# Studies on Optical Characterisation of Carbon Nanotube Suspensions

Adrian Nish

Oriel College

University of Oxford

Thesis submitted for the degree of

*Doctor of Philosophy*

Trinity 2008

# Abstract

This thesis reports studies done on single-walled carbon nanotubes (SWNTs) using optical spectroscopy as the primary investigative technique. It focuses on advances in sample preparation which have been made possible through improvements to the method of photoluminescence excitation (PLE) mapping of nanotubes.

An introduction to the field and some theoretical models are presented initially to provide a background to the experimental chapters which follow. A description of the standard procedure for sample preparation in aqueous surfactants is then followed by a detailed introduction to PLE mapping, including modeling of SWNT spectra. The next chapter discusses improvements to the sample preparation method by using organic polymer solutions instead of aqueous surfactants for suspending the nanotubes. The results show reductions in the distribution of SWNT species which are solubilised, leading to significant improvements in the resolution of the optical absorbance spectra and an increased photoluminescence yield.

Two experiments which were performed on the novel polymer-SWNT systems are then described. The first shows (via PLE mapping) that energy is transfered to the SWNTs when the polymer is photo-excited. The possible mechanisms behind this, as well as the implications for using carbon nanotubes as an additive in polymer photovoltaics, are discussed. The second experiment details a recent magneto-PL study of SWNTs embedded in films produced from the polymer solutions. Here, the improved optical signatures and absence of strain at low temperatures have revealed a previously unseen high field intensity dependence. The behavior has been explained by the magnetic field induced mixing of the excitonic states.

# Acknowledgements

I would like to take this opportunity to thank the following people for their support during my studies:

Firstly, my supervisor, **Prof. Robin Nicholas** for his ability to convey ideas both complicated or trivial in a patient and understanding manner. For his sound advice, inspirational passion and depth of knowledge in physics and in life. And for always being there when needed whilst allowing me the freedom to become an independent and confident researcher.

To my fellow DPhil and postdoc colleagues over the years: **Greg Wiltshire**, **Russell Deacon**, **Lance Li**, **Ian Mortimer**, **James Doig**, **Ben Nedniyom**, **Ken Chuang**, **Richard Tuley**, **Nutpapon Saranrom** and **James Orr**. Coffee breaks, pub lunches, conferences and office banter will leave me with fond memories of my time in the Clarendon thanks to them.

Similarly to the other students who I've had the privilege of working with and guiding during their time in our labs, many of whom have also made significant contributions to the experiments, results and ideas presented in this thesis: **Robbie Campbell**, **Jon Hwang**, **Sigrid Douven**, **Geraint Evans** and **Torben Schüttfort**.

To the **EPSRC** for financing the work and my studentship. And to **Oriel College** and the **Institute of Physics** for providing bursaries to allow me attend conferences in the USA and Canada - two of the best holidays I've ever had.

And lastly to my parents, **Alec and Mary** for the seeds of curiosity which they planted in me at an early stage, nourished with the best possible education and still support with their enthusiasm and interest in my work.

## LIST OF PUBLICATIONS

Principle Author:

"Temperature induced restoration of fluorescence from oxidised single-walled carbon nanotubes in aqueous sodium dodecylsulfate solution."
A. Nish and R.J. Nicholas. *Phys. Chem. Chem. Phys.*, **8**, 3547-3551 (2006).

"Direct spectroscopic evidence of energy transfer from photo-excited semiconducting polymers to single-walled carbon nanotubes."
A. Nish, J.-Y. Hwang, J. Doig and R.J. Nicholas. *Nanotechnology*, **19**, 095603, (2008).

"Highly selective dispersion of single-walled carbon nanotubes using aromatic polymers."
A. Nish, J.-Y. Hwang, J. Doig and R.J. Nicholas. *Nature Nanotech.*, **2**, 640, (2007).

"Novel magneto-optical behavior in single walled carbon nanotubes."
A. Nish, R.J. Nicholas, C. Faugeras, Z. Bao and M. Potemski. *Phys. Rev. B*, Submitted.

Contributing Author:

"Temperature and magnetic field dependent photoluminescence from carbon nanotubes."
R.J. Nicholas, I.B. Mortimer, L.-J. Li, A. Nish, O. Portugall and G.L.J.A. Rikken.
*Intl. J. Modern Phys.*, **21**, 1180, (2007).

"Polymer structure and solvent effect on the selective dispersion of single-wall carbon nanotubes."
J.-Y. Hwang, A. Nish, J. Doig, S. Douven, C.W. Chen, L.C. Chen and R.J. Nicholas.
*J. Am. Chem. Soc.*, **130**, 3543, (2008).

"An experimental study of coulomb corrections and single particle energies for single-walled carbon nanotubes using cross-polarized photoluminescence."
K.-C. Chuang, A. Nish, J.-Y. Hwang, G. Evans and R.J. Nicholas. *Phys. Rev. B*, In press

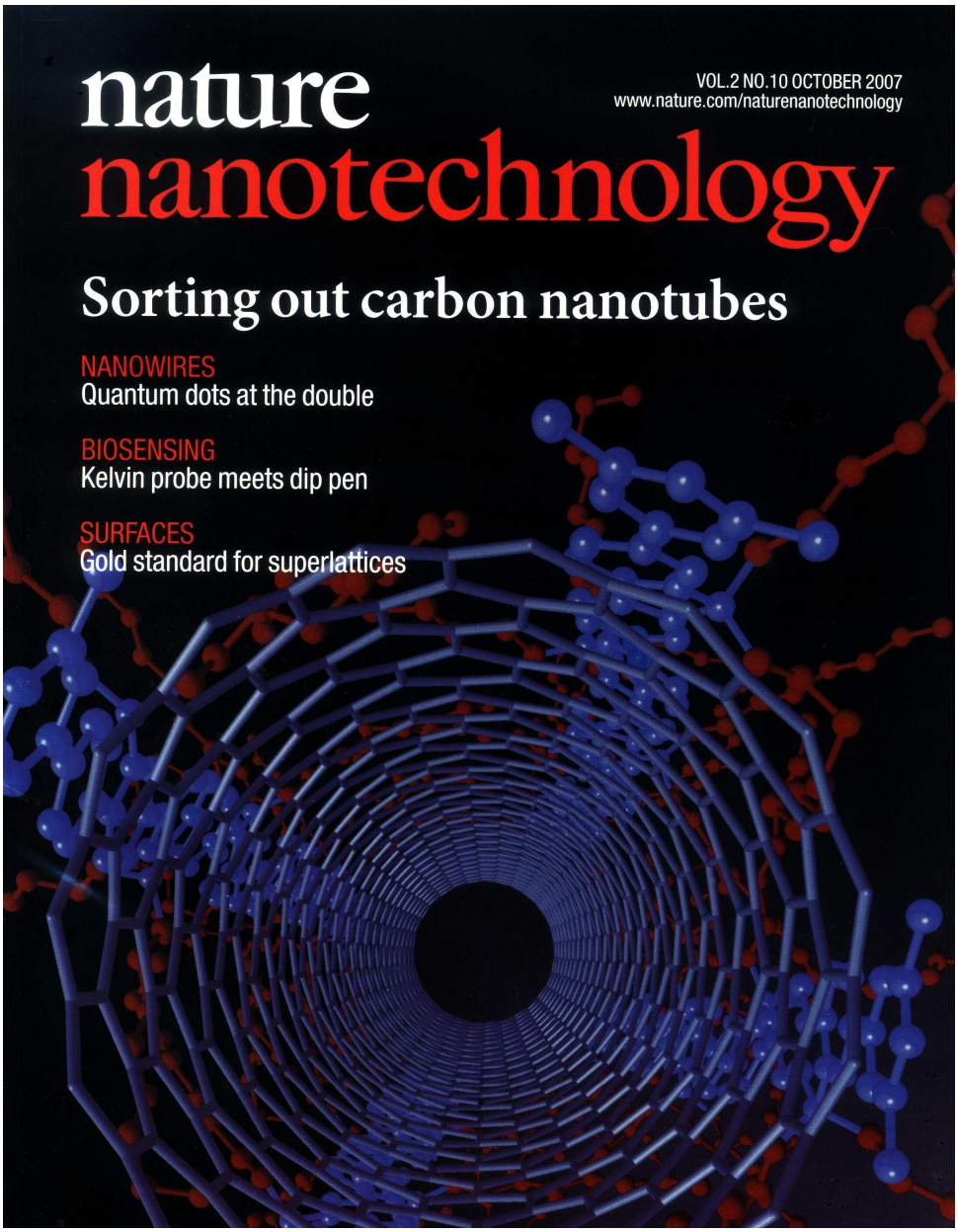


Submitted artwork accepted to accompany the publication in Nature Nanotechnology in Oct. 2007

# Contents

# Chapter 1

# Introduction

## 1.1 Carbon

Carbon is one of the most common elements on our planet. It's ability to combine with other atomic elements makes it one of the basic building blocks of the natural world and a key component of life itself. Carbon is found in all living plant and animal species, in many minerals and in the atmospheric gases. It is hard to imagine that any world as diverse and complex could exist in its absence.

The impact of carbon on mankind extends well beyond the natural characteristics which have allowed the creation of the molecules necessary for life. The decomposition of plant and animal forms over millions of years has left massive reserves of carbonaceous combustible material, which currently supply our civilization with around 81% of the energy we consume [1]. Apart from use as a fuel, carbon has had an important industrial role for many centuries in the production of iron and, later, in the production of steel [2]. In more recent times it has found uses in purer and purer forms for more high-tech applications, from graphite electrodes to carbon fibre reinforced composites to the synthetic diamonds used in cutting and in electronics. These purer forms exploit the affinity which carbon has for bonding with itself and hint towards its versatility at forming materials with considerably distinct structures.

Organic chemists have been producing molecules using hydrocarbons for generations. The seemingly endless abundance of molecules which may be produced from basic carbon units is largely due to how carbon arranges electrons around it's nucleus [3]. Carbon is element number six in the periodic table. It's six electrons, $[(1s)^2(2s)^2(2p)^2]$, allow the formation of many simple or multiple covalent bonds due to the hybridization of atomic orbitals [4]. Linear $sp^1$ hybridization of carbon atoms leads to molecules with bond angles of 180°. For example, the simple molecule ethyne has a linear structure, as is illustrated in figure 1.1a. Plane trigonal $sp^2$ hybridization produces molecules with bonds at 120° from each other. This is shown here for the molecule ethene in figure 1.1b but will also be of importance later in discussing the bond structure of graphene and carbon nanotubes. Tetrahedral $sp^3$ hybridization leads to bond angles of 109° and is illustrated here for the molecule ethane (figure 1.1c). The overlap of $s$ orbitals is referred to as sigma ($\sigma$) bonding and the overlap of $p$ orbitals as pi ($\pi$) bonding. An $sp^1$ hybridized carbon atom can make two $\sigma$ and two $\pi$ bonds, $sp^2$ hybridized carbon can make three $\sigma$ and one $\pi$ bond and an $sp^3$ hybridized carbon atom forms four $\sigma$ bonds. These

respective bond types have different formation energies and so the properties of the final structure will depend strongly on the number and nature of these bonds.

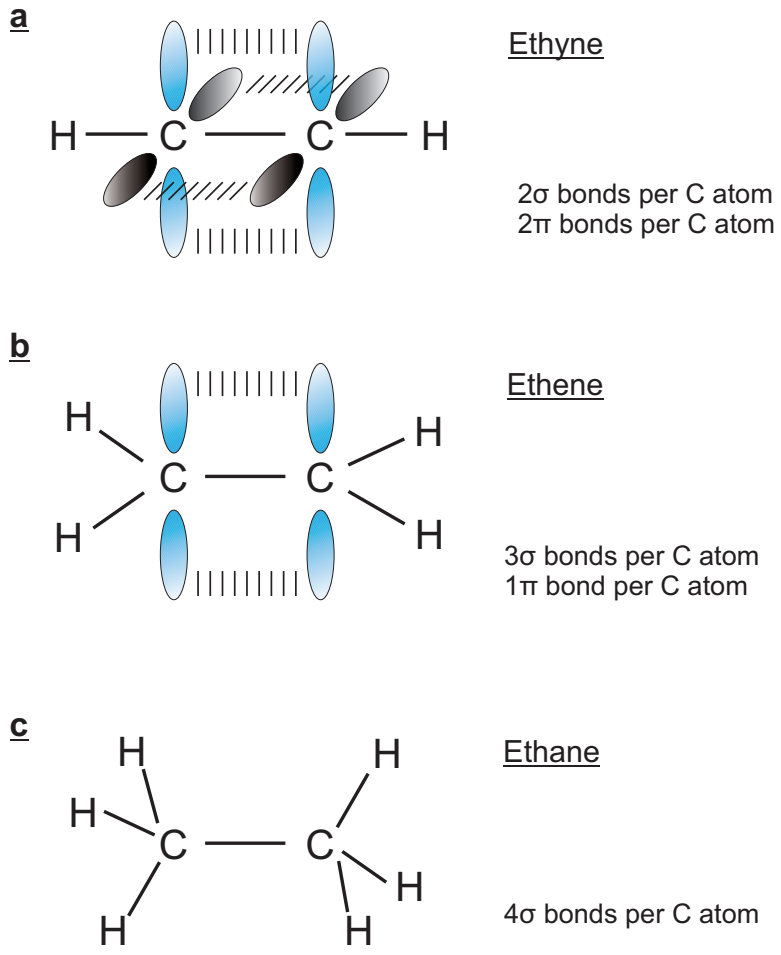


Figure 1.1: An illustration of the flexibility with which carbon bonds to other atoms using the hydrocarbons ethyne, ethene and ethane as examples.

Many pure forms of carbon, also called allotropes of carbon, are known to exist naturally or have been produced synthetically [5]. These different forms may be distinguished by their distinct bonding patterns and structures. The solid phases of all elements may exist in amorphous or crystalline forms, however, those of most interest from a scientific point of view are generally of the latter type. The crystalline carbon allotropes may be classified as belonging to four distinct families: diamond, graphite, nanotubes, and Buckminsterfullerenes. It may be argued that nanotubes and Buckminsterfullerenes should classed as part of the same 'fullerene' family and indeed, from a structural point of view, they have some similarities. However, from an electronic point of view nanotubes have much more in common with graphene (single-layer graphite) than they do with $C_{60}$ (one of the Buckminsterfullerenes) and so may be thought of as a distinct family with lying somewhere between these other two materials.

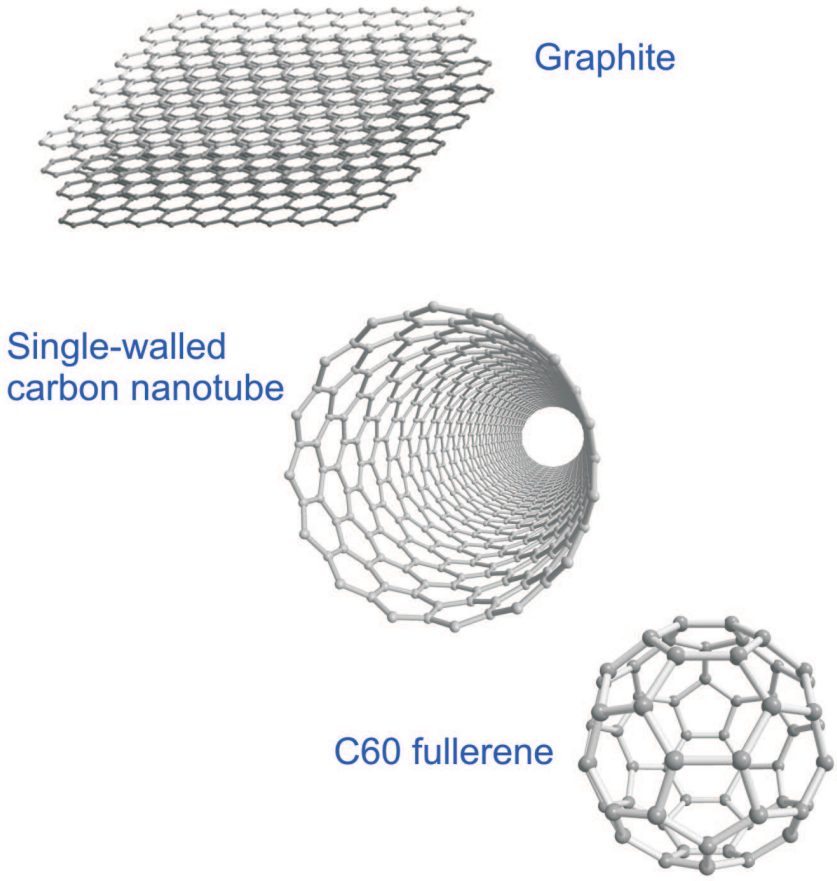


Figure 1.2: Single-walled carbon nanotubes are structurally similar to both graphite and $C_{60}$.

Diamond is a well known example of a tetrahedrally bonded crystalline structure. This arrangement of its atoms arises from $sp^3$ hybridized bonding, where each carbon atom is $\sigma$-bonded to four others. These strong bonds, fixed in an ideal crystalline network, make diamond the hardest material known to man [6]. Furthermore, the $sp^3$ bonding also accounts for diamond being an electrical insulator with a bandgap of 5.5eV and, consequently, for its optical transparency.

Graphite, as was mentioned previously, is an example of planar $sp^2$ hybridized carbon network, where layers of these quasi-2D sheets have built up into a 3D bulk structure. The intra-layer $\sigma$-bonding again makes each sheet remarkably strong but this strength is negated in the bulk material by weak non-covalent bonding between the layers. This property makes graphite useful for pencils, where the lateral friction caused by contact with paper allows these layers to easily slide off in small portions. The electronic properties are also significantly different where, in contrast to diamond's tetrahedral structure, each carbon atom is bonded to three others. This leaves one $p$-orbital (perpendicular to the plane of the graphite layer) to allow the formation of an extended $\pi$-bonded network with associated free electrons. As a result, graphite is semi-metallic in behavior and has a broad optical absorption which gives it a lustrous, silvery black appearance.

Buckminsterfullerenes are a predominantly synthetic allotrope of carbon which have been of interest to scientists since their discovery in 1985 [7]. $C_{60}$ is the proto-typical fullerene and consists of sixty carbon atoms in a spheroidal shape of alternating five and six-membered rings. The bonding is mainly $sp^2$ in nature though the curvature of the molecule's surface also gives it further hybridization with the perpendicular $p$-orbitals. The material is found to be a semiconductor with a band gap of 2.3eV (in bulk films). The unusual name of these molecules comes from Buckminster Fuller, the American architect and visionary most famous for inventing the geodesic dome. In 1985, having discovered the $C_{60}$ clusters that would later win them the Nobel Prize, Harry Kroto et al. needed to find a regular sixty element structure which would satisfy their new molecule. After realizing that a truncated icosahedron, or soccerball shape, would elegantly fulfil this requirement they titled their letter to the journal Nature '$C_{60}$:Buckminsterfullerene', in honor of the man who had pioneered the use of such structures in architecture. However, a number of alternative names were also proposed in the text of the paper. One can only wonder if this inspirational molecule would have become quite so enigmatic had the authors instead have decided to use the name 'soccerene' in their title.

## 1.2 Nanotubes

Nanotubes are the allotrope of carbon which have been the focus of the research done during the course of the studies for the chapters that follow. Their properties have much in common with all the previously described carbon families. Like diamond, they are of high purity and crystallinity. Furthermore, they show remarkable mechanical strength and are excellent thermal conductors [8]. However, they are also close to graphite in structure and physical properties. If one could roll up a single layer of graphite (graphene), to form a tight seamless cylinder around 1nm in diameter, it would produce an identical structure to that of the carbon nanotubes which are, needless to say, produced by other means. In light of this, the models used to describe nanotube structure are based on the graphene lattice. Similarly, the models for nanotube electronic structure come directly from solving the dispersion relation for graphene, with some simple extensions made to take account of the boundary conditions imposed by the finite circumference [9]. Consequently, nanotubes can exhibit either semiconducting or metallic behavior depending on their geometry [10]. This is again a property that comes from graphene, which is a semi-metal and has highly anisotropic electrical conductivity.

In terms of their relationship to Buckminsterfullerenes, nanotubes are also closed cages of carbon atoms with highly curved surfaces, a characteristic which sets the fullerenes apart from the other carbon allotropes. Many people believe that the ends of carbon nanotubes are closed by hemispheroidal caps; these caps would require the presence of five or seven-membered rings and so should have structures somewhat similar to half a $C_{60}$ molecule.

Notwithstanding the similarities which nanotubes have with other carbons, they are a class of molecules which is virtually unique in science, unparalleled thanks to both the novelty of their structures and to their exceptional properties. These characteristics, along with the possibility of exploring physical phenomena in a new system and the potential for future applications, have propelled carbon nanotube research to the forefront of physics research in recent years. Furthermore, carbon nanotubes have branched into popular science in a way which has not been seen for any other molecule. Science textbooks for undergraduates [11], science journals [12] and even contemporary science books available in high street stores [13] may be found with illustrations of carbon nanotubes and fullerenes on their covers. Much of this is due to hype surrounding the coming of the 'Nanotech age' but a great deal is also due to a natural fascination with the elegance of their symmetry and the distinctive character of these novel structures.

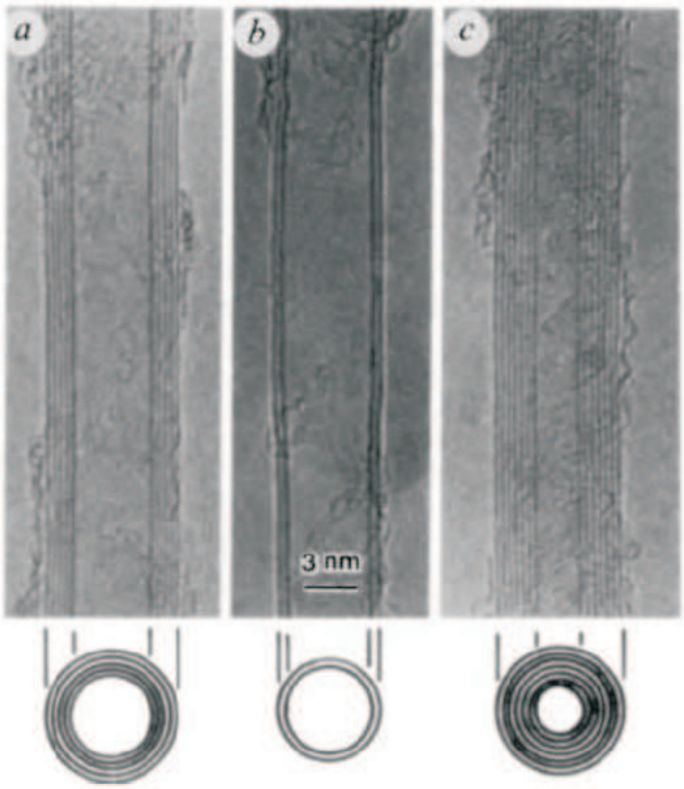


Figure 1.3: The original TEM evidence to support the discovery of carbon nanotubes presented by Iijima in his Nature paper of 1991.

Carbon nanotubes are not restricted to one type of geometric structure [14]. In fact there are classes and further sub-classes of structures within the overall nanotube family. In 1991, Sumio Iijima was performing TEM studies on novel structures formed in different regions of the reaction vessel from the Krätschmer-Huffman [15] method for producing $C_{60}$. When he analyzed the soot from inside the hard cathodic deposit of the arc-evaporator, he discovered in his images what he described as "a new type of finite carbon structure consisting of needle-like tubes" [16]. Closer inspection revealed these to be coaxial tubes of graphitic sheets, ranging in number from 2 to 50 concentric cylinders. Although he may not have been the first to image such fine carbon fibres [17], Iijima was the first to correctly report the concentric tubes; previously these structures had been thought of as rolled up graphene sheets. The outer diameters of Iijima's nanotubes ranged from 4 to 30nm with their lengths being of up to 1 micron. He also noted that "the helical pitch varies from needle to needle and from tube to tube within a single needle", an important initial observation of what we now call the nanotube's chiral angle, with its variability being one of the fundamental characteristics of ensemble samples. It was later shown [18] that many of the observed structures were closed at both ends, most probably due to the formation of defects, but other than that were found to be pristine in their regularity and crystallinity. Varying numbers of concentric tubes were found to exist, including double-walled nanotubes; however, it wasn't until 1993 that Iijima and others finally produced and imaged SWNTs by further TEM analysis of soot deposits [19, 20]. The trick was to use a metal catalyst in the growth process. This aided the formation of smaller nanotubes in the vapor phase of the reaction, which were then deposited on the sidewalls of the arc-evaporator's chamber. These nanotubes had much smaller diameters than the typical minimum of 4nm found in MWNTs. The striking difference, apart from the much reduced diameter, of the SWNTs in TEM was that where the MWNTs had always been found as extremely rigid rods, the single shell tubes were rarely straight and often were found to be curled or even looped. Although this could have been due to the presence of more defects, subsequent work has shown SWNTs (as with MWNTs) to be of highly regular crystallinity. The more rigid appearance of the MWNTs in TEM images is simply due to the natural reinforcement which comes from adding more concentric layers to the system. Another finding of initial TEM work on SWNTs [21] was that, in high purity samples, the nanotubes were often present in aggregations referred to as 'ropes' or 'bundles'. In these aligned SWNT arrangements, several tubes grow in parallel and become tightly bound along their axes by van der Waals forces. Initially [22] it was hoped that, due to the more uniform local growth conditions, the SWNTs in these bundles would all be of identical structure. Subsequent studies showed this not to be the case. These inhomogeneous bundles of tubes are one of

the major problems in SWNT research and significantly hamper their possible application. Much of the work done for this thesis has concerned the breaking up of these bundles to produce dispersions of isolated individual SWNTs.

Carbon nanotubes for laboratory use have the appearance of a black powder or 'soot'. Their broad optical absorbance in the visible region of the spectrum is a feature they share with graphite and is thought to be due to the oscillation of free $\pi$-electrons in these bulk samples. Despite being indistinguishable to the naked eye, nanotubes have a variety of sub-classes which arise from the differences in their atomic arrangements:

**Carbon Nanotubes**
→ **MWNTs or SWNTs**
→ **Semiconducting or Metallic**
→ $q = \pm\mathbf{1}$[†]
→ **Diameter and Chiral Angle differences**

Thus, when a sample of SWNTs is purchased from a supplier, we do not receive something which contains nanotubes of a single specified structure but actually a distribution of different nanotube structures (also known as chiralities). These structures are all mixed together and is what is referred to when we describe 'ensemble' samples. The distribution is a natural consequence of the growth process and the near impossibility of keeping the local conditions at a nanometer length scale identical across the reaction vessel. The fact that different chiralities of nanotubes are found in bundles (which grow simultaneously from the same catalyst particle) is an indication of the impossibility of growing a single type of structure.

Single-walled carbon nanotubes are often bought from commercial sources with purities of >90% for gram quantities of material. At the time of writing, SWNTs prepared by the 'HiPCO' growth process [23] were being sold for about £300 per gram by Carbon Nanotech. Inc., the sole supplier of this the standard material of nanotube optical spectroscopy research. Methods for producing MWNTs on the other hand have allowed the economy of scale to reduce their cost significantly, with kilogram quantities of material at up to 90% purity readily available at a price of around £0.10 per gram.

[†]Only applies to the semiconducting species and will be explained in the next chapter.

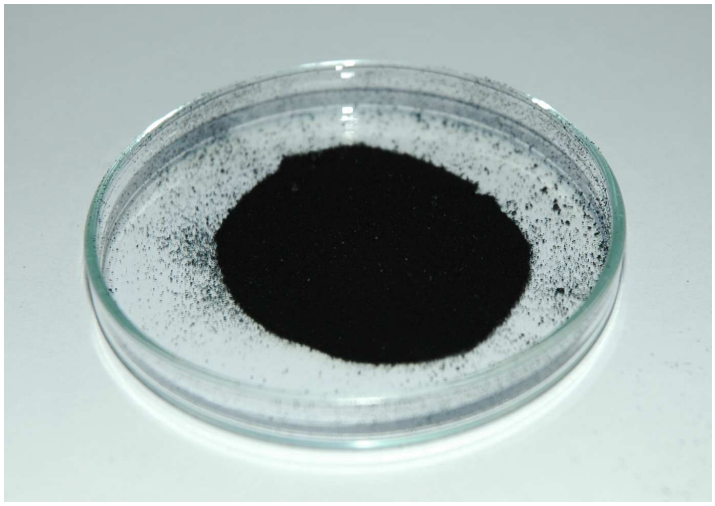

Figure 1.4: Macroscopic amounts of pure carbon nanotubes have the appearance of a fine black soot.

This has enabled MWNTs to be incorporated into many applications, some of which, such as mobile phone batteries, may be more ubiquitous than one might realize. It has to be said though that these applications are somewhat 'low-tech' and are simply improvements where carbon black had previously been used. The hope is that a truly revolutionary application could be found for carbon nanotubes, thereby justifying their remarkable hype and mirroring the impact they've had in academia in industry too. For such a leap to occur, SWNTs (with their superlative properties) would almost certainly need to be used.

Single-walled carbon nanotubes have been touted as revolutionary new technological materials since their discovery. One of the most famous and enduring claims is that of Arthur C. Clarke when discussing the possibility of making a tethered geo-stationary satellite that could be used as an elevator for launching space-craft. In his 1979 fictional novel, The Fountains of Paradise [24], one of Clarke's characters asserts that such a construction could be achieved using a *"continuous pseudo-one-dimensional diamond crystal"*. This is a remarkable prediction considering that only just over a decade later carbon nanotubes were discovered and, although a space elevator has yet to be constructed from them, it was apparent to science fiction writers that their mechanical properties could offer some major technological breakthroughs. Other, more down to earth, applications which may benefit from carbon nanotubes have also been proposed in the meantime and include:

- Electronics (transistors & wires, ref. [25])
- Field-emission devices (displays, ref. [26])

- Opto-electronics (light emitting diodes, ref. [27])
- Photo-voltaics (for energy capture or transfer in polymer composites [28])
- Gas storage (hydrogen storage, ref. [29])
- Sensors (gas and chemical sensors, ref. [30])
- Fluorescent labels (for use in biology or as markers in detecting counterfeit goods [31])
- Medical applications (drug delivery, glucose sensors, ref. [32])
- AFM probes (ref. [33])

Some of these applications have already been commercialized. For example, nanotube tipped atomic force microscopy (AFM) probes may be bought from Nanoscience Instruments and are a significant improvement on their standard silicon derived counterparts. This comes from the high aspect ratio found in carbon nanotubes, allowing imaging of surfaces with sharply edged features such as steps or holes.

Although highly ambitious, the field of nano-electronics is one of the most exciting potential applications for SWNTs. Their use here could completely revolutionize an industry based entirely on silicon and photo-lithography. Whilst this material and related processes have evolved over decades to provide us with the hardware of the modern computing and information technology era, future advances rely on reducing component size to smaller and smaller length scales. With this challenge come significant technological issues and ultimately some intrinsic limitations. However, a circuit made of molecules with semiconducting and metallic properties could fully exploit the ultimate potential of classical computers thanks to the speed at which the components could be switched between their 'on' and 'off' states. Single-walled carbon nanotubes are the perfect molecular systems for this task. Semiconducting nanotubes have band-gaps which are comparable to silicon but with much lower scattering probability and higher mobility thanks to their supreme crystallinity and 1D nature. This makes them well suited for the switching components of a molecular circuit whilst the high conductivity and high aspect ratios of metallic SWNTs makes these ideal for the interconnecting wires. Although an all nanotube electronic circuit is far from being commercialized, notable successes have been made at producing nanotube transistors and even integrating them to make simple circuits and useful devices operating at frequencies of over 100 GHz [34]. One of the major hurdles to be overcome

before a nanotube computer could be made involves producing or fractionating the desired nanotube structures for the individual components, most notably obtaining semiconducting or metallic species when desired. Further issues then arise from trying to deposit the nanotubes in the desired location and from interfacing the metallic SWNT wires to their semiconducting counterparts. As was already stated, the move from silicon to carbon nano-electronics is an ambitious goal but one which will no doubt yield fascinating cutting edge research for many years to come.

Another, more obscure but highly amusing use for nanotubes was proposed by Yurdumakan et al. in 2005 and involved using the SWNTs to produce dry adhesive tape [35]. The inspiration for this work was the natural mechanism by which lizards known as geckos can seemingly grip any flat surface. The soles the gecko's feet are covered with minute hairs, which collectively result in an extremely high surface area and sufficient capillary and van der Waals attraction to allow them to climb vertical walls with ease. A similar material could be made from vertical arrays of SWNTs and, if a large enough sheet could be manufactured, would produce enough adhesion to support the weight of a person wearing 'gecko gloves' [36]. Whilst this seems like a trivial example of a nanotube application, it does hint at the diversity of activity in the field of applied SWNT research.

Aspects of the research done in the course of studies detailed in this thesis are of importance across a range of technological applications. For example:

1. Improvements in sample purification through the use of organic polymers have led to bulk samples which are free of metallic SWNT species, something which could be of importance to work on nanotube electronics.

2. The studies on energy transfer from photo-excited organic polymers to SWNTs will be of significant interest to researchers investigating the potential which nanotubes have for improving the performance of organic light emitting devices (OLEDs) and photo-voltaics.

3. Improvements made in characterisation, particularly in the development of PLE mapping as a useful tool for sample analysis, will hopefully have a positive impact on nanotube production studies. This is an area which has shown remarkable progress in recent years but which still holds the key to realizing many of the exciting applications of SWNTs.

4. Another, more novel, potential application of the polymer-based purification process arises from

being able to control the final distribution of nanotube species in a purified sample. Mixtures of these distinct samples allows the creation of a multitude of different dispersions, each with its own identifiable and unique fluorescence signature. It is possible that these dispersions could then be applied to any surface as an invisible label, only readable with specialized detectors.

## 1.3 Synthesis

As mentioned previously, carbon nanotubes are a wholly synthetic molecule which are currently produced in research laboratories and by companies around the world in ever increasing volumes. Far from being the challenge to synthesize that one might assume from their relatively recent discovery, nanotube growth has actually been shown to occur in a number of different environments. As long as the basic requirements of a metal catalyst, carbon feedstock and sufficient energy are supplied, single-walled carbon nanotube formation is possible [37].
There are three common ways to produce SWNTs: arc discharge, laser vaporization and chemical vapor deposition. The principles behind these processes are summarized as follows.

### *Arc Discharge*

The arc discharge process was one of the first methods of nanotube production. Iijima used an arc evaporator, based on that which Krätschmer & Huffman had been using for $C_{60}$ synthesis, to produce the first multi-wall and then single-walled carbon nanotubes. It still has benefits over other contemporary methods in that high quality and low defect tubes may be produced using a relatively simple apparatus. Figure 1.5 shows a diagram of the arc evaporator, also sometimes called a Krätschmer generator. The basic principle of its operation relies on a low voltage, high current power supply (often derived from an arc welder unit) creating an arc between two graphite electrodes in an inert gas atmosphere. The arc is extremely hot and vaporizes the narrower anode electrode. This results in the formation of thick black deposits of soot throughout the reaction chamber. The key to producing single-walled nanotubes is using a metal catalyst. Adding the catalyst is done by boring out the middle of the graphite anode and filling it with a mixture of a fine powdered metal (such as iron, cobalt or nickel) and powdered graphite. Variations on the catalyst mixture and inert gas type and pressure

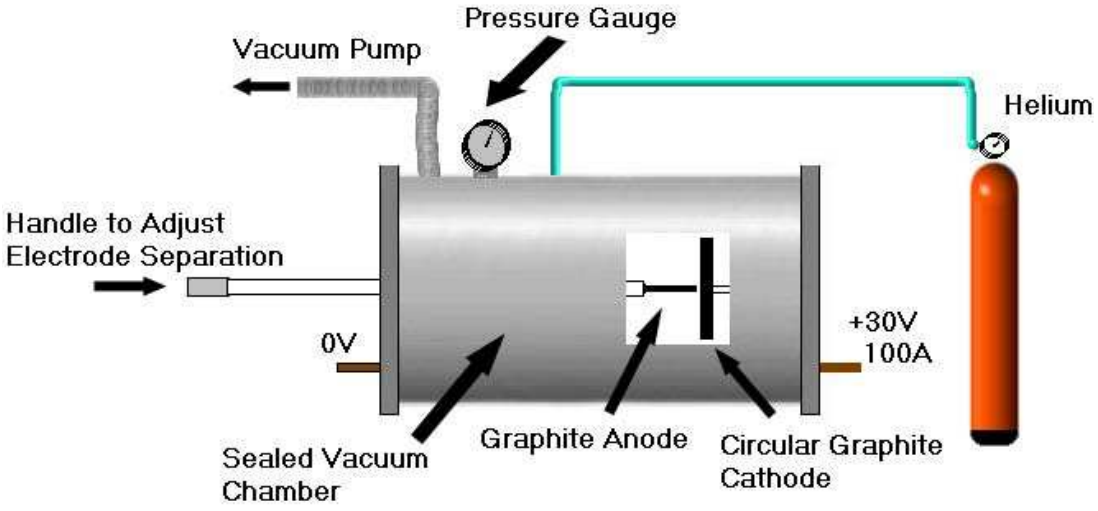


Figure 1.5: Diagram of an arc evaporator used to produce SWNTs.

allow the control of nanotube yield and the diameter distribution. Typically, SWNTs from the arc process have an average diameter of 1.35nm with a distribution ranging from 1.1 to 1.6nm [38].

***Laser Vaporization***

The laser vaporization method is similar to the arc discharge process in that the carbon source is initially a solid which is evaporated in the presence of a catalyst to produce SWNTs. A metal catalyst impregnated graphite 'target' (similar to the anode described in the arc method) is heated

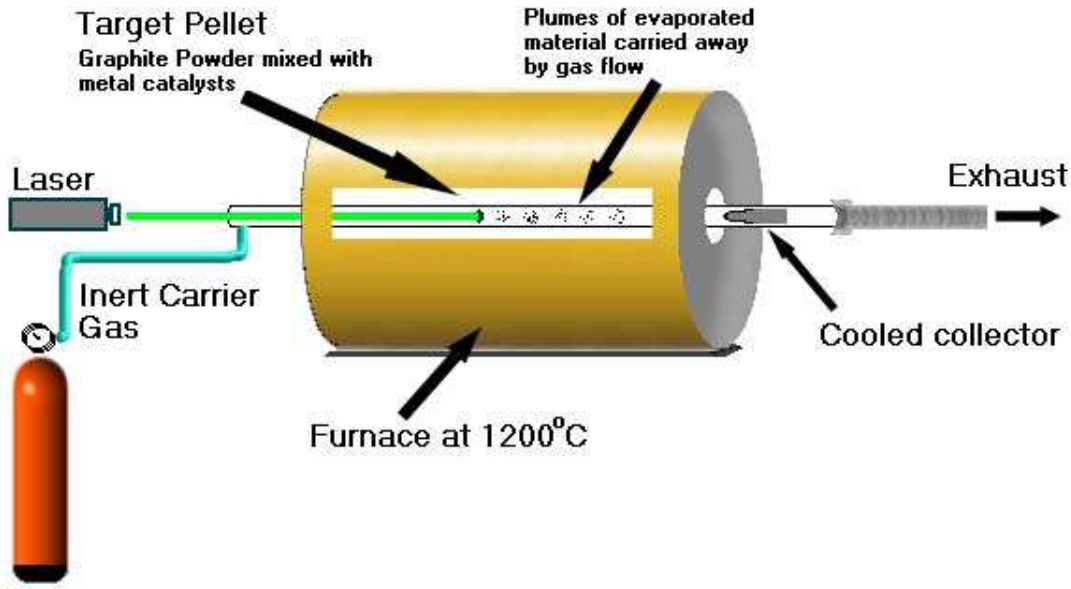


Figure 1.6: Diagram of the general apparatus used in the laser vaporization process.

in a furnace to 1200°C, with an inert atmosphere provided by helium or argon gas. A high powered continuous-wave or pulsed laser system is used to vaporize the target, forming a plume of molten metal droplets saturated with atomic carbon. As the plume is swept away from the target zone by the buffer gas it cools, causing the segregation of the carbon on the surface of the still-molten metal droplets. The nanotubes are then thought to form spontaneously, growing outward radially from the catalyst particle. As with the arc process, carbonaceous by-products are also created, though the laser vaporization process does form some of the highest quality material available. Furthermore, it also produces SWNTs with a narrow diameter distribution, centered on an average of 1.2nm, with a range from 1.1 to 1.3nm [38].

***Chemical Vapor Deposition***

The chemical vapor deposition process (CVD) involves the decomposition of a hydrocarbon gas at medium temperatures over a catalyst covered substrate. Nanotubes grow vertically from the substrate and look like a dense patch of grass under SEM. Figure 1.7 shows the classical apparatus for CVD, simply consisting of a quartz tube inside an oven. For SWNT production, a thin film of metal catalyst is deposited onto a substrate such as silicon. As with the other methods, this catalyst may be iron, nickel or cobalt. The substrate is then loaded onto a quartz boat and carefully placed in the center of the tube. The tube must be sealed and evacuated. High purity acetylene gas is then introduced and heated to the required temperature of between 700 and 1000°C. A pressure of 1mbar of acetylene is constantly flowing through the tube and a typical run takes 10 minutes. This method

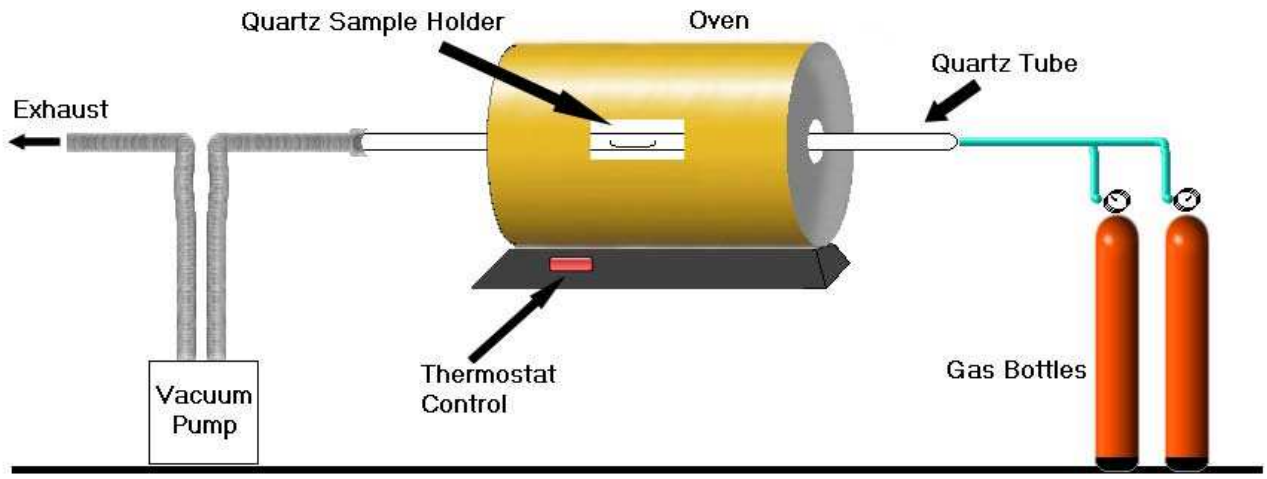


Figure 1.7: Basic schematic of the CVD apparatus used to grow nanotubes.

has an advantage over others in that the nanotubes may be grow on the substrate in an organized predetermined fashion. This gives it potential for electronics applications where controlled positioning of the nanotubes would be vital. Also, it is easy to imagine the scaling up of the process, as substrates could be prepared in a method similar to the oxide growth or impurity doping stages of current IC production. Furthermore, tedious purification procedures are not required as generation of by-products is minimal. Unfortunately though, as with the other synthesis methods, it is not possible to control the growth of metallic verses semiconducting species, something which would be a major hinderance for nano-electronics applications. Nonetheless, many other potential applications exist and, as before, by controlling the conditions in the reaction vessel one can control the diameters of nanotubes produced. High purity material of up to 99% SWNTs can be grown using CVD methods with broad or narrow diameter ranges spanning anywhere between 0.4 and 5nm [37].

The three methods which have been discussed here are the classic SWNT growth processes. Many other procedures exist, mostly derived from the CVD method, but two in particular are worth further elaboration here. These are both processes which have developed into the leading sources of the high-quality, narrow diameter distribution material most suited to work on optical spectroscopy.
The first of these is called the **'HiPCO'** process [23], standing for high pressure carbon monoxide. It is a CVD process but does not have any substrate to support the catalyst or for the nanotubes to grow from. Instead, the catalyst is introduced as a gas simultaneously with the carbon monoxide. This catalyst gas is generally $Fe(CO)_5$ which, at an elevated temperature of around 1000°C and pressure of 30 to 50 bar, is converted into carbon rich iron nano-droplets. Further carbon feedstock is provided by the disproportionation of additional carbon monoxide injected into the growth zone. The nature of this type of growth process means that a continuous flow of product can be set-up with gram to kilogram quantities obtainable. Purities of over 90% SWNTs can be achieved with average diameters of 1nm and a distribution ranging from 0.75 to 1.25nm [39]. The second material of much importance to SWNT spectroscopy comes from the **'CoMoCAT'** growth process [40]. This process also uses carbon monoxide as its feedstock and produces a SWNT material of similarly high purity to HiPCO. The presence of atomic oxygen in both these processes is thought to play a key role in achieving this high-purity by acting as a scavenger of amorphous carbon (which is more reactive than the graphitic variety). The catalyst used here is a mixture of cobalt and molybdenum on a mesoporous silicon dioxide substrate. Fine control of the catalyst's nanoparticle size and uniformity have resulted in ensemble samples with a remarkably narrow diameter distribution, approaching that of just two

dominant structures of SWNT. These dominant tube species have diameters of around 0.85nm, with the remaining minority species ranging from 0.7 to 1nm [40]. Both of these production processes have been turned into commercial sources of SWNT material with HiPCO being provided by a spin-off of the Rice University group called Carbon Nanotech Inc. and CoMoCAT provided by a spin-off of the Resasco research group called Southwest Nanotechnologies.

## 1.4 Characterisation

Carbon nanotube characterisation has been a major challenge since their discovery. This has mostly been due to the problem of sample inhomogeneity and the subsequent difficulties that arise in sample preparation. Nanotubes are grown as poly-disperse ensembles of many distinct structures, each with only very subtle differences to the other species present. Added to this, they generally form as bundles of randomly distributed species, compromising their properties as individuals and making global characterisation methods ineffective. The unique properties of distinct nanotube species can only be elucidated through the splitting of these bundles into isolated individual tubes which may then be probed using a variety of methods. Preparative techniques (detailed later in this thesis) have been developed which can accomplish this exfoliation of nanotube bundles with remarkable efficiency. These rely on dispersing the nanotubes in liquid suspensions where a dispersing agent holds the individual SWNTs in a stable suspension. Researchers working on optical spectroscopy of SWNTs have been the prime motivators in developing these dispersion based methods for nanotube characterisation. However, the samples prepared using these procedures have also advanced many more characterisation methods thanks to their effectiveness at obtaining samples highly enriched in isolated SWNTs.

Some techniques are capable of probing the SWNTs at an individual tube level, such as scanning tunneling microscopy (STM) and transmission electron microscopy (TEM). Others analyze the samples globally, such as x-ray diffraction and the optical spectroscopy techniques. Although there are many methods for investigating the physical and chemical nature of SWNTs, the techniques of prime importance for this thesis are those which yield the most informative results and can be applied on a routine basis. Thus the following two sections have been devoted to the branches of SWNT characterisation which have the most significance for the field.

***Microscopy***

Individual SWNTs are far too small to be observed with conventional optical microscopy, being around a factor of 200 times smaller than the resolution limit of a microscope using visible light. Electron microscopy has a much lower limit though since the wavelength of electron is far shorter than that of photons. Thus, both scanning electron microscopy (SEM) and transmission electron microscopy (TEM) can be used to image nanotube features on substrates and across grids. Indeed, as was discussed previously, the first evidence for carbon nanotubes came from studies done using TEM on soot produced in an arc evaporator. Since then, TEM in particular has become a common method of nanotube analysis due to its ability to unambiguously determine the presence of SWNTs and to qualitatively assess the purity of samples. It may also be used to measure the diameters of the nanotubes, however this becomes a prohibitively tedious task where statistical analysis of batches of material is required. It also lacks definitive structural recognition, as few labs exist worldwide that can actually image the nanotube with sufficient resolution to also determine its chiral angle. Nonetheless electron microscopy is a powerful technique of analysis which can produce awe-inspiring reminders of exactly what these molecules look like.

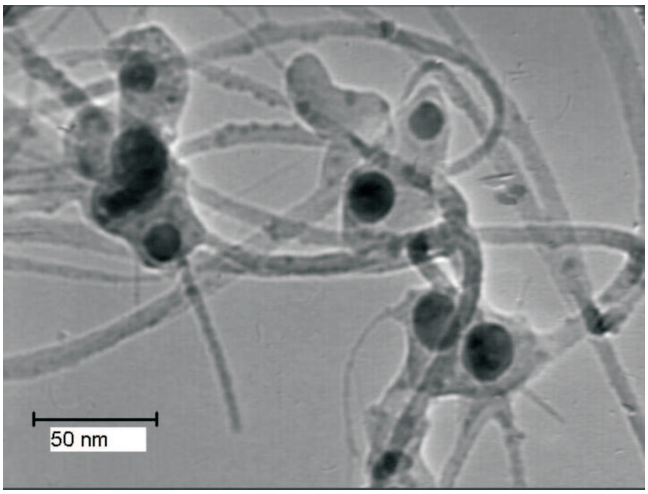


Figure 1.8: TEM image of SWNTs grown using the arc discharge process. The dark spots are metal catalyst particles and are seen to have bundles of nanotubes protruding radially from them.

A related technique which does have structural recognition ability is electron diffraction [41]. This can be done in a high resolution transmission electron microscope and produces unique patterns of bright and dark spots or fringes for the various structures of SWNT [42]. Isolation of individual SWNTs is crucial for this technique as bundles contain different structures and thus produce complicated diffraction patterns. Interpretation of these patterns is difficult but may be done by using computer

software to compare the recorded images with simulated predictions. Currently, this technique and photoluminescence-excitation mapping (PLE mapping, described later) are the main characterisation methods which yield a full determination of the populations of distinct species in ensemble samples. With the PLE mapping method, however, there are uncertainties which arise due to differences in the intrinsic PL efficiency of the different SWNT species. Thus the electron diffraction method is the only technique which can unambiguously characterise a given SWNT ensemble in terms of its constituent species distributions, albeit with the same issues that make TEM a prohibitively tedious way to get statistical data.

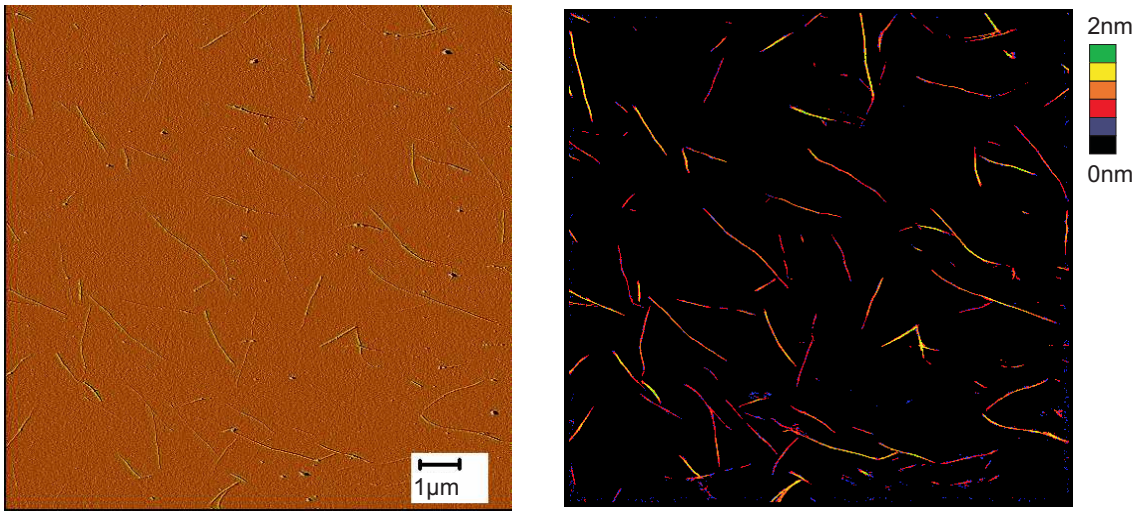


Figure 1.9: AFM images of individual nanotubes and small bundles on a GaAs substrate. The image on the right is a false colour version of that on the left with the colour scale (not shown) corresponding to heights of the features on the surface. Typical heights were in the region of 1-2nm, indicating the nanotubes are deposited as individuals as opposed to being in bundles.

Another technique that falls under this heading is known as atomic force microscopy (AFM). This method relies on a sharp tip at the end of a cantilever which is subjected to a minute deflection as it is scanned across the surface of the sample. For studying SWNTs it is necessary to deposit a low concentration of tubes on a clean flat substrate such as $SiO_2$ or GaAs. The sharpness of the tip is always a limiting factor restricting the lateral resolution of the scan in any AFM experiment. This is particularly pertinent for probing SWNTs as their nanometer scale diameters makes them too small to be imaged accurately. However, height measurements are not affected by the problem of tip convolution and so nanotube diameters can be accurately determined from the profile of the scan or through adding a false colour scale, as is shown in figure 1.9. AFM is also extremely useful for SWNT length measurements and is commonly used for this purpose.

***Spectroscopy***

Optical spectroscopy is probably the most effective method of SWNT characterisation available. It has developed over recent years into a reliable, quick and easy route to semi-quantitative information on the species present in a given sample and their relative concentrations. For this reason, optical spectroscopy has been used extensively as a characterisation technique through all the studies presented in this thesis. Critical analysis of methods have been performed along the way in order to build on the reliability of the general techniques and to strengthen confidence in the results they give.

As will be established in the next chapter, the optical spectroscopy techniques used predominantly here are sensitive to the electronic band-structure of SWNTs. Also used, to a much lesser extent, has been Raman spectroscopy. This technique probes the various optically activate phonon modes in carbon nanotubes. Sample preparation is more straightforward than for other spectroscopic or microscopic methods since the distinct properties of importance to Raman are less affected by their environment. However, all allotropes of carbon are Raman active with the position and width of the peaks being dependent on the particular form in question. Since multiple forms of carbon exist in raw unpurified nanotube soot this can obscure the interpretation of Raman spectra. One peak feature is a distinct indicator of the presence of SWNTs. It is called the 'breathing' mode and arises from the radial expansion and relaxation of the nanotube structure at low frequencies of $< 200$ cm$^{-1}$. The intensity of the radial breathing mode (RBM) is highly dependent on the energy of excitation, otherwise known as a resonance effect. Also, the energy of the peak is almost inversely proportional to the SWNT diameter with some simple empirical corrections made to accurately describe the dependence. These two experimental parameters, the excitation energy used and the resultant peak position, allow a very reliable determination of the exact nanotube species present in a given sample.

Although the sample preparation is simple, obtaining clear Raman spectra from SWNTs can be a challenge due to low signal to noise ratios and the requirement for sophisticated excitation and detection equipment. A far simpler optical characterisation technique is absorbance spectroscopy. This probes the allowed optical transitions between the SWNT's electronic energy levels in the visible and infrared regions of the spectrum. Sensitive to both features in metallic and semiconducting tube types, optical absorbance spectroscopy can yield quantitative information on the composition of a nanotube sample in terms of the concentrations of the species present. It is, however, sensitive to

the sample preparation and highly resolved peaks can only be obtained after purification to remove the undesirable carbon forms as well as bundles of SWNTs. Even with some of the best purification methods, optical absorbance still suffers from the intrinsic problem that some different tube structures have overlapping energies. This limits the ability to resolve the contributions of each of these tube structures to the overall absorbance intensity. This hindrance though is not an issue for the more powerful technique known as photoluminescence spectroscopy. A fortunate relationship exists between the primary and secondary energy levels for the different SWNT types meaning that no two tube structures possess both the same bandgap and secondary energy transition. As a result of this, photoluminescence spectroscopy may be performed on SWNT samples where the secondary energy gap is excited whilst the bandgap is determined via the emitted light. Since the intensity of the emitted light is strongly dependent on the excitation energy matching the secondary energy transition, both energy gaps can be accurately determined by scanning the excitation source and recording the change in emission as a function of its wavelength. Peaks on the resultant two-dimensional plot of excitation vrs emission can then be unambiguously assigned to established values for the secondary and primary energy levels. This method is called photoluminescence-excitation (PLE) mapping and will be the subject of an entire chapter of this thesis due to it's significance, the advances made in it's development and the uses found in the characterisation of SWNT samples.

## 1.5 State of the Art

The field of carbon nanotube research has received much attention and publicity from it's beginning at the start of the 1990s. For those with an interest in the optical spectroscopy of materials, nanotubes have provided a wealth of interesting theoretical modeling challenges and experiments. In response to burgeoning activity in this sub-section of carbon nanotube research, a special conference series was initiated in 2005. It was called the Workshop on Nanotube Optics and Nanospectroscopy or 'WONTON' for short. The scope of this conference was to provide a forum for the presentation of the latest results on nanotube spectroscopy and to promote topical discussion among the most prominent researchers in the field from around the world. At this first meeting, held in Telluride in Colorado, many initial reports of what would become ground breaking work were first presented. These included the first demonstration of fluorescence imaging of individual nanotubes in liquid phase

and the first report of the density gradient centrifugation method for purifying and separating SWNT ensembles. One of the most interesting debates of the conference surrounded the origin of the low PL yield in SWNTs. This is a topic which encompasses many researchers' interests and is also of significant importance to the technologists who might hope to make use of the optical properties of this material. Much of the debate surrounded the role which non-emissive singlet excitonic energy states were playing. These states, called 'Dark-excitons', had been predicted to exist by several theorists and were thought to lie just below the main radiative singlet exciton level. Their presence implied that as the electron and hole relaxed after excitation they would end up in this lowest energy state and therefore no photoluminescence would occur. However, at temperatures above absolute zero, thermal energy causes the electrons to populate the higher radiative levels. Nonetheless, their existence could explain the low PL yields which are observed. Magneto-PL and temperature dependence experiments were carried out by our group which helped to describe some of the characteristics of these states -the latest of these results are presented here in chapter 7.

By the time of the 2nd Workshop on Nanotube Optics and Nanospectroscopy, held in Ottawa in 2007, the role of dark excitons had been more established. However, it was also evident that other factors were at work in suppressing the PL yield at room temperature. This realization came about through various different improvements in experimental conditions that meant the true PL efficiency could be probed more closely. Some of these approaches used the aforementioned microscopic imaging of SWNTs where the absorbance could also be simultaneously measured in-situ, others relied on results from time resolved PL spectra. Further work presented, including that which will be described later in this thesis, relied on improvements in nanotube purification that remove the impurities which cause parasitic absorbance in ensemble samples. What was remarkable is that in all these independent and different experiments the values being quoted by the investigators were all in the region of $\eta$=2% to 7%, approximately an order of magnitude higher than what had been thought at the time of WONTON'05. Although there now seems to be a good consensus that we are approaching the true value for the SWNT PL efficiency, what is still unclear is the reason behind it. In particular, it is hoped that by WONTON'09 the mechanisms by which the exciton relaxes from the secondary energy levels to the band edges will be sufficiently understood. Whilst there can be little doubt that the progress over the past decade in nanotube research has achieved a great deal, it is remarkable that so much original research is still being done on these materials and that they seem to have much more to offer than was ever thought before.

# Bibliography


[1] *Key World Energy Statistics.* International Energy Agency, 2007.

[2] M. Inagaki. *New Carbons. Control of Structure and Functions.* Taylor & Francis, 2006.

[3] N. N. Greenwood and A. Earnshaw. *Chemistry of the Elements.* Pergamon, 2nd edition, 1997.

[4] P. Atkins and L. Jones. *Chemical Principles.* Freeman, 3nd edition, 2005.

[5] R. Setton, P. Bernier and S. Lafrant. *Carbon Molecules and Materials.* Taylor & Francis, 2002.

[6] T. D. Burchell. *Carbon Materials for Advanced Technologies.* Pergamon, 1999.

[7] H. W. Kroto, J. R. Heath, S. C. O'Brien, R. F. Curl and R. E. Smalley. $C_{60}$: Buckminsterfullerene. *Nature*, 318:162, 1985.

[8] M Endo, S. Iijima and M. S. Dresselhaus. *Carbon Nanotubes.* Pergamon, 1996.

[9] S. Reich, C. Thomsen and J. Maultzsch. *Carbon Nanotubes. Basic Concepts and Physical Properties.* Wiley, 2003.

[10] J. W. Mintmire, B. I. Dunlap and C. T. White. Are fullerene tubules metallic? *Phys. Rev. Lett.*, 68:631, 1992.

[11] P. Atkins and J. de Paula. *Atkins' Physical Chemistry.* Oxford University Press, 7th edition, 2002.

[12] A. Nish, J-Y. Hwang, J. Doig and R.J. Nicholas. Highly selective dispersion of single-walled carbon nanotubes using aromatic polymers. *Nature Nanotech.*, 640, 2007.

[13] W. I. Atkinson. *Nanocosm: Nanotechnology and the Big Changes Coming from the Inconceivably Small.* American Management Association, 1st edition, 2003.

[14] P. J. F. Harris. *Carbon Nanotubes and Related Structures.* Cambridge University Press, 1999.

[15] W. Krätschmer, L. D. Lamb, K. Fostiropoulos and D. R. Huffman. Solid $C_{60}$: A new form of carbon. *Nature*, 347:354, 1990.

[16] S. Iijima. Helical microtubules of graphitic carbon. *Nature*, 354:56, 1991.

[17] R. Bacon. Growth, structure and properties of graphite whiskers. *J. Appl. Phys.*, 31:283, 1960.

[18] S. Iijima, T. Ichihashi and Y. Ando. Pentagons, heptagons and negative curvature in graphitic microtubule growth. *Nature*, 356:776, 1992.

[19] S. Iijima and T. Ichihashi. Single-shell carbon nanotubes of 1-nm diameter. *Nature*, 363:603, 1993.

[20] D. S. Bethune *et al.* Cobalt-catalysed growth of carbon nanotubes with single-atomic-layer walls. *Nature*, 363:605, 1993.

[21] A. Thess *et al.* Crystalline ropes of metallic carbon nanotubes. *Science*, 273:483, 1996.

[22] P. Ball. The perfect nanotube? *Nature*, 382:207, 1996.

[23] P. Nikolaev, M. J. Bronikowski, R. K. Bradley, F. Rohmund, D. T. Colbert, K. A. Smith and R. E. Smalley. Gas-phase catalytic growth of single-walled carbon nanotubes from carbon monoxide. *Chem. Phys. Lett.*, 313:91–97, 1999.

[24] A. C. Clarke. *The Fountains of Paradise.* Harcourt, 1979.

[25] A. Bachtold, P. Hadley, T. Nakanishi and C. Dekkerdagger. Logic Circuits with Carbon Nanotube Transistors. *Science*, 294:1317, 2001.

[26] W. B. Choi, D. S. Chung, J. H. Kang, H. Y. Kim, Y. W. Jin, I. T. Han, Y. H. Lee, J. E. Jung, N. S. Lee, G. S. Park and J. M. Kim. Fully sealed, high-brightness carbon-nanotube field-emission display. *Appl. Phys. Lett.*, 75:3129, 1999.

[27] S. A. Curran, P. M. Ajayan, W. J. Blau, D. L. Carroll, J. N. Coleman, A. B. Dalton, A. P. Davey, A. Drury, B. McCarthy, S. Maier and A. Strevens. A Composite from Poly(m-phenylenevinylene-co-2,5-dioctoxy-p-phenylenevinylene) and Carbon Nanotubes: A Novel Material for Molecular Optoelectronics. *Adv. Mat.*, 10:1091, 1999.

[28] E. Kymakis and G. A. J. Amaratunga. Single-wall carbon nanotube/conjugated polymer photovoltaic devices. *Appl. Phys. Lett.*, 80:112–114, 2001.

[29] S. M. Lee and Y. H. Lee. Hydrogen Storage in Single Walled Carbon Nanotubes. *Appl. Phys. Lett.*, 76:2877, 2000.

[30] J. Kong, N. R. Franklin, C. Zhou, M. G. Chapline, S. Peng, K. Cho and H. Dai. Nanotube Molecular Wires as Chemical Sensors. *Science*, 287:622, 2000.

[31] G. W. Evans. Optical Properties of Carbon Nanotubes. *MPhil thesis, Oxford*, 2008.

[32] Y. Lin, F. Lu, Y. Tu and Z. Ren. Glucose Biosensors Based on Carbon Nanotube Nanoelectrode Ensembles. *Nano. Lett.*, 4:191, 2004.

[33] S. S. Wong, J. D. Harper, P. T. Lansbury and C. M. Lieber. Carbon Nanotube Tips: High-Resolution Probes for Imaging Biological Systems *J. Am. Chem. Soc.*, 120:603, 1998.

[34] T. Rueckes, K. Kim, E. Joselevich, G. Y. Tseng, C. L. Cheung and C. M. Lieber. Carbon Nanotube-Based Nonvolatile Random Access Memory for Molecular Computing. *Science*, 289:94, 2000.

[35] B. Yurdumakan, N. R. Raravikar, P. M. Ajayan and A. Dhinojwala. Synthetic gecko foot-hairs from multiwalled carbon nanotubes. *Chem. Comm.*, page 3799, 2005.

[36] N. M. Pugno. Towards a spiderman suit: large invisible cables and self-cleaning releasable superadhesive materials. *J. Phys.: Condens. Matter*, 19:395001, 2007.

[37] M. J. O'Connell. *Carbon Nanotubes. Properties and Applications.* Taylor & Francis, 2006.

[38] B. Hornbostel, M. Haluska, J. Cech, U. Dettlaff and S. Roth. *Arc Discharge and Laser Ablation Sythesis of Single-Walled Carbon Nanotubes.* NATO Science Series, vol. 222, 2006.

[39] Y. Oyama, Y. Saito, K. Sato, J. Jiang, G. G. Samsonidze, A. Gruneis, Y. Miyauchi, S. Maruyama, A. Jorio, G. Dresselhaus and M. S. Dresselhaus. Photoluminescence intensity of single-wall carbon nanotubes. *Carbon*, 44:873–879, 2006.

[40] S. M. Bachilo, L. Balzano, J. E. Herrera, F. Pompeo, D. E. Resasco and R. B. Weisman. Narrow (n,m)-distribution of single-walled carbon nanotubes grown using a solid supported catalyst. *J. Am. Chem. Soc.*, 125:11186–11187, 2003.

[41] K. Tanaka, T. Yamabe and K. Fukui. *The Science and Technology of Carbon Nanotubes*. Elsevier, 1999.

[42] J. C. Meyer, M. Paillet, G. S. Duesberg and S. Roth. Electron diffraction analysis of individual single-walled carbon nanotubes. *Ultramicroscopy*, 106:176–190, 2006.

# Chapter 2

# Theory

## 2.1 Structure

Current single-walled carbon nanotube production methods yield a range of nanotube diameters in a Gaussian-like distribution, where the mean diameter is dependent on growth conditions such as temperature and pressure. The relationship between the structure and nanotube diameter is complicated by the angle of the carbon lattice with respect to the nanotube axis. Properties such as electronic nature of a nanotube species are highly dependent on the precise atomic geometry of the structure in question and cannot be simply deduced from it's diameter. A SWNT with a diameter of 1nm may behave as a semiconductor with a band-gap of 0.8eV or it may be metallic. This necessitates a rigorous classification system, one from which all the required information such as diameter and lattice angle for the precise structure in question can be easily elucidated.

It is useful to simplify the issue of nanotube classification by considering the structure of graphene. Graphene is composed of a plane of carbon atoms which are covalently attached to each other with bond angles of 120°. This arrangement of atoms comes from the hybridisation of the *2s* electron with two of the *2p* electrons to give three $sp^2$ orbitals. Although carbon nanotubes are not planar, and therefore have some small loss of $sp^2$ character and increase in $sp^3$ character, for the purposes of structural classification their curvature can be neglected.

The classification system which is now universally accepted starts with the graphene basis vectors $\mathbf{\hat{a}_1}$ and $\mathbf{\hat{a}_2}$ as they are shown in figure 2.1. These vectors are related to the carbon bond length, $a_{c-c}$, by

$$\mathbf{\hat{a}_1} = \mathbf{\hat{a}_2} = \sqrt{3}a_{c-c}. \tag{2.1}$$

A carbon nanotube may be generated by the rolling of a graphene sheet along a vector $\mathbf{C_h}$, whereby the length and angle of this vector with respect to the hexagonal lattice determine the distinct structure of the different nanotube types. The vector $\mathbf{T}$ in figure 2.1 lies normal to $\mathbf{C_h}$ and indicates the axis of the carbon nanotube. The different possibilities of SWNT structure are described by the equation

$$\mathbf{C_h} = n\mathbf{\hat{a}_1} + m\mathbf{\hat{a}_2} \tag{2.2}$$

where $\mathbf{C_h}$ is known as the chiral vector. The vectors $\mathbf{\hat{a}_1}$ and $\mathbf{\hat{a}_2}$ are again the graphene basis vectors

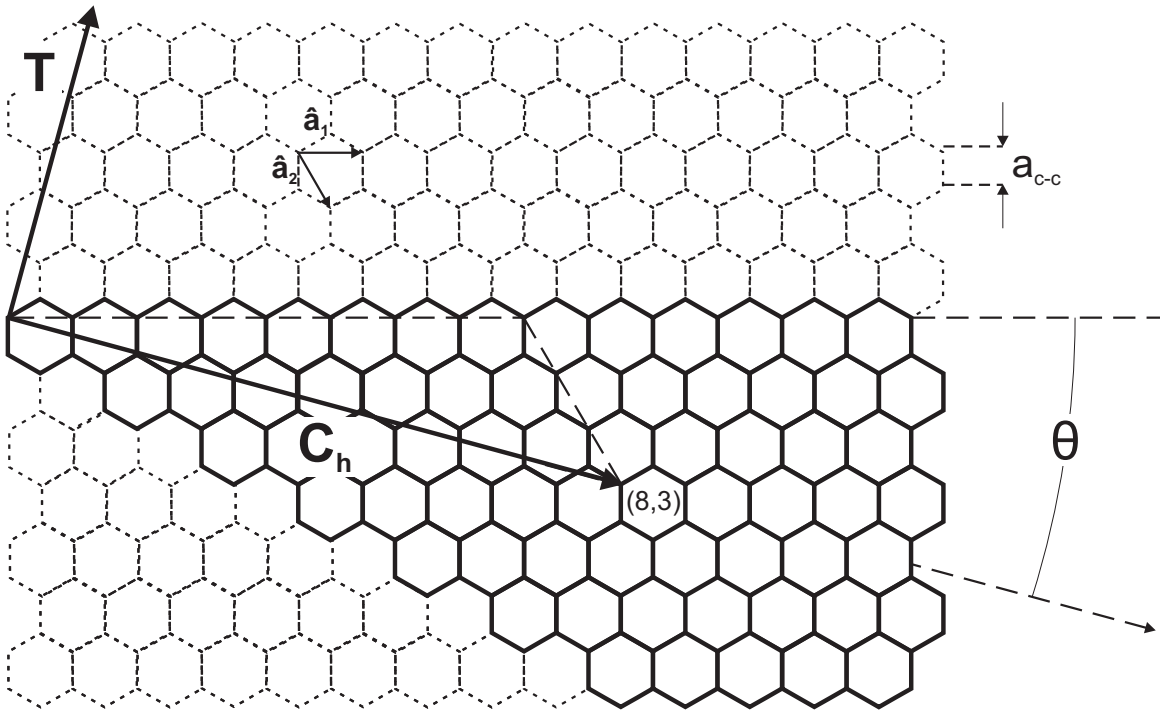


Figure 2.1: Hexagonal lattice indicating the fundamental parameters of the coordinate system on which the carbon nanotube structure models and nomenclature is based. The (8,3) species of SWNT is highlighted due to convenience and the fact that it is a constituent semiconducting species of the real samples which have been studied here.

and their preceding integers, $n$ and $m$, correspond to the distinct allowed geometries of SWNT. From these integers it is possible to determine all the necessary structural information about the nanotube in question. The magnitude of the chiral vector, $\mathbf{C_h}$, equates to the circumference of the tube. Thus, assuming we know the carbon-carbon bond length $a_{c-c}$, we can find the diameter of the SWNT from the following equation

$$d = \frac{|\mathbf{C_h}|}{\pi} = \frac{\sqrt{3}a_{c-c}}{\pi}\sqrt{n^2 + nm + m^2}. \tag{2.3}$$

The chiral vector used schematically in figure 2.1 corresponds to a SWNT with the indices $n = 8$ & $m = 3$. For a carbon-carbon bond length of 0.142nm this produces a nanotube with a diameter equal to 0.77nm. The same set of indices, hereafter referred to as the 'chiral indices', can also be used to determine the angle at which the graphene sheet is rolled up with respect to the hexagonal lattice

$$\theta = cos^{-1}\frac{2n + m}{2\sqrt{n^2 + nm + m^2}}. \tag{2.4}$$

The angle, $\theta$, is referred to as the chiral angle. For the $(8, 3)$ SWNT this equation gives a chiral angle of 15.3°. Unique SWNTs are only found with angles which lie between 0° and 30°, angles greater than this produce tubes which are the symmetrical equivalents of those at smaller angles.

Three distinct classes of SWNT are often referred to in the literature. These are summarised in Table 2.1 with examples of each of these nanotube classes shown in figure 2.2.

The majority of SWNTs in a given sample are known as chiral SWNTs, so called because they have a chiral angle between 0° & 30°. Figure 2.3 shows a schematic called a 'Graphene Sheet Map'. It indicates the chiral indices as hexagons which correspond to a specific chiral vector and hence nanotube type. This useful representation will be used in later chapters to describe the populations of specific species in real nanotube samples and how they can be affected by different stabilisation agents when in liquid suspension.

| Chiral Indices | Angle | Class Name |
|---|---|---|
| $(n, 0)$ | $\theta = 0°$ | Zig-zag |
| $(n, m)$ | $0° < \theta < 30°$ | Chiral |
| $(n, n)$ | $\theta = 30°$ | Armchair |

Table 2.1: The three chiral classes of SWNT

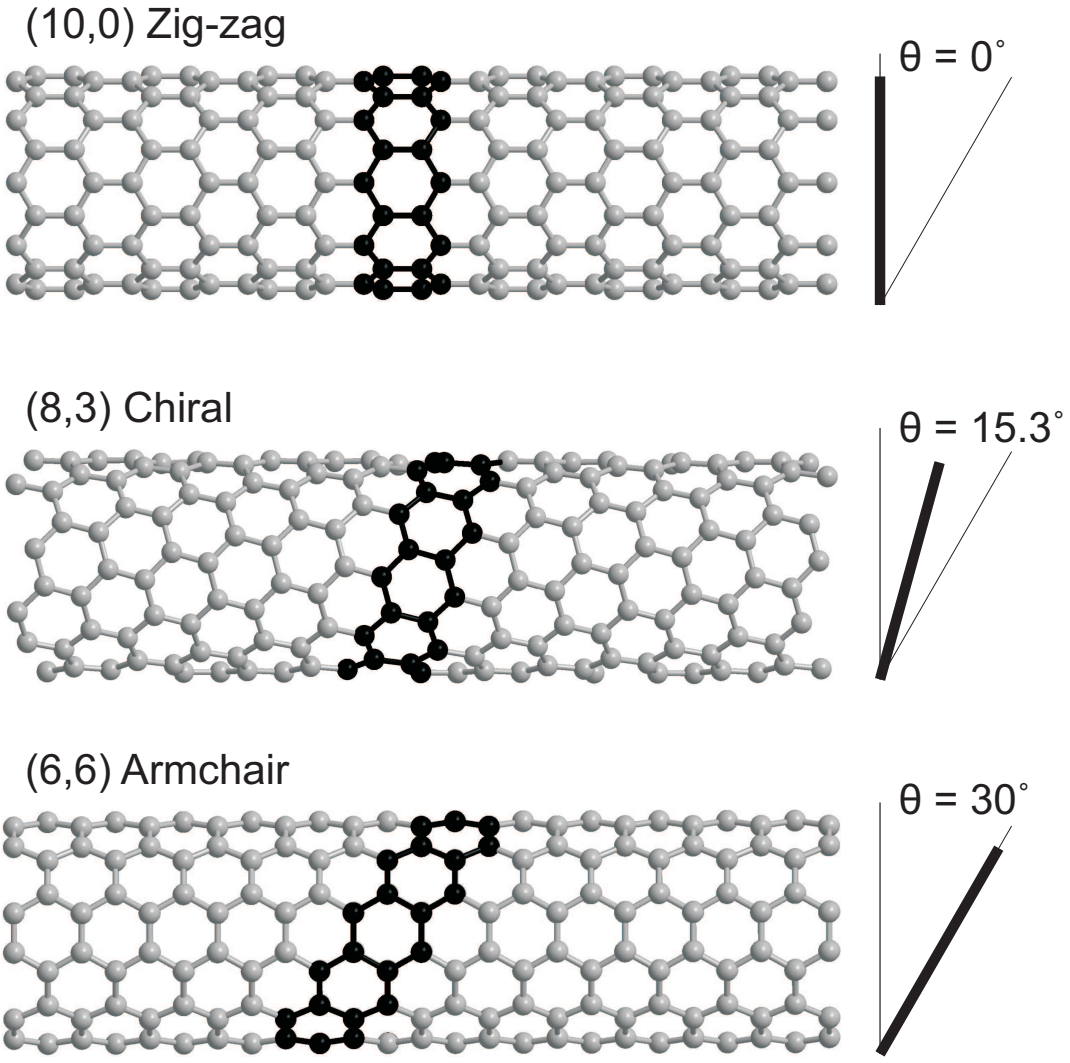


Figure 2.2: The three classes of carbon nanotubes are easily distinguished by the angle which the indicated ring of carbon atoms makes with the perpendicular to the nanotube axis.

Few characterisation techniques are sensitive enough to unambiguously determine the structure of an individual SWNT. Some experienced researchers, however, have managed to use scanning tunneling microscopy and even high resolution transmission electron microscopy to image the atomic structure of the nanotubes. Images such as those in the work of Lieber et al. [1], allow the diameter and chiral angle to be determined, confirming the validity of equations such as (2.3) and (2.4).

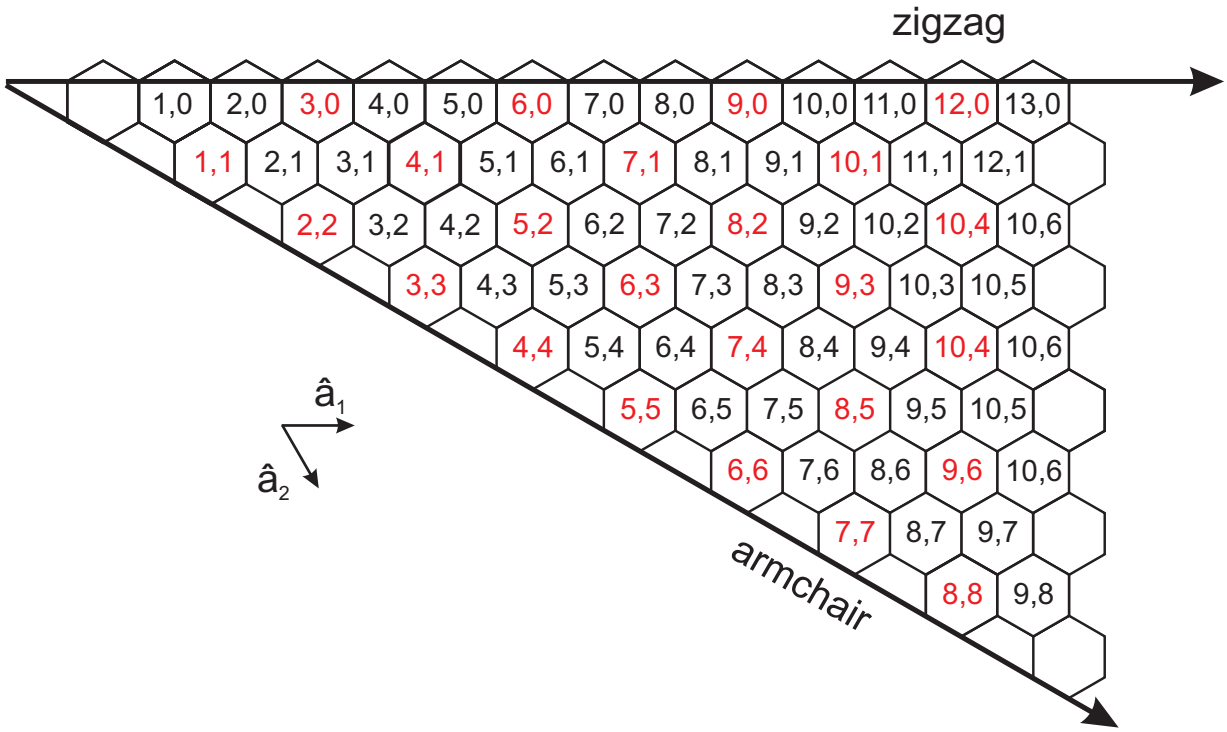


Figure 2.3: A similar illustration as that in figure 2.1 showing many more SWNT indices. The black indices are semiconducting species and the red are the metallic species. These figures are called graphene sheet maps and will be used in later chapters to describe the relative concentrations of the various nanotubes.

## 2.2 Electronic Properties

### 2.2.1 Graphene

The electronic structure of single-walled carbon nanotubes is arguably one of the most important aspects of their physical nature. Derived from their unique atomic configuration, it yields novel physical properties such as the ability of subtly different SWNT structures to be either metallic or semiconducting and to quantum mechanical phenomena such as the Aharanov-Bohm effect [2]. The electronic properties are what have sparked the interest of technologists, keen to exploit SWNTs as molecular wires or transistors for nanoscale logic circuits. Of primary relevance to the work presented in this thesis is the effect which the electronic band structure has on the optical properties of SWNTs. An understanding of the trends which determine the dependencies of the band structure on the nanotube diameter and chiral angle was of paramount importance to the interpretation of the initial optical spectra obtained as part of the studies detailed here. Whilst theoretical methods for precisely predicting the observed optical energy gaps (taking into full account the intricacies of the excitonic behavior in SWNTs) are beyond the scope of this thesis it is hoped that some of the useful underlying principles can be demonstrated in the following section.

The electronic properties of SWNTs can be derived from the band structure of graphene. These detailed calculations were first worked out in 1947 by P. R. Wallace [3], who obtained the following expression for the energy, $E_{2D}$, of an electron at a point in the lattice described by the orthogonal wavevectors $k_x$ and $k_y$

$$E_{2D}(k_x, k_y) = \pm\gamma_0\left(1 + 4cos^2\left(\frac{k_y a}{2}\right) + 4cos\left(\frac{\sqrt{3}k_x a}{2}\right)cos\left(\frac{k_y a}{2}\right)\right)^{-\frac{1}{2}} \tag{2.5}$$

where $\gamma_0$ is the nearest neighbour transfer integral and $a$ is the length of the graphene basis vector.

Using empirically determined values for the constants above ($\gamma_0 = -2.79$eV and $a = \sqrt{3}a_{c-c} = 0.246nm$)[4] equation 2.5 can be solved to yield an elegant representation of the $\pi$-electronic energy surfaces for graphene. Illustrations of the solution of this equation are given in Figure 2.4.

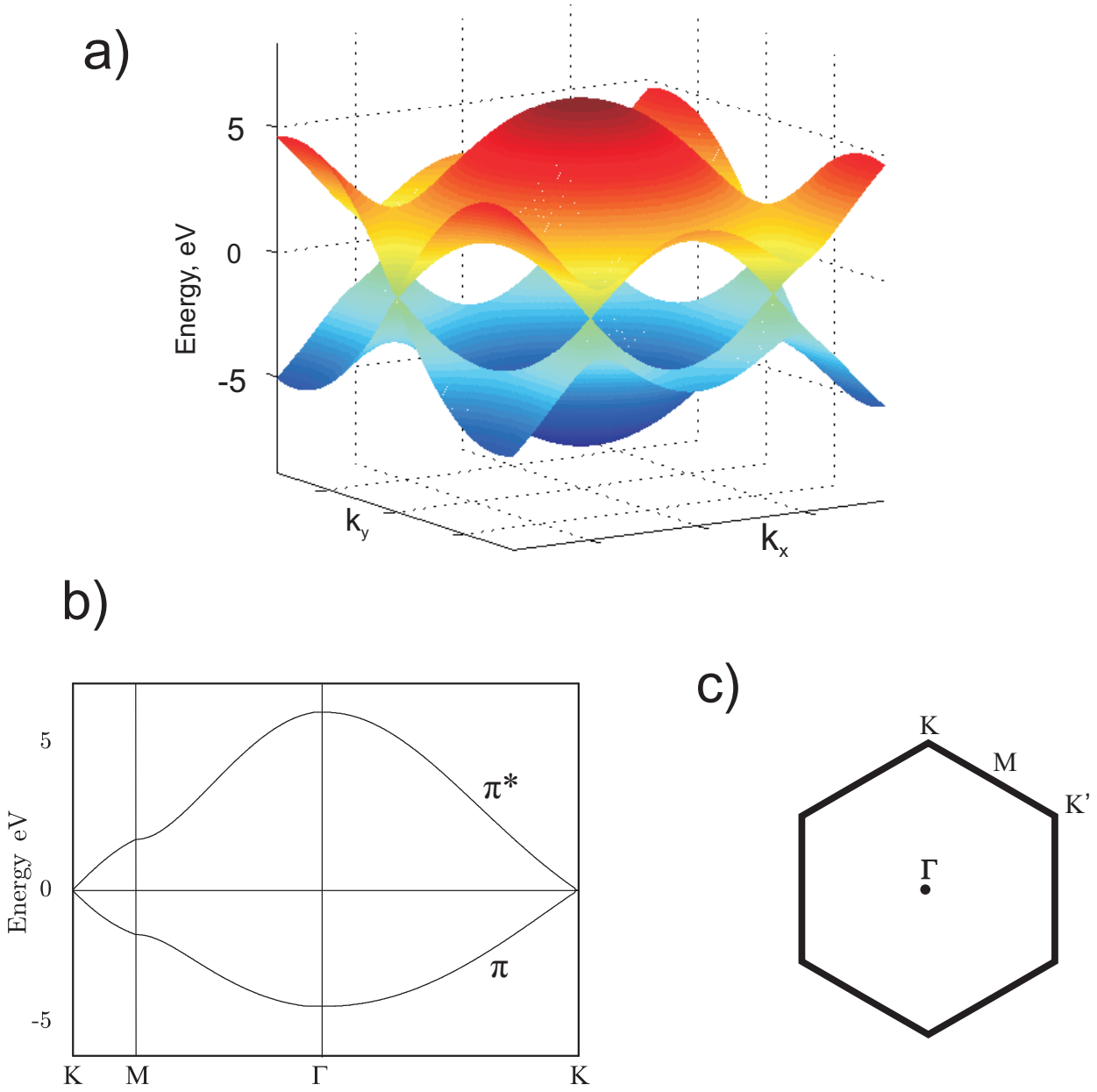


Figure 2.4: Solution of the dispersion relation shown in equation 2.5. Part **a)** shows the conduction and valence bands plotted in 3D as an energy surface. This is then given as a reduced representation in part **b)** where the directions used are indicated by the Γ, M and K points shown in **c)**. The $\pi$ and $\pi^*$ notation is used to denote the highest occupied and lowest unoccupied molecular orbitals respectively (HOMO and LUMO levels).

### 2.2.2 Nanotubes

The solution of the dispersion relation for graphene (equation 2.5) assumes the lattice is a 2D sheet of infinite length. For carbon nanotubes there is a boundary imposed in one of these directions (due to the finite circumference), whilst along the axial direction it may remain effectively infinite. The consequence of this boundary condition is that the electron wavefunction is restricted to an integer multiple of wavelengths around the tube circumference. All other possibilities vanish due to interference. This results in the quantization of the allowed wavevectors around the nanotube with the number and orientation of these wavevectors being dependent on the chiral indices $(n, m)$ of the SWNT. This approach to solving the nanotube electronic band structure is known as the zone-folding approximation. The quantization of the allowed wavevectors may be visualized as taking a number

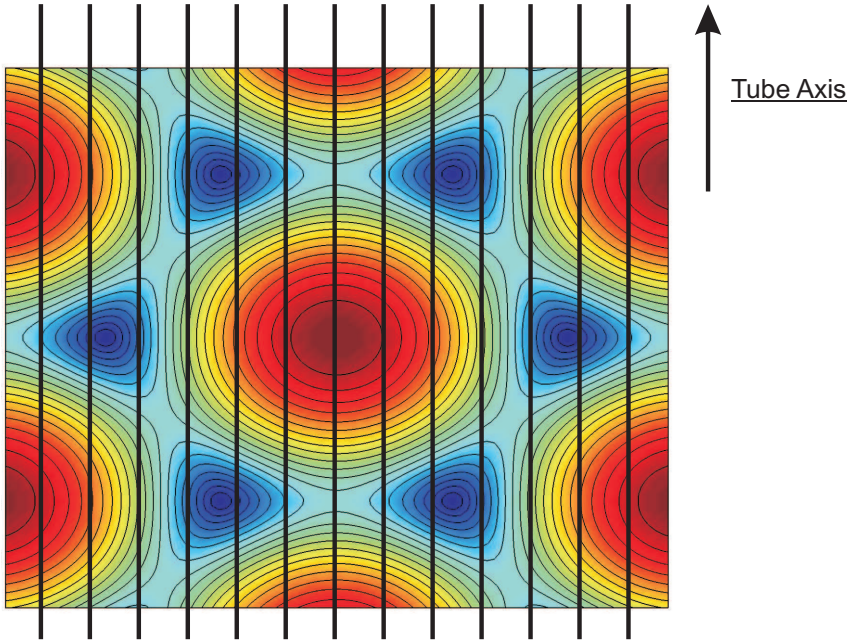


Figure 2.5: The $\pi^*$ energy surface from figure 2.4 as viewed from above and plotted with contour lines. The red colour represents a high energy and the blue is low energy. The parallel lines indicate regularly spaced sections where the graphene energy plot is cut due to the restriction in the allowed wavevectors in a SWNT. This is imposed by the quantization that arises from the boundary condition of a finite circumference and the nature of the electron wavefunction.

of sections across the energy surface of graphene, as in Figure 2.5. Each of these parallel lines will be a fixed distance apart,e where the maximum number of wavevectors around the nanotube is related to the number of atoms in the unit cell [5]. Thus nanotubes with ever increasing diameters approach the solution found for 2D graphene. Nanotubes with smaller diameters however have greater distance

between the wavevectors and consequently a larger energy separation between electronic levels. If one of the SWNT wavevectors passes through graphene's degenerate $K$-point then the tube will be metallic. Otherwise the SWNT will be semiconducting, with a small bandgap determined by the wavevector which passes closest to the $K$-point. In fact, most of the physical effects observed in graphene and SWNTs are determined by the allowed electronic states close to this point with a linear dispersion relation being a good approximation for the $\pi$-bands around the Fermi level. The band

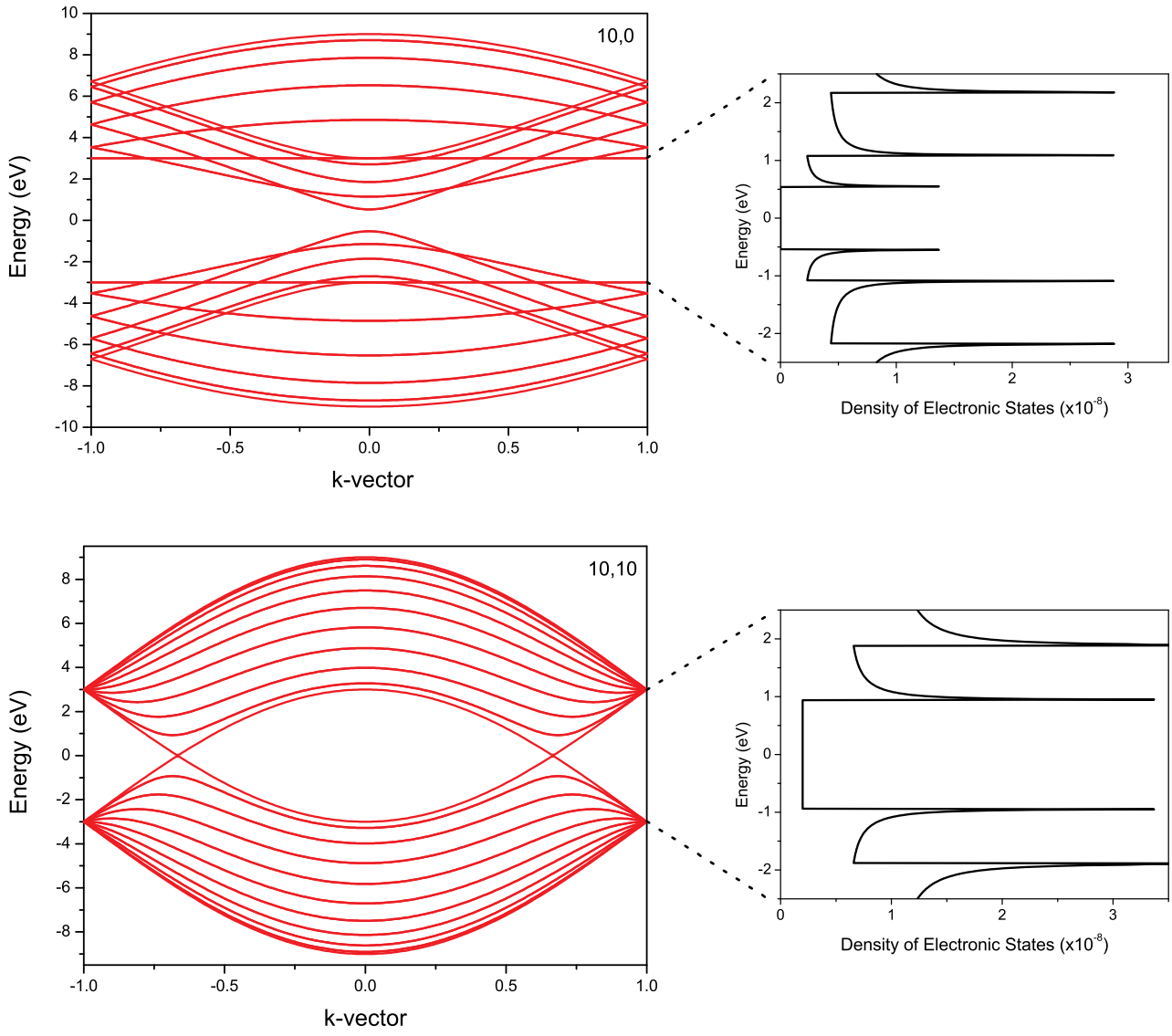


Figure 2.6: The electronic band structure and density of states for (10,0) and (10,10) SWNTs as calculated using a simple tight binding model. The Fermi level is normalised to a value of zero.

structure and density of states for (10,0) and (10,10) nanotubes are shown in Figure 2.6. Whilst this picture of the nanotube's electronic properties makes a good approximation to the general behavior of the optical properties of SWNTs, for a more precise model we need to include the effect of electron-hole and electron-electron interactions [6]. Nonetheless, many of the trends in the variation of the energy

gaps across the distinct nanotube structures can still be explained using approximations within the single particle model. The first of these approximations is that the bandgap is inversely proportional to the diameter

$$E_g = \frac{2\gamma_0 a_{c-c}}{d} \tag{2.6}$$

where $\gamma_0$ is the nearest neighbour transfer integral, $a_{c-c}$ is the carbon-carbon bond length. The second approximation is that the ratio of the first and second energy transitions is roughly equal to two

$$\frac{E_{22}}{E_{11}} \approx 2. \tag{2.7}$$

Whilst these approximations have limited use in interpreting the actual experimental results, they do offer a guide to the general behavior of the energy levels in SWNT systems. In reality, deviations from equations 2.6 and 2.7 occur due to the chiral angle of the SWNTs. For example, the semiconducting Zig-zag SWNTs ($\theta = 0$) have a bandgap which is inversely proportional to their diameter; however, as the chiral angle is increased, the wavevectors rotate with respect to the K-point. This causes them to intersect the graphene energy surface (as in figure 2.7) along a different gradient and so have a unique bandgap-diameter dependence for every chiral angle. If the energy contours close to the K-point were circular, the change in chiral angle wouldn't cause this deviation. This is known as the trigonal warping effect [7].

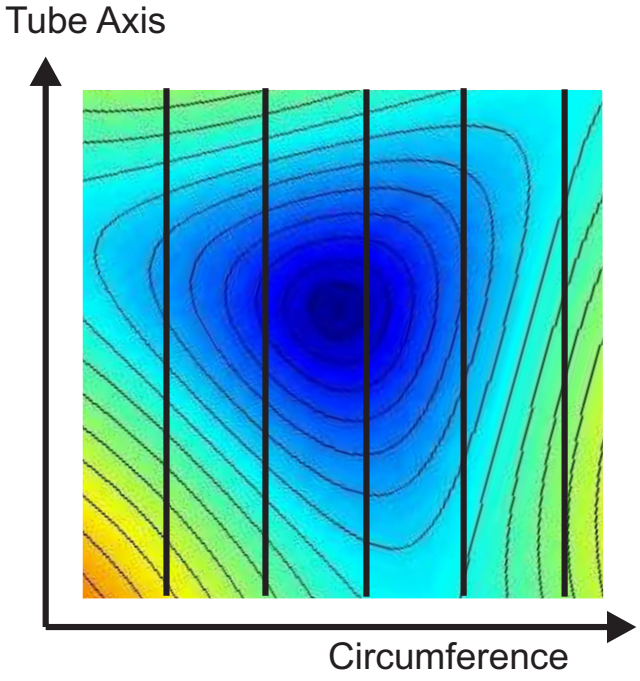


Figure 2.7: This picture of the wavevector sections intersecting the graphene surface reveals the origin of the deviations from the simple approximations of equations 2.6 and 2.7.

As can be seen in figure 2.8 the positions of the SWNT energy gaps are spread to either side of a median line. The side of this line on which the various species are located is determined by the sign ($q$=$\pm$1) which satisfies the following relationship

$$n - m = 3p + q \tag{2.8}$$

where $p$ is a positive integer. The physical origin of this difference comes from the whether the bandgap determining wavevector intersects the energy surface on the inside or on the outside of the $K$-point with respect to the centre of the Brillouin zone. Although the distance from $K$-point to wavevector on either side is the same in $k$-space for identical diameters of SWNT, the asymmetry of the energy surface causes differences in the respective energy gaps. This results in a deviation from the constant ratio behaviour between $E_{11}$ and $E_{22}$ which is predicted by equation 2.7. The magnitude of this deviation is determined by the chiral angle with small angle SWNTs being furthest from the median. As can be seen in figure 2.8 a global reduction of the ratio from the value of 2 is observed by in optical spectroscopy measurements. This has been shown to be due to excitonic effects [8].

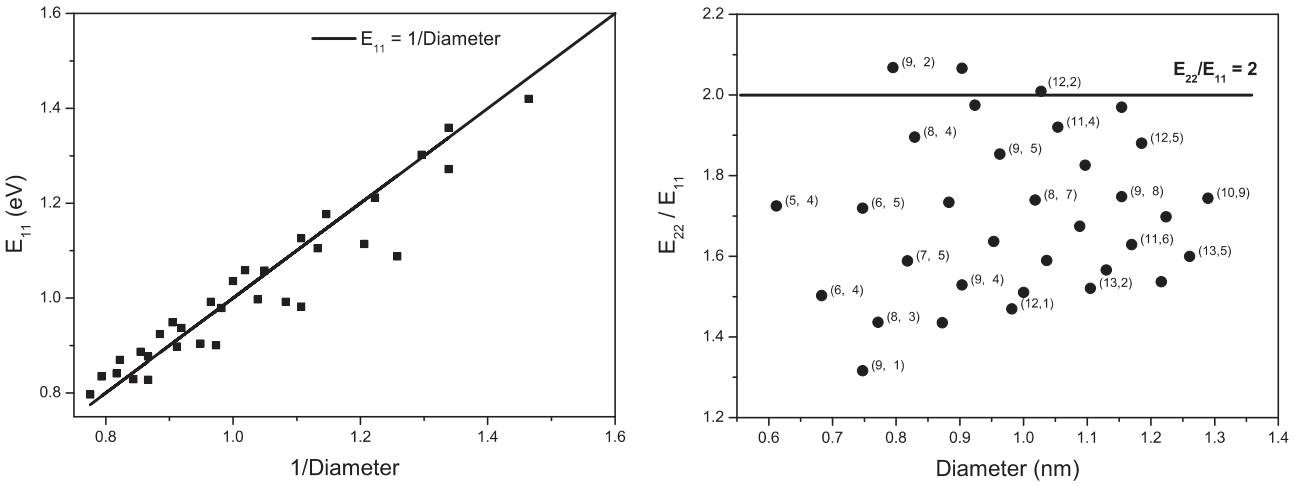


Figure 2.8: The first energy transition (bandgap) for SWNTs is roughly inversely proportional to the diameter with points either side of the line arising due to the chiral angle. The spread of the ratio between $E_{11}$ and $E_{22}$ is shown in the plot on the right. Excitonic effects blue-shift $E_{11}$ more than $E_{22}$ resulting in the median ratio being lower than 2. The data shown have been taken from experimental results.

The dependence of the $1^{st}$ and $2^{nd}$ energy gaps on diameter is shown in Figure 2.9. Plotting these gaps against each other, and in terms of wavelength, is of major importance to the characterisation of SWNTs [9]. As can be seen, no overlapping points are present. This implies that, whilst distinct nanotube species may have similar bandgaps, the ratio of the energy levels leads to well separated

features. Optical spectroscopic techniques exist which are simultaneously sensitive to both transitions, allowing the precise determination of the structures present in a given sample. The relevant technique developed and used to great effect in the characterisaction of SWNTs is known as photo-luminescence excitation (PLE) mapping.

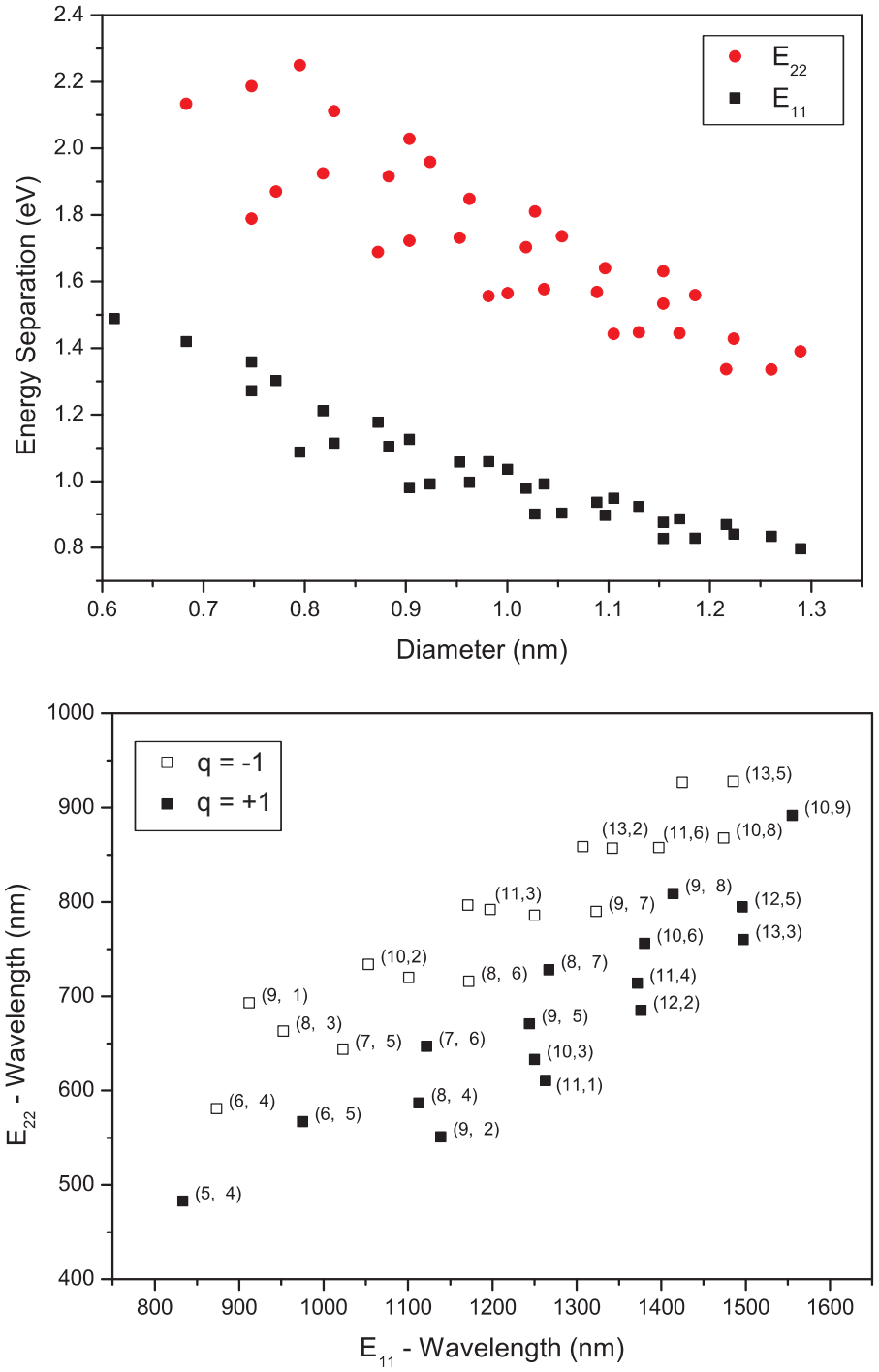


Figure 2.9: Further ways of plotting the empirically determined SWNT energy gaps. The lower plot is significant as it is shown in the same form as much of the spectroscopic data in later chapters. These plots are often referred to as Kataura plots in the literature [10].

## 2.3 Optical Transition Rules and Excitonic Behavior

An important element of optical spectroscopy in carbon nanotubes is the presence of selection rules for the allowed transitions. These rules may be derived from symmetry arguments and are summarized under two categories. First is the general rule that only vertical transitions are allowed, $\Delta k = 0$. The second concerns the polarization of light with respect to the nanotube axis, $z$. For this we find that $\Delta i = 0$ for $\mathbf{E} \parallel z$. and $\Delta i = \pm 1$ for $\mathbf{E} \perp z$, where $i$ is the quantum number of the energy level. Whilst both rules are pertinent to the optical absorbance and photoluminescence work presented in later chapters, we find that the second rule has some notable interest. Experimentally, it is evident that transitions between bands of the same quantum number, $i$, dominate over all other interband possibilities. These dominant features are often abbreviated to $E_{11}$ transitions (between the first pair of energy levels), $E_{22}$ transitions (between the second pair of energy levels) and so on. However, recent work has shown that it is also possible to observe the weak $E_{12}$ (and $E_{21}$) optical transitions by using polarized light [11]. These observations were made from PLE maps, which record excitation of an electron from the first valence band to the second conduction band and subsequent recombination with the emission of a photon having energy $E_{11}$.

Excitons are a key feature of spectroscopic studies in nanoscale systems due to the large role which they play in determining the energy transitions. They form in semiconductors and macro-molecules from the association of opposite charges. These charges may arise through photo-excitation or may initially exist as free carriers, as they do in light emitting diodes. In the case of photo-excitation, an electron's energy is elevated to a conduction band level by absorption of a photon, leaving a hole in the valence band. If the spatial separation between these charges is significant then their interaction may be negligible. However, if they are sufficiently close, they experience a Coulombic attraction which binds them into an electron-hole pair known as an exciton. When the dielectric constant of the material is high then the screening tends to reduce the Coulomb potential between the electron and hole. This has the result of increasing the radius of the exciton, creating what is called a Mott-Wannier type exciton. When the dielectric constant is low, or where the particles are confined to the same unit cell, the exciton has a much smaller radius. These smaller excitons typically have a binding energy of an order of magnitude higher and are know as Frenkel excitons.

Simple models of excitons can be produced using the hydrogenic model and assuming homogeneous systems with no boundaries. If the free particle bandgap in such a system is represented by $E_g$ then we find the binding energy from the following

$$E_b = E_g - E_x \tag{2.9}$$

where $E_b$ is the binding energy and $E_x$ is the exciting photon's energy. In bulk semiconductor materials with high dielectric constant the exciton binding energy is small, typically around 27meV for CdS, 5.1meV for InP and 4.9meV for GaAs [12]. At room temperature this energy separation is comparable to or smaller than the thermal energy and so, in order to observe excitonic effects in conventional semiconductors, we need to go to cyrogenic temperatures. However, the added confinement in nanoscale systems results in a large increase in the exciton binding energy, with quantum dots having $E_b$ of 50-200meV and conjugated polymers and carbon nanotubes being of the order of 400meV [13]. This is substantially larger than $kT$ at room temperature (only around 25meV) and so excitonic effects dominate the optical spectra at all temperatures for these systems [14].
If the simple picture represented by equation 2.9 were valid for SWNTs then the exciton binding energy would be equal to around half the energy gap and we would observe much lower transition energies in the optical spectra than a theory such as tight binding model suggests. In the real system however, it is revealed that the electron-electron interactions also play a large role in determining the transition energies. This has a significant importance where changes in the local dielectric environment of the SWNTs induce shifts in the spectral peak positions [15]. These shifts can be explained through almost equal but opposite alterations in the screening of the $e-h$ and $e-e$ interactions producing a net red-shift or blue-shift depending on the sign of the dielectric change.

The detailed description of the excitonic states in SWNTs is in fact quite complex. The wavevectors in SWNTs symmetrically intersect the graphene energy surface on either side of the Brillouin zone (as in figure 2.5). This gives rise to doubly degenerate valence and conduction bands. Out of this, four singlet excitons can be formed: two higher energy excitations which have finite circumferential $k$-vector ($\alpha$ states) and two lower zero momentum states, one state with odd parity ($\beta$ state) and one with even parity [16] ($\delta$ state). To be optically active with linear polarization, the excitonic wavefunction must be of odd parity and the $k$-vector must be close to zero. Thus, both the upper $\alpha$-states cannot decay radiatively.

The odd parity $\beta$ exciton is allowed to decay radiatively and hence is known as a 'Bright' exciton. However, the K-K$'$ Coulomb mixing that splits the lower exciton states results in the even parity exciton being lower in energy [17]. This state cannot emit radiatively and is known as a 'Dark' exciton. Its presence below the Bright state is thought to contribute to the reduced photoluminescence yield observed in nanotubes with respect to other similar systems, such as organic polymers and dyes. Figure 2.10 shows an energy level diagram for the excitonic states.

The magnitude of the energy splitting between the lower excitonic states is the subject of much interest and debate in the SWNT photo-physics community [18, 19]. Recent magneto-photoluminescence experiments, which are the subject of chapter 7 in this thesis, have determined the value of this splitting ($\Delta_x$) to be of the order of 2-6meV. It is significant that the splitting is smaller than the thermal energy at room temperature as otherwise the carriers would be unable to populate the Bright state and photoluminescence would not be observable [20]. However, as SWNTs are cooled their emission intensity falls as $kT$ approaches $\Delta_x$. This is in contrast to conventional semiconductors where the luminescence yield is maximized as T$\rightarrow$0.

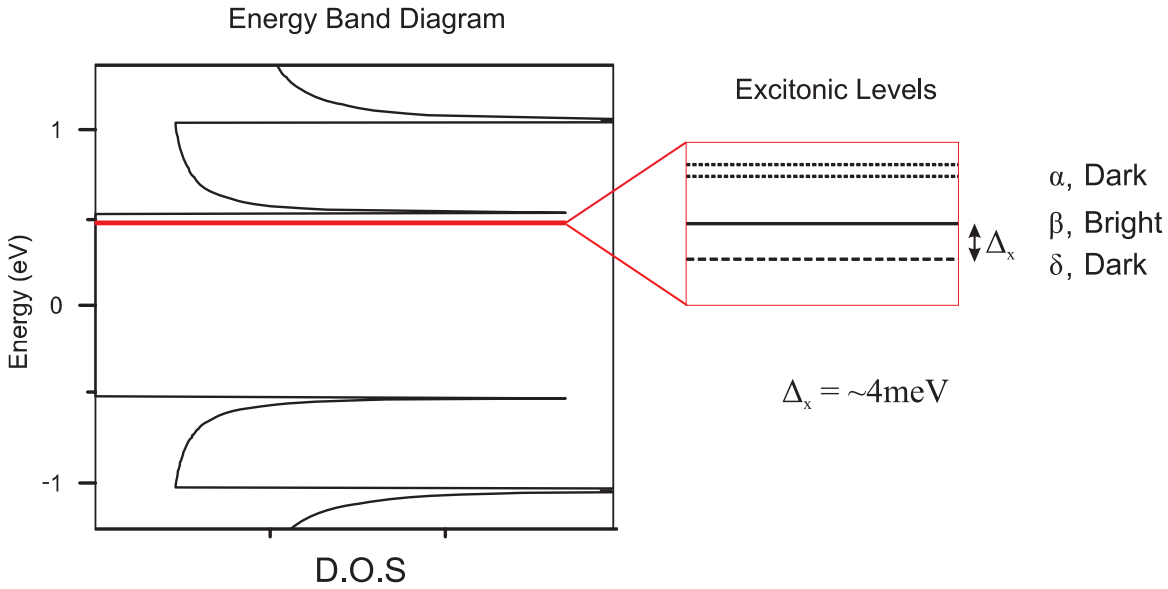


Figure 2.10: A band diagram showing the detail of the singlet excitonic levels on the standard SWNT density of states figure.

# Bibliography


[1] T. W. Odom, J-L. Huang, P. Kim and C. M. Lieber. Atomic structure and electronic properties of single-walled carbon nanotubes. *Nature*, 391:62, 1998.

[2] S. Zaric, G. N. Ostojic, J. Kono, J. Shaver, V. C. Moore, M. S. Strano, R. H. Hauge, R. E. Smalley and X. Wei. Optical Signatures of the Aharonov-Bohm Phase in Single-Walled Carbon Nanotubes *Science*, 21:1129, 2004.

[3] P. R. Wallace. The band theory of graphite. *Physical Review*, 71:622–634, December 1947.

[4] S. Reich, C. Thomsen, J. Maultzsch and P. Ordejn. Tight-binding description of graphene. *Phys. Rev. B*, 66:035412, 2002.

[5] S. Reich, C. Thomsen and J. Maultzsch. *Carbon Nanotubes.* Wiley, 2004.

[6] C.L. Kane and E.J. Mele. Electron interactions and scaling relations for optical excitations in carbon nanotubes. *Phys. Rev. Lett.*, 93:197402, 2004.

[7] R. Saito, G. Dresselhaus and M. S. Dresselhaus. Trigonal warping effect of carbon nanotubes. *Phys. Rev. B*, 61:2981–2990, 2000.

[8] J. Maultzsch, R. Pomraenke, S. Reich, E. Chang, D. Prezzi, A. Ruini, E. Molinari, M.S. Strano, C. Thomsen and C. Lienau. Exciton binding energies in carbon nanotubes from two-photon photoluminescence. *Phys. Rev. B.*, 72:241402, 2005.

[9] S. M. Bachilo *et al.* Structure-assigned optical spectra of single-walled carbon nanotubes. *Science* 298:2361–2366, 2002.

[10] H. Kataura, Y. Kumazawa, Y. Maniwa, I. Umezu, S. Suzuki, Y. Ohtsuka and Y. Achiba. Optical properties of single-wall carbon nanotubes. *Synth. Metals*, 103(1):2555–2558, 1999.

[11] K. C. Chuang, A. Nish, J. Y. Hwang, G. Evans and R. J. Nicholas. An experimental study of Coulomb corrections and single particle energies for single-walled carbon nanotubes using cross-polarized photoluminescence. *Phys. Rev. B*, In Press 2008.

[12] G. D. Scholes and G. Rumbles. Excitons in nanoscale systems. *Nature. Mat.*, 5:683-696, 2006.

[13] M. Pope and C. E. Swenberg. *Electronic processes in organic crystals and polymers.* Oxford University Press, Oxford, 2 edition, 1999.

[14] V. Perebeinos, J. Tersoff and P. Avouris. Scaling of excitons in carbon nanotubes. *Phys. Rev. Lett.*, 92:257402, 2004.

[15] T. Hertel, A. Hagen, V. Talalaev, K. Arnold, F. Hennrich, M. Kappes, S. Rosenthal, J. McBride, H. Ulbricht and E. Flahaut. Spectroscopy of single- and double-wall carbon nanotubes in different environments. *Nano. Lett.*, 5:511–514, 2005.

[16] S. Zaric, G. N. Ostojic, J. Shaver, J. Kono, O. Portugall, P. H. Frings, G. L. J. A. Rikken, M. Furis, A. Crooker, X. Wei, V. C. Moore, R. H. Hauge and R. E. Smalley. Excitons in carbon nanotubes with broken time-reversal symmetry. *Phys. Rev. Lett.*, 96:016406, 2006.

[17] T. Ando. Effects of valley mixing and exchange on excitons in carbon nanotubes with aharanov-bohm flux. *J. Phys. Soc. Japan*, 75:024707, 2006.

[18] I. B. Mortimer and R. J. Nicholas. The role of bright and dark excitons in the temperature dependent photoluminescence of carbon nanotubes. *Phys. Rev. Lett.*, 98:027404, 2007.

[19] J. Shaver, J. Kono, O. Portugall, V. Krystic, G. L. J. A. Rikken, Y. Miyauchi, S. Maruyama and V. Perebeinos. Optical signatures of the aharanov-bohm phase in single-walled carbon nanotubes. *Nano Letters*, 7:1851, 2007.

[20] V. Perebeinos, J. Tersoff and P. Avouris. Radiative lifetime of excitons in carbon nanotubes. *Nano. Lett.*, 5:2495, 2005.

# Chapter 3

# Sample Preparation

## 3.1 Liquid Phase Dispersion

Investigation of carbon nanotube samples is limited by the ability to discern the characteristics of individual SWNTs in ensembles of many species. All characterisation methods thus require novel sample preparation procedures which have been specially developed by researchers in this field to counter the challenges posed by working with these materials. These efforts are truly multidisciplinary as cutting edge methods are borrowed from materials science, chemistry and biochemistry, then applied by physicists to produce samples which can be probed experimentally.

Many of the novel successes presented in this thesis have come from optimizing the preparation procedure to produce better samples for optical characterisation through UV-Vis-IR absorbance and photoluminescence spectroscopy. This work has been cyclical in its evolution. Better samples have allowed us to look at finer and finer details in the optical spectra. This motivation then gives us new features to optimize for with the preparation methods. Over time, a 'tool-box' of methods has been developed for preparing samples which are most suited to a particular study. For example, where we want to have very narrow diameters of tubes to study large bandgap SWNTs we can use material grown by a certain technique. Or if, on the other hand, we want nanotubes of a high chiral angle, then it is a matter of using a particular purification agent.

Another motivation for preparing the samples by different methods is that having a variety of materials in which to place the nanotubes provides a way of controllably perturbing their physical properties. Since single-walled nanotubes are mono-layer surfaces, interactions with the environment in which they are in contact will strongly effect their behavior. Examples are shown later in the charge-transfer experiments, where one local environment is found to remove electrons from the nanotube and another donates electrons. Also shown in the experiments are shifts in optical transitions which occur due to dielectric changes in the local environment and shifts in the electronic bandgap from external strain being imposed on the nanotube lattice.

All commercially available nanotube samples arrive as black powder (shown in chapter 1; figure 4). This black powder has the appearance of fine soot with no distinguishable structure even under the most powerful optical microscopes. However, under TEM it can be seen that the SWNTs exist in

| *Name* | *Growth Method* | Diameters (nm) | Supplier |
|---|---|---|---|
| 'HiPCO' | High Pressure disproportionation of Carbon Monoxide (Iron catalyst) | 0.80 - 1.25 | Carbon Nanotech Inc |
| 'CoMoCAT' | Disproportionation of Carbon Monoxide (Cobalt-Molybdenum catalyst) | 0.75 - 1.00 | Southwest Nanotechnologies |
| 'Laser vap.' | Laser Vaporization (Nickel-Yttrium *or* Rhodium-Platinum catalyst) | 1.10 - 1.30 | MPI Stuttgart |
| 'Arc' | Arc Discharge (Nickel-Yttrium catalyst) | 1.10 - 1.60 | MPI Stuttgart |

Table 3.1: The main varieties of SWNTs used.

bundles of many tightly bound individual species [1]. The bonds between the nanotubes come from van der Waals forces and, though generally weak in nature, for nanotubes of 500nm in length the total intertube binding energy has been calculated to be over 400eV [2]. This is roughly the equivalent energy to one carbon-carbon double bond for every 10nm of nanotube length.

Individualizing the SWNTs is necessary not just to explore their intrinsic physical properties but also from a point of view of applications. A major benefit of SWNTs over other materials is the high surface area which they possess, a benefit which is compromised if the nanotubes remain in bundles. Overcoming the aggregation is possible by dispersing the SWNTs in an appropriate solvent. Whilst some researchers have shown efficient dispersions in carefully selected solvents [3], it is most common to use an additive in the liquid phase which aids the dispersion. The standard dispersing method for this utilizes a surfactant such as the ionic sodium dodecylsulfate (SDS) in water. Many studies have been done on the effect which using different ionic aqueous surfactants has on the dispersion but few have been shown to work better than the original standard. Currently, we use a derivative of SDS for aqueous suspensions which is called sodium dodecylbenzenesulfonate (SDBS). It is thought that the additional benzene ring in the structure aids adhesion of the surfactant to the nanotube through $\pi$-$\pi$ stacking, producing more efficient dispersions.

## 3.2 Sonication

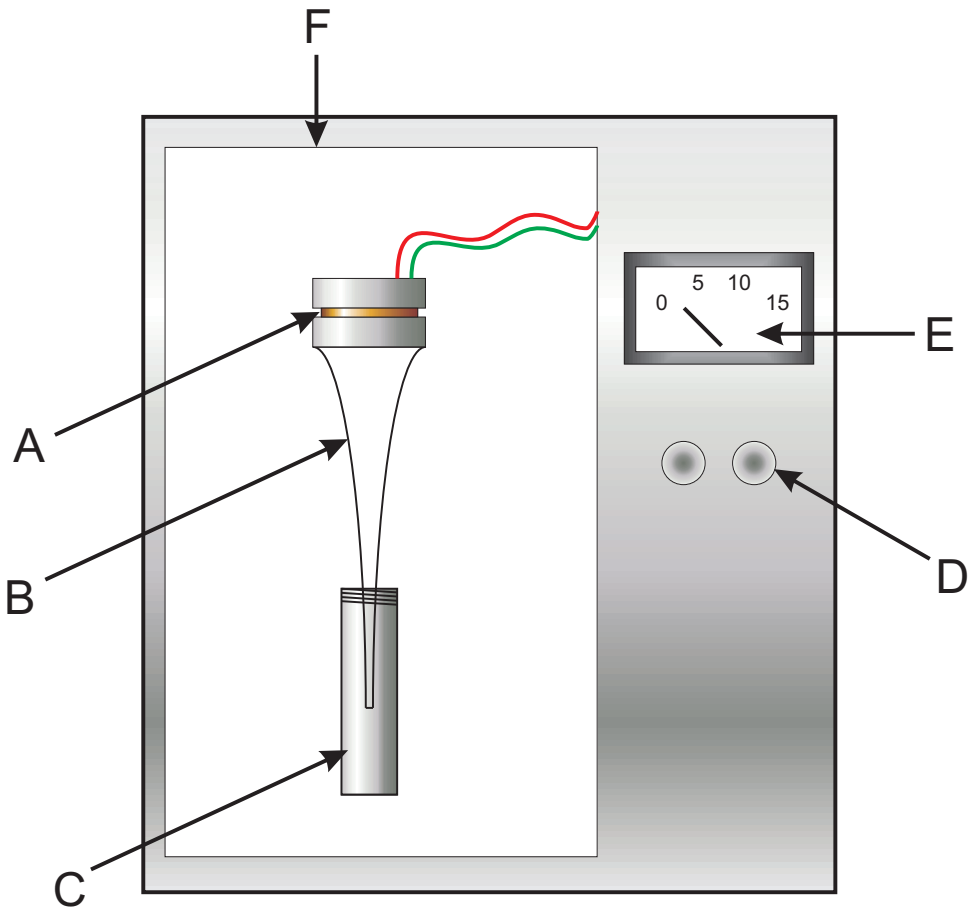


Figure 3.1: Schematic of the ultrasonic probe apparatus. The labeled components are as follows: **A**, the piezoelectric transducer, **B**, the exponential titanium sonication tip, **C**, SWNT dispersion (in a plastic sample holder), **D**, control switches for timer and power, **E**, scale for amplitude setting, **F**, sound proof enclosure.

The main role of the surfactant is to prevent the nanotubes from re-aggregating in the liquid. However, a crucial step in getting to this stage is to break the initial aggregates which exist in the raw material. For this we use powerful ultrasonic disintegrators designed for microbiological applications where they are used to rupture cells and bacteria for extraction of DNA. The principle of its operation relies on a titanium rod which is immersed in the suspension transmitting high frequency sound waves into the sample. As shown in figure 3.1, the titanium rod is connected to a 150 watt piezoelectric transducer. This rod is vibrated at 23kHz by the transducer. We use a rod which has an exponential curve to its diameter in order to minimise sample heating. Furthermore, samples are always sonicated in a beaker of ice water in order to dissipate the heat which is produced. Figure 3.2 shows the temperature change for small volumes of water over a 100sec sonication at different settings. The only variable parameters on the instrument are the amplitude & the duration of time which the sample is sonicated

for. The amplitude corresponds to the displacement of the tip which is caused by the transducer and is measured in micrometers. The formula for the intensity of a longitudinal wave in a fluid medium is

$$I = \frac{1}{2}\sqrt{\rho B}\omega^2 A^2 \tag{3.1}$$

where $\rho$ is the density of the medium, $B$ is its bulk modulus, $\omega$ is the frequency and $A$ is the amplitude. As can be seen from the form of the equation the power should increase with the amplitude squared. The fits to the data in figure 3.2 yield a temperature increase with amplitude to the power of 1.55. This is likely to be due to the inefficient insulation used to prevent heat loss, the inefficient transfer of energy from the rod to the medium and possibly a non-linearity between the scale on the instrument dial and the actual displacement at the tip of the rod. Nonetheless, the behavior shown helps to demonstrate the behavior of the sonication at a macroscopic scale. From the data we can also deduce the power which is transmitted into the sample. At an amplitude setting of 15 microns this was calculated to be 10.1 Watts ($\pm$0.4).

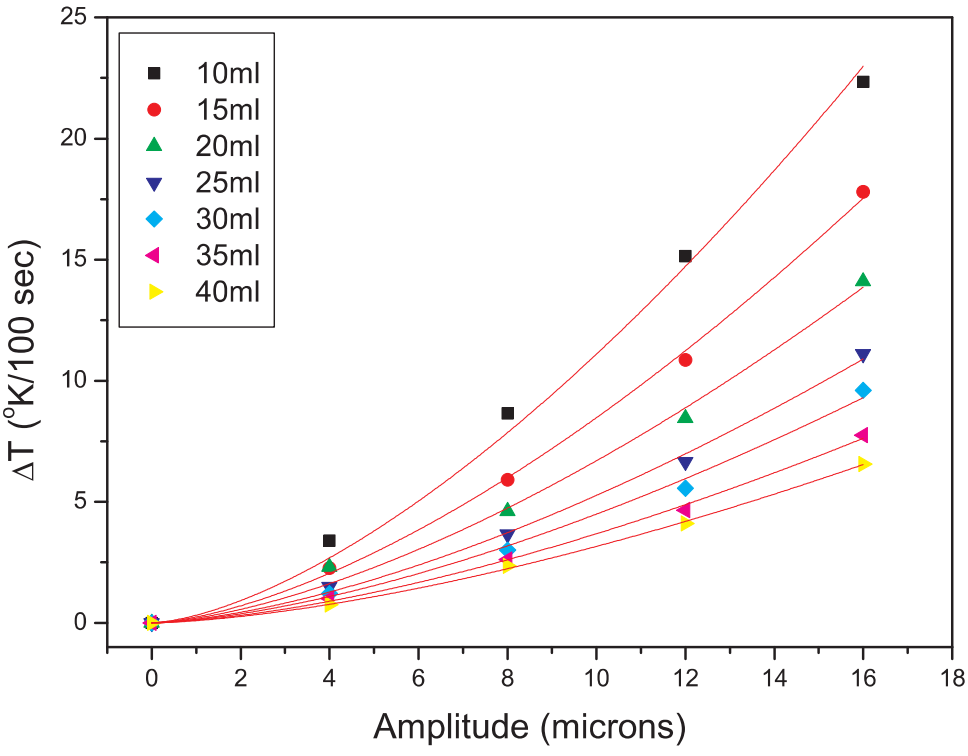


Figure 3.2: Experimental data and fits showing the temperature increase in samples of water subjected to the ultrasonicator.

For the dissociation of the nanotubes from the bundles it is important to have an understanding of the microscopic behavior. This has not been studied in any detail for the purposes of this thesis but some ideas will be presented for posterity. The action of high frequency acoustic waves on a fluid medium

is known to lead to an effect called cavitation. Cavitation is the rapid formation, growth and collapse of bubbles in a liquid which is often associated with propellers on ships but can also be induced by acoustic waves such as those produced by ultrasonic irradiation. The small pockets of gas in these bubbles can reach extremely high pressures and temperatures, sufficiently high that researchers have even tried using the effect to induce nuclear fusion reactions [4]. More commonly though cavitation is a nuisance as it causes damage to surfaces which it contacts.

It is presumed that the sonicator used in our sample preparation method induces cavitation in the nanotube dispersions. The micrometer sized bubbles create extremely high pressure gradients over short length scales, pulling the individual tubes from the bundles. The forces on the nanotubes may be so high that their bonds are broken and the nanotubes are shortened significantly by excessive sonication. In a study of the mechanism of cavitation-induced scission of SWNTs, Hennrich et al. [5] showed that after 40mins of sonication nanotubes of length 800 $\pm$ 300nm were cut to lengths of around 200nm. Interestingly they showed that the shortening follows a logarithmic decrease which is limited by the presence of a critical length for scission of around 100nm. Also given in the paper are the bubble growth and implosion dynamics which show that the maximum bubble radius has a value of 600$\mu$m and occurs with a frequency of around 80$\mu$s.

## 3.3 Centrifugation

After sonication the SWNT-surfactant dispersions are more homogeneous and the nanotubes take longer to precipitate. For the purposes of optical characterisation though it is necessary to enrich the proportion of individual tubes verses bundles. The main reason for this is that the bundles absorb and scatter light strongly, but don't have any distinguishable structure in the spectra which allows their contribution to be subtracted out. This makes them a parasitic impediment to investigating the underlying individualized SWNT properties. However, it is possible to remove the bundles due to the fact that they are of a higher density than the surfactant coated individual tubes. This is presumed to be due to the fact that the surfactant imparts some buoyancy on the nanotubes; for example, taking an individual SWNT from a value of 1.4 g/cm$^3$ to around 1 g/cm$^3$ [6]. The bundles, on the other hand, have less surface area for the dispersing agent to coat. Thus the additional buoyancy which

the surfactant imposes is of little benefit for keeping the bundles in suspension under high centrifugal forces. Such high centrifugal forces are readily available in other scientific disciplines, such as in biological research, where they are used for both analysis and preparative work. Ultra-centrifuges are capable of subjecting samples to accelerations of over 100,000 times that of gravity. Particles which are in a suspension with a solvent of a lower density can be sedimented rapidly and efficiently. The key component of the ultracentrifuge is the rotor which the samples are mounted on. This is precision engineered out of titanium or steel and must be mounted with great care to ensure perfect balance. The rotor used to prepare nanotube/surfactant suspensions for the studies in this thesis was of the swing bucket variety, whereby the sonicated sample dispersion ($\sim$30ml) is loaded into a vertical sample tube. As the rotor accelerates the bucket swings out to the horizontal position so that the sample is sedimented to the bottom of the tube. The standard procedure for the centrifugation required 85,000g for 4 hours [7]. After this the top 50% of the dispersions would be decanted for subsequent studies. This procedure had been optimized by a previous student in the group and further details can be found in his DPhil thesis [8].

# Bibliography


[1] A. Thess *et al.* Crystalline ropes of metallic carbon nanotubes. *Science*, 273:483, 1996.

[2] C.-H. Suna, L.-C. Yina, F. Lia and G.-Q. Lub. Van der Waals interactions between two parallel infinitely long single-walled nanotubes. *Chem. Phys. Lett.*, 403:343-346, 2005.

[3] S. Giordani, S. D. Bergin, V. Nicolosi, S. Lebedkin, M. M. Kappes, W. J. Blau and J. N. Coleman. Debundling of single-walled nanotubes by dilution: Observation of large populations of individual nanotubes in amide solvent dispersions. *J. Phys. Chem. B*, 110:15708-15718, 2006.

[4] R. P. Taleyarkhan, C. D. West, J. S. Cho, R. T. Lahey, R. I. Nigmatulin and R. C. Block. Evidence for Nuclear Emissions During Acoustic Cavitation. *Science*, 295:1868-1873, 2002

[5] F. Hennrich, R. Krupke, K. Arnold, J. A. Rojas-Stutz, S. Lebedkin, T. Koch, T. Schimmel and M. M. Kappes. The Mechanism of Cavitation-Induced Scission of Single-Walled Carbon Nanotubes. *J. Phys. Chem. B*, 111:1932–1937, 2007.

[6] M. S. Arnold, A. A. Green, J. F. Hulvat, S. I. Strupp and M. C. Hersam. Sorting carbon nanotubes by electronic structure using density differentiation. *Nature Nanotech* 1:60–65, 2006.

[7] M. J. O'Connell *et al.* Band gap fluorescence from individual single-walled carbon nanotubes. *Science*, 297:593–596, 2002.

[8] L.-J. Li. Probing the Band Gap Structure of Single-Walled Carbon Nanotubes by Optical Spectroscopy. *DPhil thesis, Oxford*, 2006.

# Chapter 4

# PLE Mapping

## 4.1 Foreword

Experimental characterisation of single-walled carbon nanotubes has been an enduring challenge since their discovery in the early 1990s. Researchers have been motivated primarily by two goals:

- Investigation of the intrinsic properties of carbon nanotube structures.
- Determination of the abundance and distribution of the various species present in a given sample.

Improvement in the optical spectroscopy of SWNTs has gradually met this challenge, advancing both our knowledge of the physical behavior of carbon nanotubes and our ability to detect the presence of distinct species even at remarkably low concentrations. Other commonly used characterisation methods, such as TEM and AFM, suffer from their ineffectiveness at discriminating between the different nanotube structures (particularly those with the same diameters) and from the inherent difficulty in obtaining quantitative results using these techniques. Optical spectroscopy, and in particular photoluminescence excitation (PLE) mapping, has been used throughout the studies presented in this thesis, where investigation into the fractional concentrations of the various SWNT species and their electronic interactions with surrounding media have been the primary interests. Since this technique is concerned with light emission from materials, a short review of the different physical processes by which this may occur will be discussed here first.

## 4.2 Light Emission

Light emission from materials comes in many forms and may be referred to by different names by researchers from different backgrounds. Firstly, it is necessary to distinguish the light emission we are concerned with here, luminescence, from emission due to thermal radiation. Visible light may be obtained from hot incandescent bodies, such as metal filament light bulbs which operate at over 2000° Kelvin, whereas emission due to luminescence may occur at any temperature [1]. Secondly, luminescence should last for a time exceeding the period of an electromagnetic oscillation [2]. This distinguishes luminescence from reflected light and also from scattered light. This point is particularly pertinent in luminescence where the excitation source is electromagnetic radiation. Intermediate processes between photon absorption and emission take place which exceed the period of an electromagnetic oscillation. This time delay eliminates any correlation between the phases of the exciting and emitted light, unlike in the cases of reflected or scattered light.

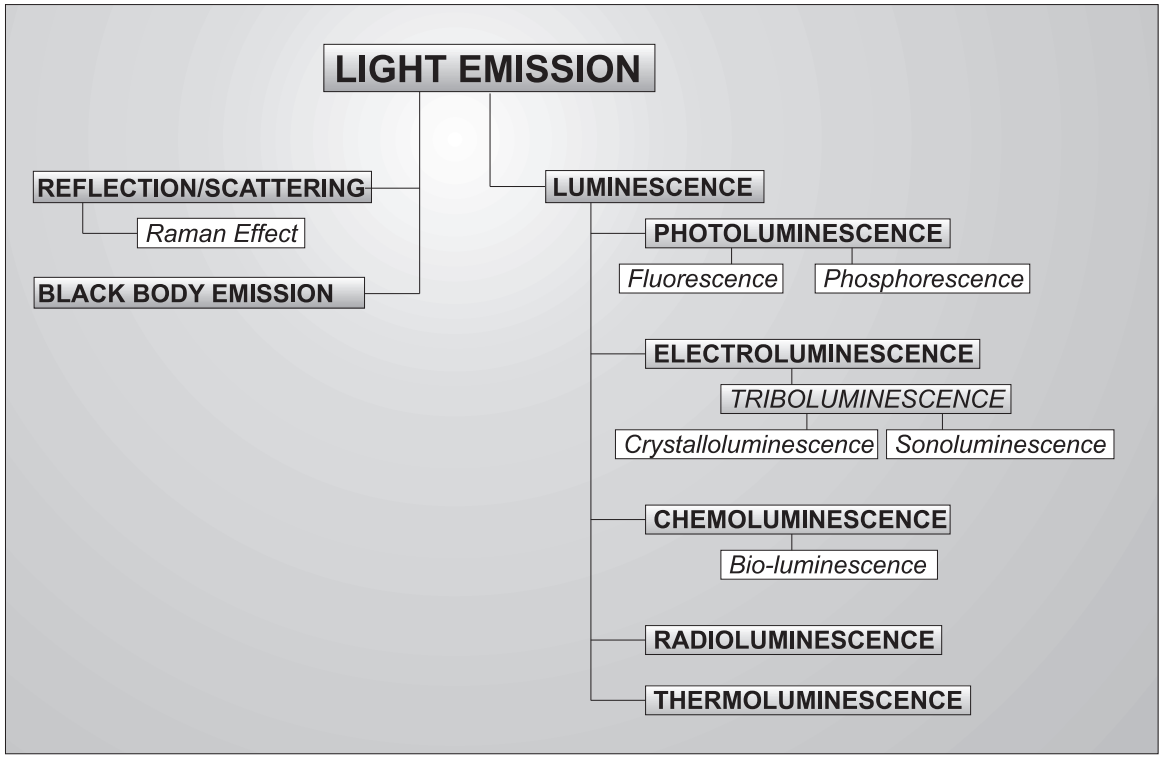


Figure 4.1: Schematic breakdown of various light emission phenomena.

There are many different types of luminescence, however, clear distinctions can be made by considering the source of the excitation. The commonest form in the field of carbon nanotube research [3], and the process which is used as an experimental technique here, is called photoluminescence. It occurs

when luminescence is stimulated by the absorption of a photon, typically of energies corresponding to the UV-Vis-NIR region of the spectrum. Energy from the excited electron-hole pair is then lost through molecular vibrations before the final transition to the ground state is made by emission of another, lower energy, photon. Thus, in most examples, the wavelength of the emitted light will be longer than that of the excitation source. As previously mentioned there is always a delay between the photon absorption and emission due to relaxation of the excited particles. This is known as the photoluminescence lifetime. A process with a short lifetime is called fluorescence and one with a long lifetime is called phosphorescence. Typical time scales between absorption and emission for these processes would be from $10^{-12}$ to $10^{-7}$ seconds in the case of fluorescence whereas phosphorescence may last for hours or even days [2]. Both of these effects may be found in everyday applications from glow-in-the-dark stickers to road signs to washing powders claiming to give whiter than white results.

Although electroluminescence has also been shown to occur in SWNT samples [4, 5], it and the other luminescence processes shown in figure 4.1 were not the focus of the studies done for this thesis. As already mentioned, photoluminescence (PL) is the process at the centre of one of the major investigative techniques in the field of SWNT characterisation. With lifetimes on the order of $10^{-8}$ seconds in SWNTs the process is undoubtedly fluorescence [6]. However, this distinction is not regularly made in the literature and so photoluminescence may be regarded as synonymous with fluorescence here too.

## 4.3 Optical Absorption

Before looking at emission spectra from SWNTs it is important to appreciate another aspect of the PL process, light absorption. Optical absorbance spectroscopy is itself an important characterisation technique for carbon nanotubes. Also, since photon absorption is the primary step in PL, it can yield valuable information which can help in interpreting the spectra. Absorbance spectroscopy is not affected by chirality dependent PL efficiencies and so is, in principle, the most accurate method for determining the relative concentrations of SWNT species. In practice, however, non-resonant absorption, a broad linewidth and overlapping transition energies diminish the resolution of these spectra making it impossible to identify the contributions of individual nanotube species.

Figure 4.2 shows an old absorbance spectrum of SWNTs crudely dispersed in the aqueous surfactant sodium dodecylsulfate. The graphitic $\pi$-plasmon is very dominant in the spectra. The precise origin of this broad-band absorbance still remains uncertain. It is likely that it comes from the oscillation of free electrons either in graphitic impurities or metallic SWNTs [3]. The contributions made by each of these mechanisms is unclear and so they are merely presented for figurative purposes in figure 4.2. The $\pi$-plasmon's low energy tail extends into the infra-red and results in a background on which the $E_{ii}$ (where $i$ = 1,2,3...) transitions sit. In the figure these transitions are labeled as $S_{11}$, $S_{22}$ and $M_{11}$ to distinguish between the transitions from Semiconducting and Metallic tube types. Whilst these early spectroscopic attempts showed some of the fundamental features of SWNT spectra they lacked the resolution to allow investigation of the individual $(n, m)$ species.

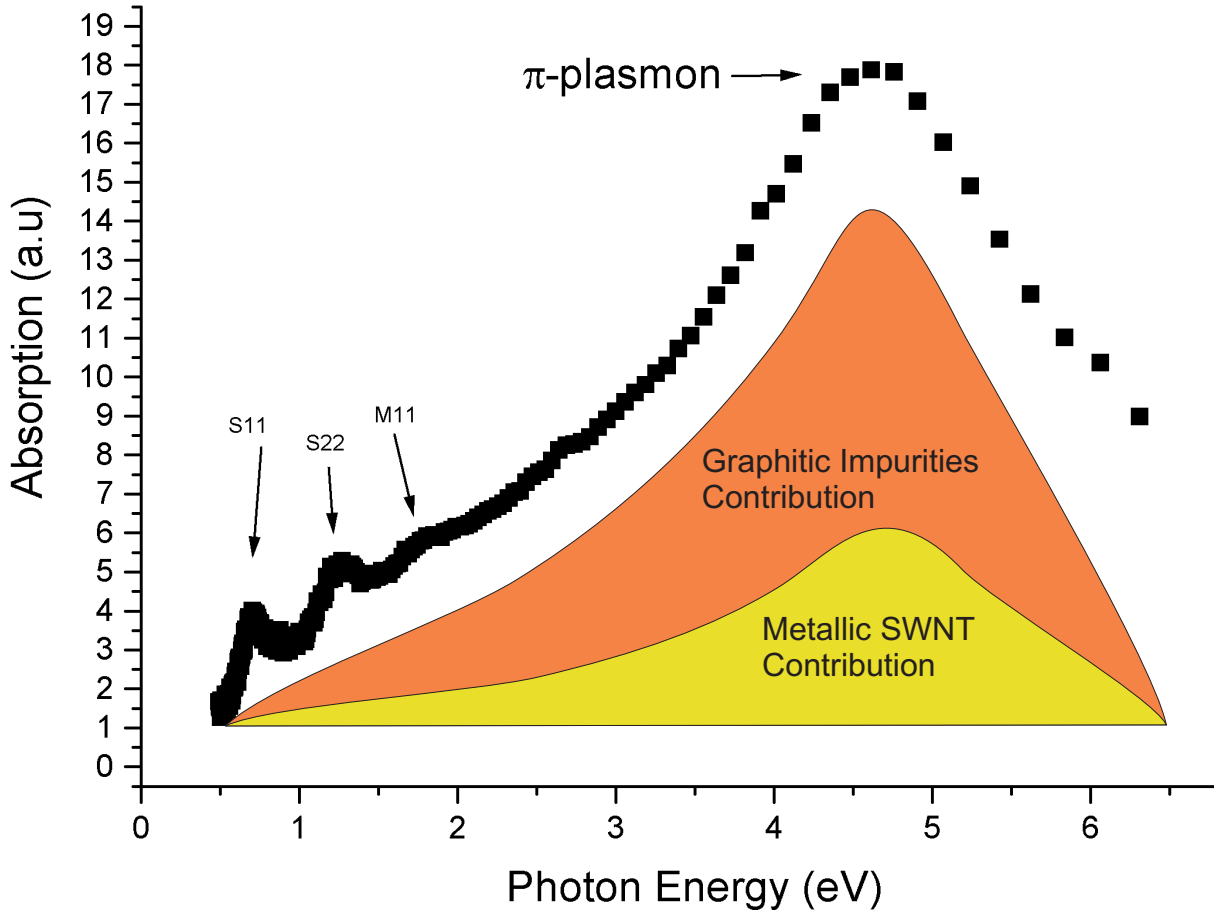


Figure 4.2: A UV-Vis-IR spectrum taken by the author in 2003 showing some fundamental features of SWNT absorbance. The nanotube band-to-band transitions sit on top of a large background which is thought to come from graphitic impurities and metallic species.

It was soon realized that the poor resolution plaguing SWNT optical spectroscopy wasn't an inherent feature of bulk samples but merely due to poor preparation. Specifically, it was due to the presence of residual carbonaceous impurities and the aggregation of the individual SWNTs into bundles. When SWNTs are in contact with other species of different electronic structure, local electric fields cause a perturbation of their energy levels -having the effect of broadening the nanotube's absorption peak. This, combined with the natural proximity of $E_{11}$ (or $E_{22}$) energies in the distinct SWNT species causes the individual transitions to become smeared into one large peak. The use of aqueous surfactants [7] to solubilise the hydrophobic nanotubes in water helped to improve the stability of their suspensions.

However, this brought a further complication which hampered early attempts at measuring these transitions accurately in that $H_2O$, the solvent, shows a strong absorption in the infra-red. Fortunately a simple fix to this was found by replacing the $H_2O$ used with $D_2O$. This had no negative effect on the quality of the dispersion but pushed the solvent absorption edge from 1.4$\mu$m to 1.8$\mu$m, allowing access to SWNT features in this range. Use of high purity $D_2O$ and care to avoid $H_2O$ contamination is crucial to effective optical spectroscopy of SWNTs using surfactants.

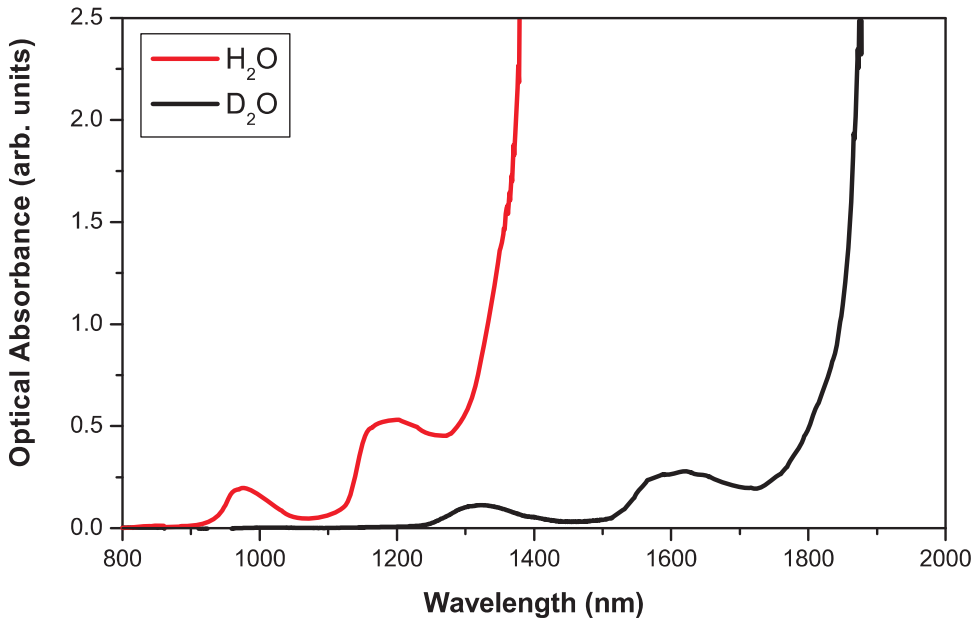


Figure 4.3: Absorbance of $D_2O$ and $H_2O$ in the infra-red range.

A further breakthrough in sample preparation [8] was the use of ultracentrifugation as a method for removing non-dispersed material and, in particular, for removing bundles of SWNTs. This method relies on the fact that, when coated with a surfactant, the individual SWNTs should be neutrally buoyant whereas the denser bundles should be sedimented by the centrifugal force. The ability to remove

bundles of SWNTs from the dispersions was a significant breakthrough. Even when bundles contain the same species of SWNT with identical initial energy gaps there will be differences in the local environments (there are many possible combinations of nearest neighbour species) causing inhomogeneous broadening of the energy transitions. Isolated individual SWNTs have a much more uniform environment and therefore narrower linewidths. Furthermore, the isolating of semiconducting species from metallic was the crucial step necessary for photoluminescence. Indeed, these advanced sample preparation techniques led to a major improvement in the resolution of optical absorbance spectra making it possible to resolve families of individual species and to the first reports of photoluminescence from single-walled carbon nanotubes [8, 9, 10].

## 4.4 Photoluminescence from SWNTs

Photoluminescence (PL) from molecules and bulk semiconductors has been well documented. In it's most simple approximation, PL occurs when an electron is photo-excited to a higher energy level and then returns to the ground state by re-emitting a photon of lower energy. The emitted photon must come from the minimum energy gap between lowest unoccupied molecular orbital (LUMO) and highest occupied molecular orbital (HOMO) levels. In semiconductor physics these are called the conduction band edge and valence band edge. PL spectroscopy is therefore an excellent method for measuring the bandgap of semiconducting materials. However it is fundamentally insensitive to metallic materials, a drawback in carbon nanotube characterisation since one third of the species of SWNTs in an ensemble sample are metallic.

A more sophisticated view of the photoluminescence process, and one which is particularly necessary for carbon nanotubes, must include the existence of electron-hole pairs known as excitons. The presence of excitons in carbon nanotubes was first investigated theoretically by Ando in 1997 [11] and then later confirmed through experiments by Wang et al. [12] and Maultzsch et al. [13] in 2005. Figure 4.4 shows a schematic for a photoluminescence process in SWNTs. Step 1 is referred to as excitation and consists of the creation of an electron-hole pair. Step 2, the electron and hole then relax to their respective minimum energy states. Step 3, recombination of the electron-hole pair occurs through the emission of a photon. The defining characteristic of excitons is that the electron and hole

pair is subject to a Coulomb attraction called the binding energy. This electrostatic interaction is screened by the dielectric constant and so a typical binding energy may be very small, as in inorganic semiconductors such as silicon, or it can be orders of magnitude larger, as in organic polymers and SWNTs. As mentioned in chapter 2, a significant result of this difference is that for conventional semiconductors excitonic effects only become dominant at low temperatures as the binding energy becomes comparable to kT. However, for carbon nanotubes the large value of the binding energy means the excitons are not thermally dissociated and thus remain an important feature of nanotube spectroscopy even at room temperature. For example, in chapter 5 it is shown that changes in the local environment cause shifts in the energy transitions due to screening of the binding energy. Furthermore, in chapter 7 it is demonstrated that the interplay of the Dark and Bright excitons cause enhancement of the PL intensity in high magnetic fields (albeit this experiment is done at 2K).

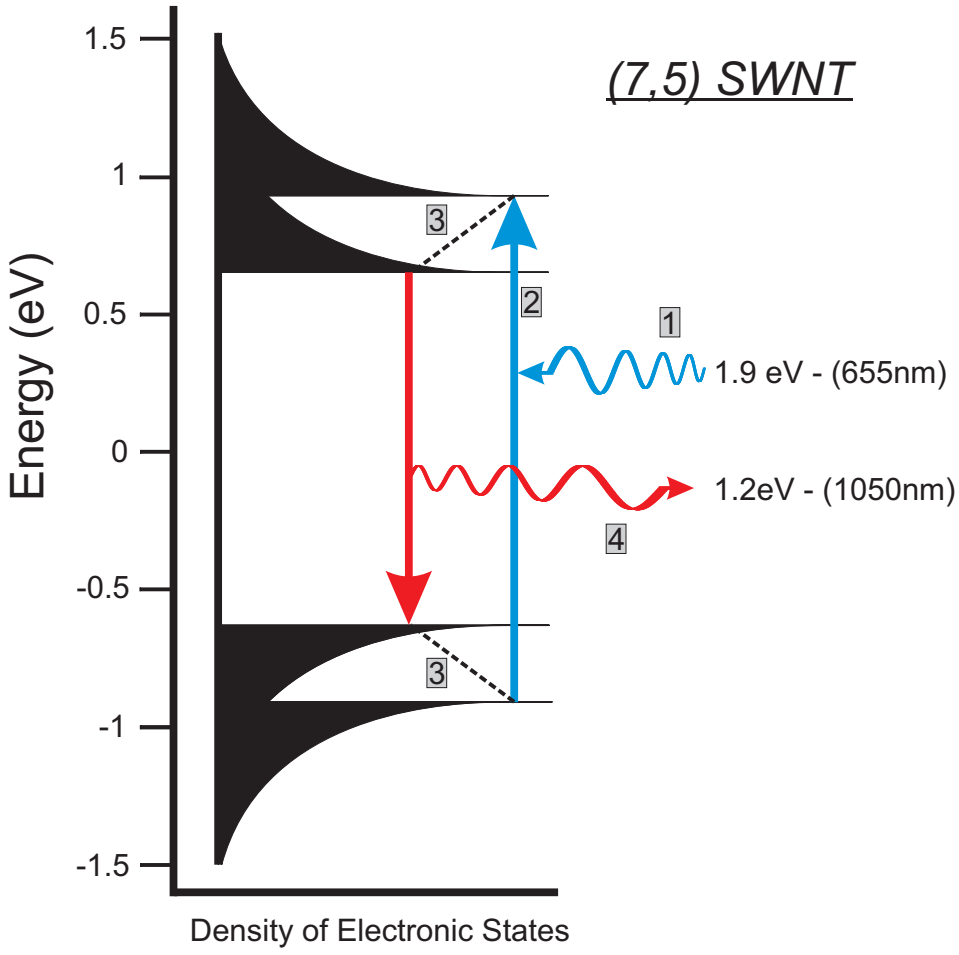


Figure 4.4: A schematic diagram of the photo-luminescence process in SWNTs. The energy levels correspond to the prominent van Hove singularities in a (7,5) nanotube. In step 1, a photon, with an energy of 1.9eV, is incident on the SWNT. This causes the excitation of an electron into the conduction band (step 2) followed by its relaxation to the lowest available energy level (step 3). Simultaneously, the hole relaxes to the edge of the valence band (step 3). Recombination of the carriers then occurs by way of emission of a photon at a lower energy of 1.2eV (step 4).

Figure 4.5 shows PL spectra of SWNTs produced by HiPCO and CoMoCAT growth processes taken using a Helium Neon laser emitting at 633nm as the excitation source. The peaks have been deconvoluted using commercially available software. Fits using a combination of Gaussian and Lorentzian lineshapes, known as a Voigt profile, have been used in this example indicating that both homogeneous and inhomogeneous broadening mechanisms are taking place. The FWHM of these spectra is approximately 30meV. This linewidth is larger than expected and would indicate that there is substantial system broadening by the experimental apparatus. Nonetheless this figure illustrates the type of spectra that can be obtained routinely using a simple set-up and single wavelength excitation. Homogeneous broadening is intrinsic to the SWNT transitions and is not affected by temperature. Inhomogeneous broadening may arise through the presence of defects or other differences in the local environment of the SWNTs, such as differences in the surfactant coverage or hydration state. Broadening of the linewidth by the optical system was common in the early measured PL data due to the slit width on the spectrometer being increased to strengthen the signal throughput. However, advances in the optimization of sample preparation and the use of state of the art equipment has significantly improved the measured PL intensities in recent years. Somewhat related to this is the

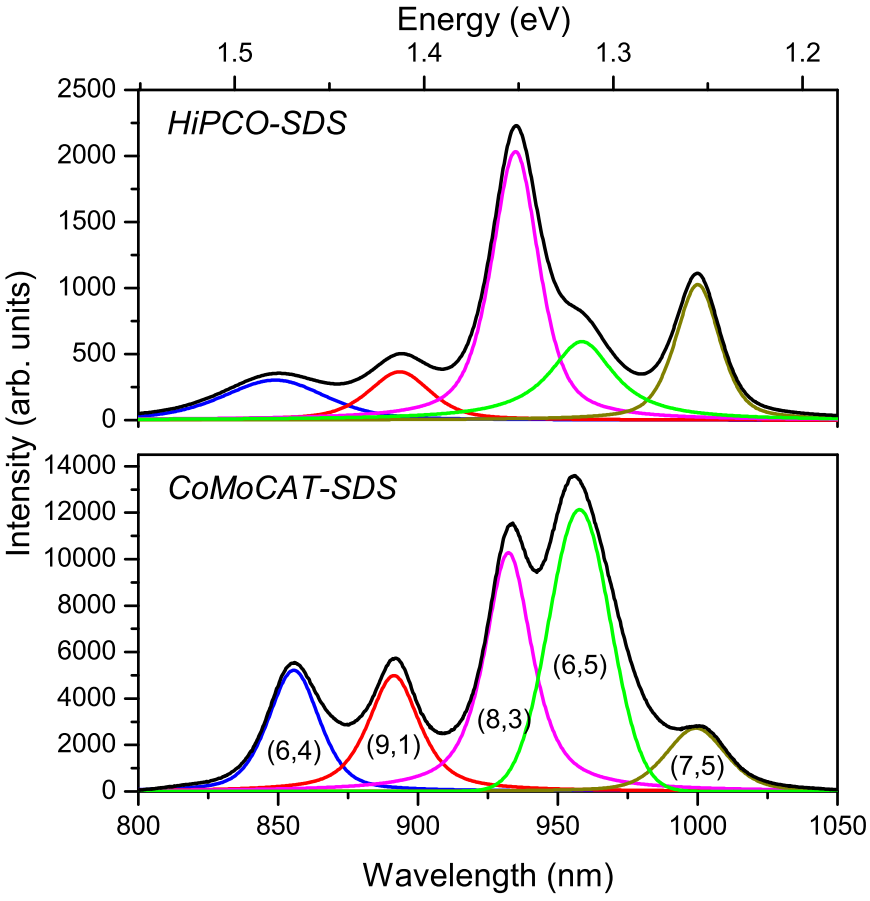


Figure 4.5: PL Spectra of narrow diameter nanotubes grown by two different growth methods.

issue of the photoluminescence quantum yield. The intrinsic yield is still a subject of debate in the SWNT spectroscopy community [3]. Early estimates put its value at between 0.01 and 0.1% [8]. This is the sample quantum yield though; the presence of the non-radiative absorbing impurities such as the $\pi$-plasmon reduces the observed luminescence. Measurements done in our lab using samples prepared by advanced purification techniques have raised this value significantly to around 1.5%. It is likely though that the intrinsic value for a single species in the absence of parasitic absorbance will be higher still and reports of 7% have emerged recently [14].

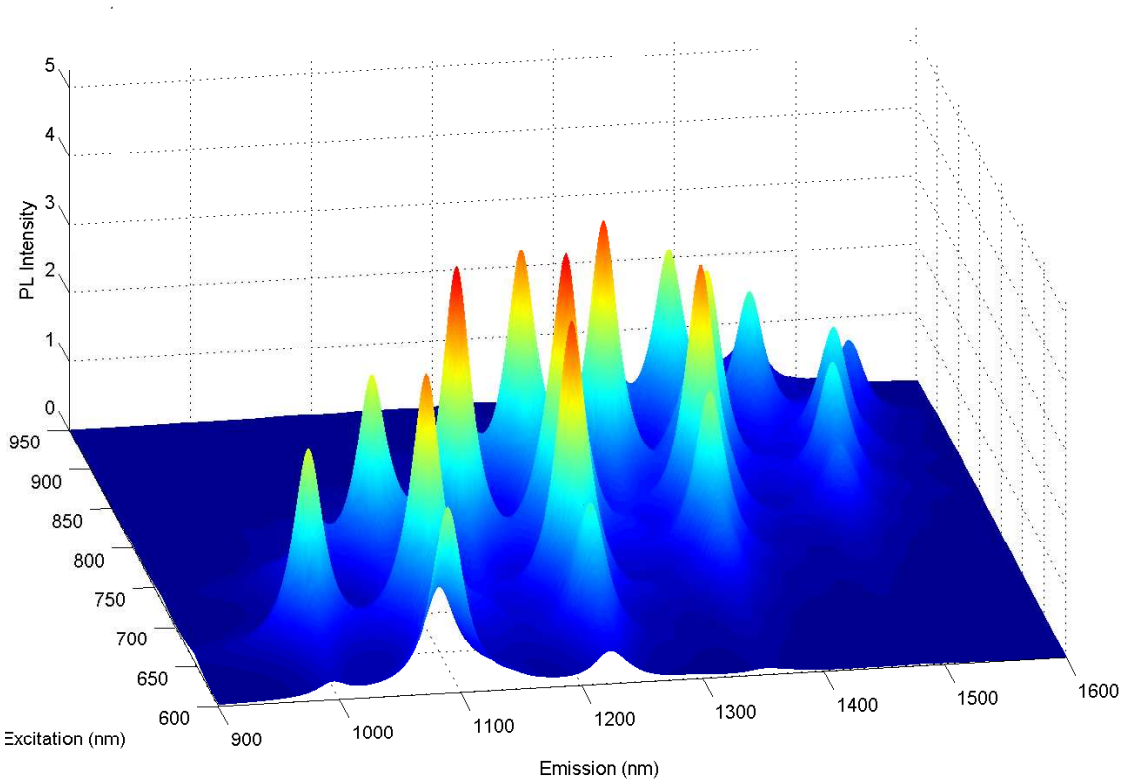


Figure 4.6: A 3D representation of a photoluminescence-excitation map

The PL spectra have been compared with absorbance spectra of the same samples and show little or no difference in peak position. This is unlike other molecular systems, such as organic polymers, which exhibit a Stokes shift between the absorbance and fluorescence peaks caused by the relaxation of the lattice [1]. PL spectroscopy has the advantage over absorbance spectroscopy as a characterisation tool due to the fact that is is a resonant process. However, it can still be confusing to interpret single-line spectra when there is a close overlap of several emission energies from different SWNTs. The ability to distinguish the SWNTs reliably is possible by using a tunable excitation source to match the excitation wavelength to the $E_{22}$ transition energy. This resonantly enhances the $E_{11}$

emission peak for a particular species and when scanned over the full range creates what is called a photoluminescence-excitation map. Such a plot is shown in figure 4.6 with the emission shown on the X-axis and the wavelength of excitation shown on the Y-axis. Each peak comes from a distinct species of nanotube with its intensity being indicative of its concentration in the sample. When viewed from above a distinct pattern emerges, figure 4.7. As was seen in the theory section, tight binding models can be used to find the $E_{11}$ and $E_{22}$ energy gaps of the various SWNTs. By matching the patterns of these plots with experimental spectra we can revise the theory to create semi-empirical models of these energies for various $(n, m)$ indexed SWNT species [15]. These semi-empirical models form the basis for all subsequent identification of nanotube species present in a sample characterised by PLE mapping.

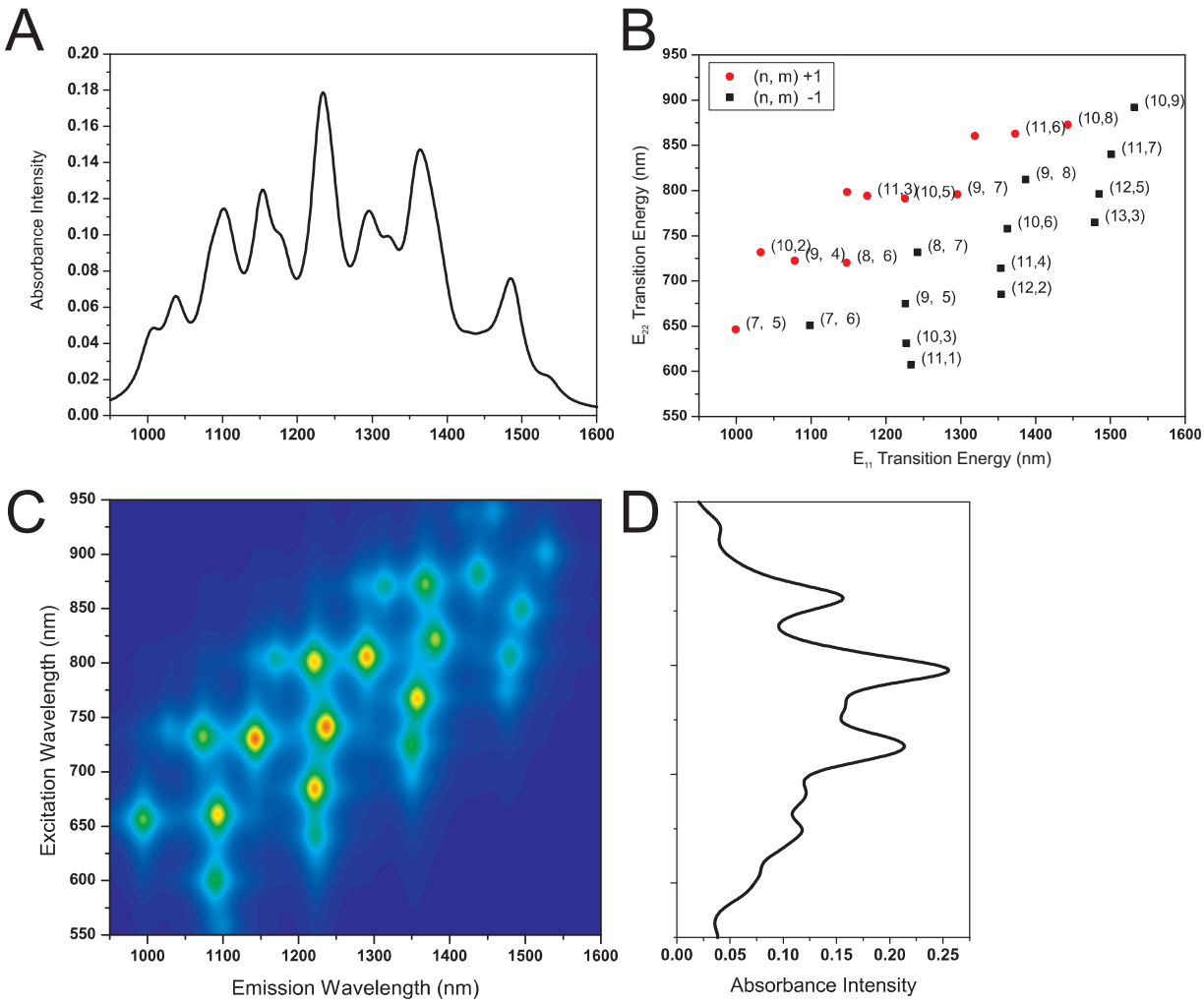


Figure 4.7: Panels A & D show simulated absorbance spectra which which cover the $E_{11}$ and $E_{22}$ regions respectively and are derived from the simulated PLE map in panel C. The plot in panel B of the figure shows theoretical positions for the energy resonances.

## 4.5 Experimental Method

In all absorbance experiments performed for SWNT characterisation, a commercially available Perkin Elmer photo-spectrometer was used. For the photoluminescence experiments it was necessary to use a home-built system. Initial work done in the group used lasers with single lines of excitation such as an argon ion laser at 488nm and 515nm, a HeNe laser at 633nm and an 810nm diode laser. Whilst these provided high intensity irradiance they could only excite a limited number of tube species. The availability of a tunable Ti:Sapphire laser made the first PLE mapping possible in our group. This has a range of 700 to 990nm, sufficient to examine a significant number of nanotube species. Although this laser outputs high intensity light (making collection times reasonably short) it cannot easily be automated. This meant it could take several hours of laborious work for a single PLE map. Testing many different samples or different parameters using PLE mapping thus became possible but extremely tedious.

In order to speed up the process of PLE mapping a fully automated system was set up. A 75W xenon lamp focused into a monochromator set to a standard bandpass of 5nm was used to excite a quartz sample cell. Collection of the emitted light was made at a right angle to the excitation. For measurement of the luminescence from the sample either of two detectors could be used. A highly sensitive thermo-electrically cooled Silicon CCD with a range of 400-1000nm or a liquid nitrogen cooled Indium Gallium Arsenide (InGaAs) photodiode array with a range of 900-1600nm. Some previous work had been done using a Germanium photodiode detector which required the collected light to be scanned over the detector in order to record the PL intensity as a function of wavelength. This latter type of system would have made recording each PLE map an extremely lengthy process. However, the availability of diode array detectors makes much faster collection times possible, with the result that an entire PLE map can be recorded in a matter of minutes rather than hours.

The source lamp and monochromator do not give a constant irradiance of the sample over the spectral range. This makes it necessary to normalise each spectra after it is recorded. This was done by deflecting a small fraction of the excite beam onto a silicon photodiode connected via a voltmeter to the computer. Measuring the light intensity in this way produces a normalisation in terms of the photon flux as opposed to power. The entire system is controlled by a custom designed LabView

program. This program lets the user set the excitation range and step size on the monochromator and the collection time for the detector as well as correcting each spectra with the normalisation factor. The output from the program is a matrix which can easily be plotted using a software package such as Origin or Matlab.

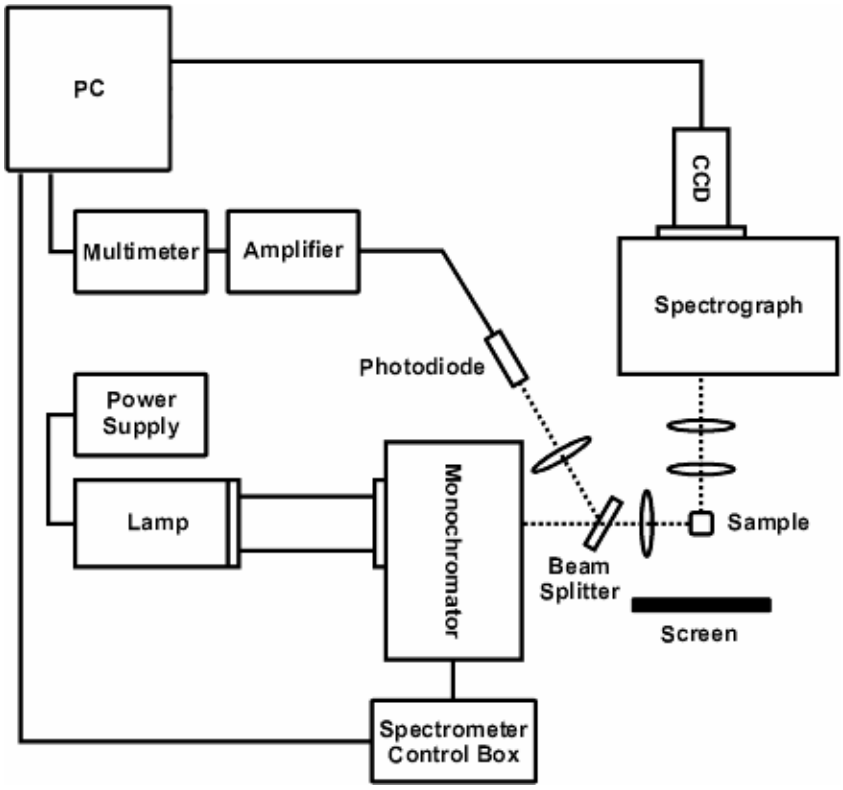


Figure 4.8: PLE mapping system schematic

Although this system is largely fit for purpose it does have some limitations. Larger diameter SWNT species have minimum energy gaps which are smaller than the bandgap of the InGaAs material used in this detector, therefore their luminescence cannot be studied. Overcoming this issue requires the use of an 'extended' 2.2$\mu$m InGaAs system. These detectors have a higher dark count than the standard InGaAs and it is difficult to observe the weak PL from SWNTs. A further problem is that the xenon lamp used for excitation has sharp peaks in it's near infra-red emission. These peaks cannot be totally compensated for by the normalisation employed here, making it difficult to interpret spectra in this range. This issue may be overcome by using a tungsten-halogen bulb as a broadband source which produces a much more even spectrum. However, the most crucial limitation in probing the luminescence from larger diameter SWNTs is the optical absorption from solvent. As was seen in figure 4.8, the absorbance of $D_2O$ has a strong edge at a wavelength of 1.8$\mu$m. This restricts the possibility of recording PL in aqueous surfactant dispersions to SWNTs of diameter less than $\sim$1.5nm.

## 4.6 PLE Maps of SWNTs from Various Sources

One powerful aspect of SWNT characterisation using PLE mapping is its ability to produce a 'finger-print' spectra of a sample. This comes from the distribution of peak intensities that results from the unique composition of $(n, m)$ species' concentration in samples from a particular growth process. As part of these studies, SWNTs from three distinct sources have been used:

**1.** Commercially available material grown using the 'HiPCO' [16] and 'CoMoCAT' [17] processes.
**2.** Samples from the group of Dr. Siegmar Roth at the Max-Planck-Institut für Festkörperforschung in Stuttgart grown by 'arc discharge' and 'laser vaporisation' processes.
**3.** Material from a collaboration with a company in Belgium called 'Nanocyl', a producer of SWNTs and related structures. The following sections show PLE maps and give brief descriptions of the characteristics of nanotubes from these different sources.

### 4.6.1 Common Commercial Materials

Figure 4.9 shows typical PLE maps obtained using the system described previously for 'HiPCO' and 'CoMoCAT' materials in aqueous surfactant dispersions. The colour scale is used to illustrate photoluminescence intensity with the bar shown on the right of each map as a guide. For the HiPCO sample it can be seen that there is a wide range of different nanotube species present. The diameters of these species ranges from around 0.8nm to 1.25nm. Due to the quality control inherent in this commercial source (less than 10% impurities by weight) we get relatively strong PL signals. A typical collection time for a sample of HiPCO dispersed in aqueous surfactant would be 20 seconds per excitation line, yielding an excellent signal to noise ratio. The total time for recording an entire PLE map, such as those shown, would therefore be around 30 minutes.

The CoMoCAT sample has fewer tube species and its diameter distribution is centred on a narrower diameter. Typically, SWNTs of between 0.75nm and 1nm are found in CoMoCAT material. A further difference is that the PL intensity is higher from these samples. There are several possible reasons for this: a lower concentration of impurities, fewer defects on the tube walls or different lengths of SWNT

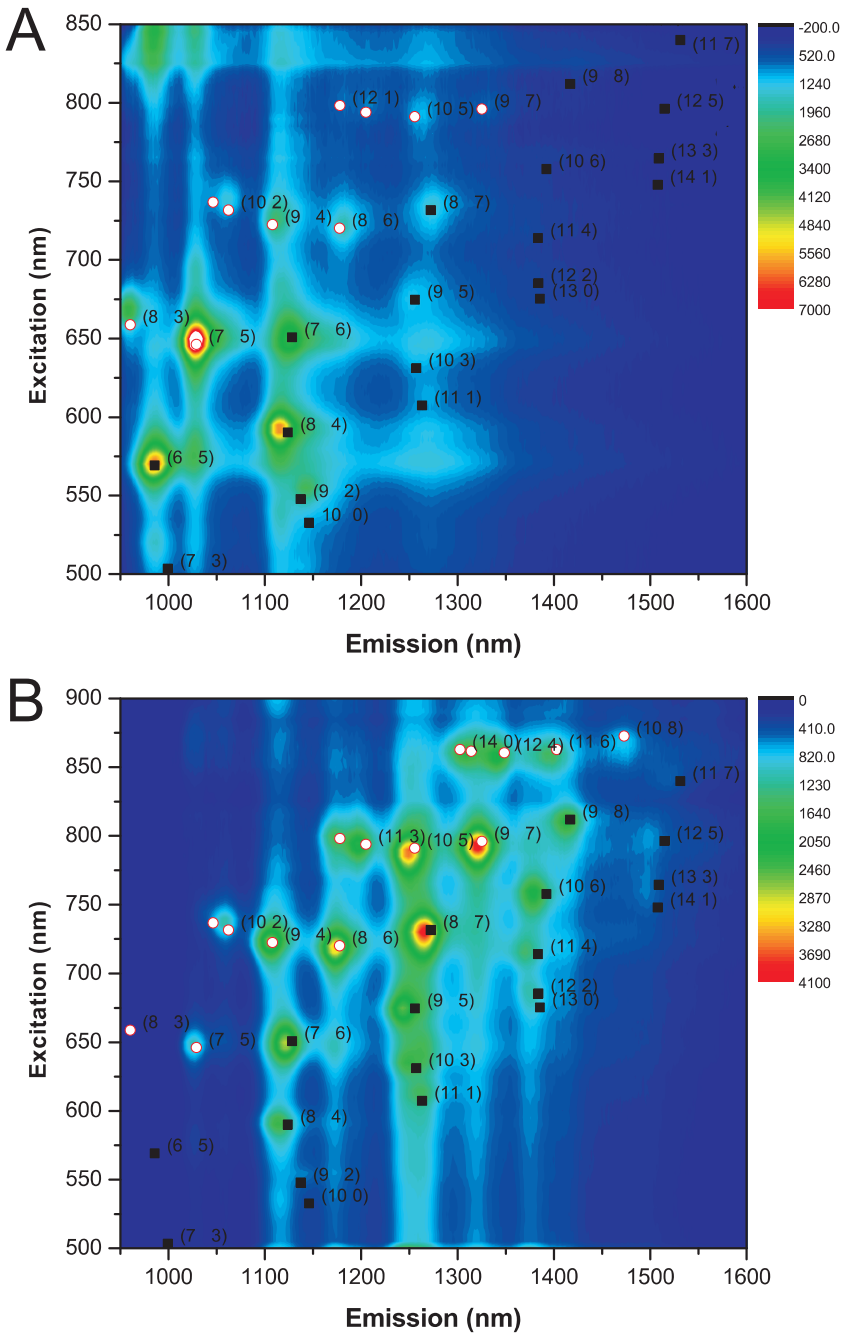


Figure 4.9: PLE Maps of commercially available SWNTs. Panel A is from material grown by the CoMoCAT process and panel B is material from the HiPCO process. The open red circles indicate positions of SWNTs with $q = +1$ and black squares indicate SWNTs with $q = -1$

are all possible causes. However, it is most likely that the reason should simply come from the narrow distribution of species present in this material. For example, in 10mg of CoMoCAT there will be a higher weight of a particular species than would be found in 10mg of HiPCO. This naturally would lead to a higher fractional concentration of each species and thus a higher PL intensity.

### 4.6.2 Samples from MPI Stuttgart

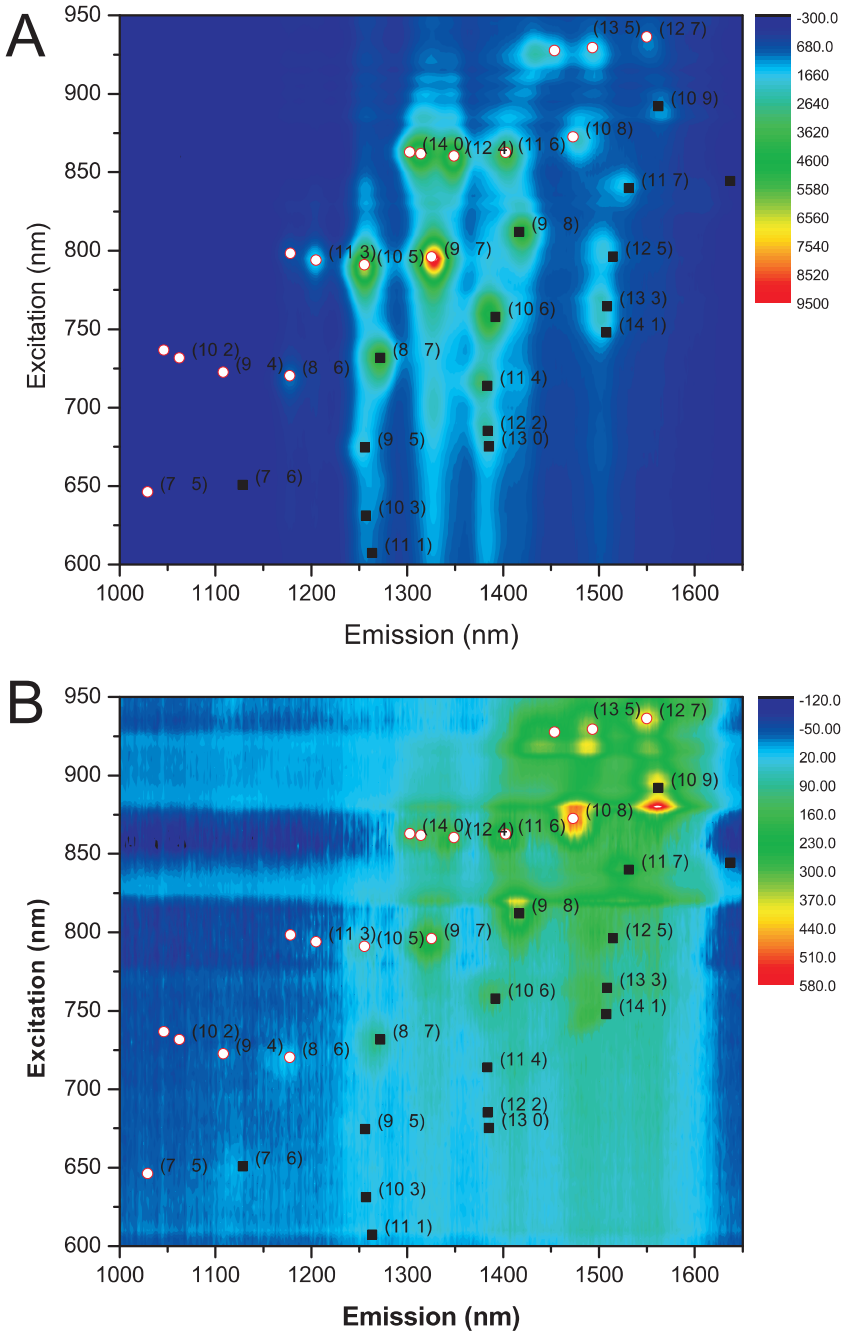


Figure 4.10: PLE Maps of SWNTs grown by the Laser Vaporization (A) and Arc Discharge processes (B)

Figure 4.10 shows PLE maps of SWNTs produced using the Laser Vaporization and Arc Discharge processes. This material is grown by the group of Dr. Siegmar Roth at the Max Planck Institute in Stuttgart. Part of their research concerns the effect which the catalyst metal has on the diameter distribution. Interestingly they are one of the few groups to use the non-magnetic metals Rhodium and Platinum to produce high quality SWNTs in both the laser and arc processes. The map for the laser vaporization SWNTs shown here was made using material grown with Rh/Pt catalyst. It produces SWNTs of slightly narrower average size than material grown using nickel based catalyst mixtures. Nonetheless, all SWNT samples grown by laser vap. have a small distribution of species and generally produce tubes with diameters around 1.1nm to 1.3nm. Some samples give strong PL intensities, factors of five or six higher than HiPCO SWNTs. Again this is thought to be due to the narrow range of species and the purity of the starting material.

The SWNTs produced by the arc discharge process on the other hand are of lower purity and have a larger distribution of species with diameters in the range 1.1nm to 1.6nm. Recording spectra from these samples is difficult due to the system limitations mentioned previously and the lower concentrations of observable species. Thus a poor signal to noise ratio gives a grainy PLE map such as that shown in figure 4.10, typical of dispersions prepared with this material.

One useful result from the analysis of PLE maps of samples from Stuttgart came from its ability to quantitatively measure differences in diameter distribution. Samples were grown using the laser vaporization technique for various gas pressures. Previously this parameter had been varied in order to maximise the yield of SWNTs produced. However, using PLE mapping it was possible to show that the gas pressure also has an effect on the diameter distribution of the SWNT ensemble. Lowering the gas pressure in the reaction chamber broadens the distribution of tube species, as can be seen in figure 4.11. The two plots show sections cut from PLE maps of samples grown with different chamber pressures. Both show increases in the longer wavelength peaks attributed to larger diameter SWNTs. The 790nm excited spectra also show an increase in the peak at around 1250nm, indicating a broadening of the distribution as opposed to a shift in average diameter.

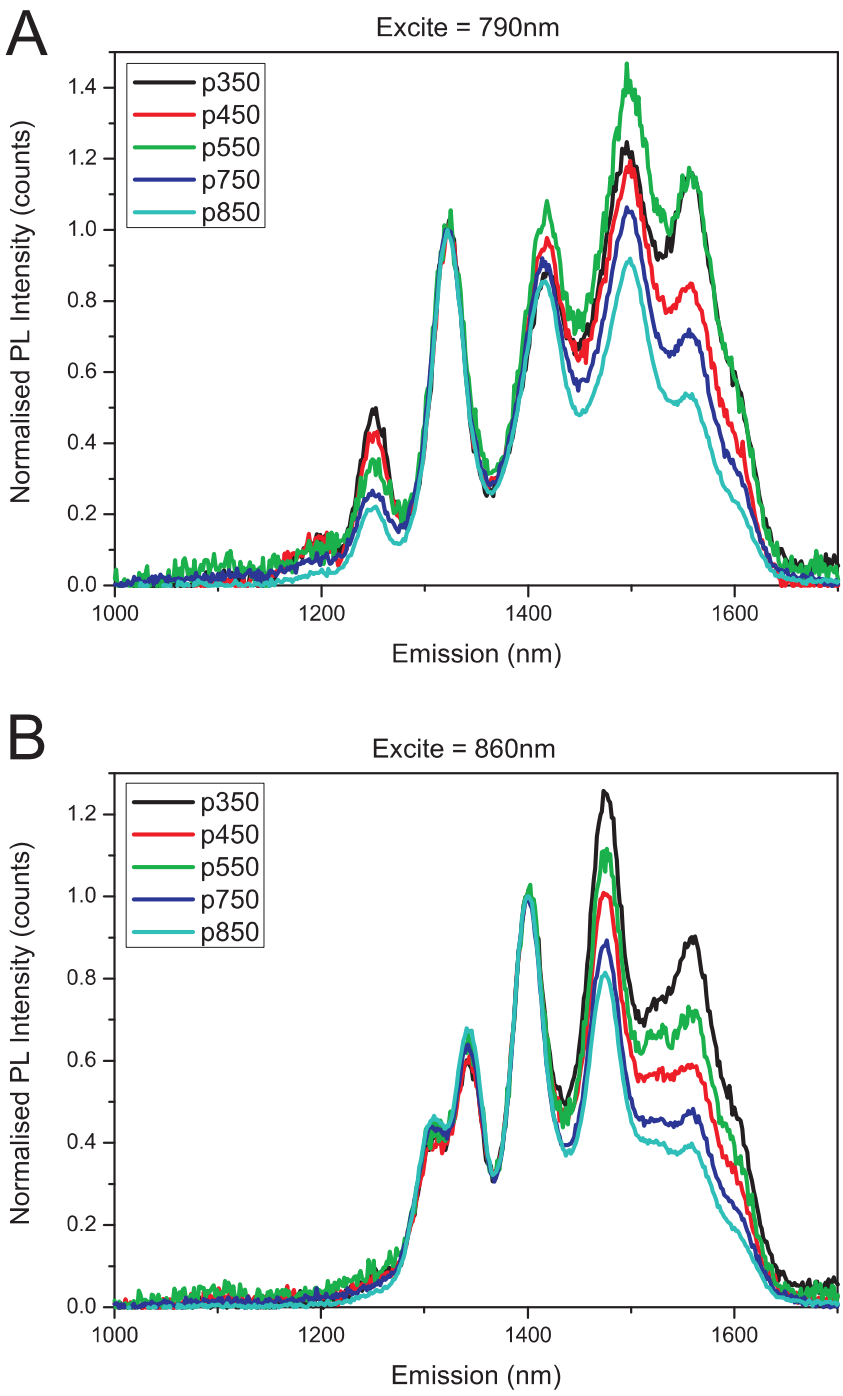


Figure 4.11: Sections from PLE maps taken of SWNTs produced by the laser vaporization method at different growth pressures. Plot A shows spectra taken using 790nm excitation and plot B shows spectra taken with 860nm excitation. For each excite wavelength the spectra have been normalized to one of the central emission peaks.

### 4.6.3 Samples from Nanocyl

Nanocyl is a Belgium based company established in 2002 to manufacture large quantities of carbon nanotubes for commercial clients. Primarily, multi-walled carbon nanotubes are produced for use in relatively low tech applications such as additives in polymer blends where they can increase electrical conductivity or be used as flame retardants. These multi-walled carbon nanotubes are produced in a continuous flow process which has much higher yields than processes for growing SWNTs. Nanocyl are also involved in producing relatively small amounts of research grade double-walled carbon nanotubes as well as single-walled nanotubes. Due to the stricter quality control requirements in producing SWNTs for research and the lack of suitable in-house characterisation equipment a collaboration was established to provide Nanocyl with some feedback on batches of their material.

Figure 4.12 shows PLE maps of material grown by Nanocyl as double-walled carbon nanotubes (DWNTs). The spectra reveal tubes with diameters of between 0.62nm and 1.03nm. The bottom map shows emission in the range 920nm to 1600nm and was recorded with a 1000nm cut-off long pass filter. A map taken with the silicon CCD is also shown which highlights the presence of very narrow diameter tubes. It is unlikely that the luminescence detected in these samples is coming from DWNTs. Whilst it is possible that the particular species of tube shown in these maps could be the inner tubes, it is thought more likely that this emission actually comes from an 'impurity' of SWNTs that arises in the growth process. One reason for suspecting this is that there is no shift in peak positions on these maps verses maps for other SWNT samples. Since the energy levels are very sensitive to the local dielectric environment this suggests that species in this DWNT sample are in an identical environment to SWNTs. Inner tube species are surrounded by another nanotube and thus should have a very different local dielectric environment. Indeed, it is possible that the inner tube species in DWNTs do not emit at all. This would be due to the fact that the outer tubes will always be of lower bandgap and in one third of cases metallic. Charge transfer may thus occur from the photo-excited inner tubes to the outer tube. This would provide a non-radiative pathway for the carriers in the inner tube. If this charge transfer does occur then it should be possible to observe emission at longer wavelengths from these larger tubes. Tests were done in search of this emission but were unable to detect it. A likely explanation for the absence of outer-wall luminescence is that the diameters for these tubes would be on the order of at least 1.28nm (considering a minimum inner tube diameter of 0.62nm and inter-layer

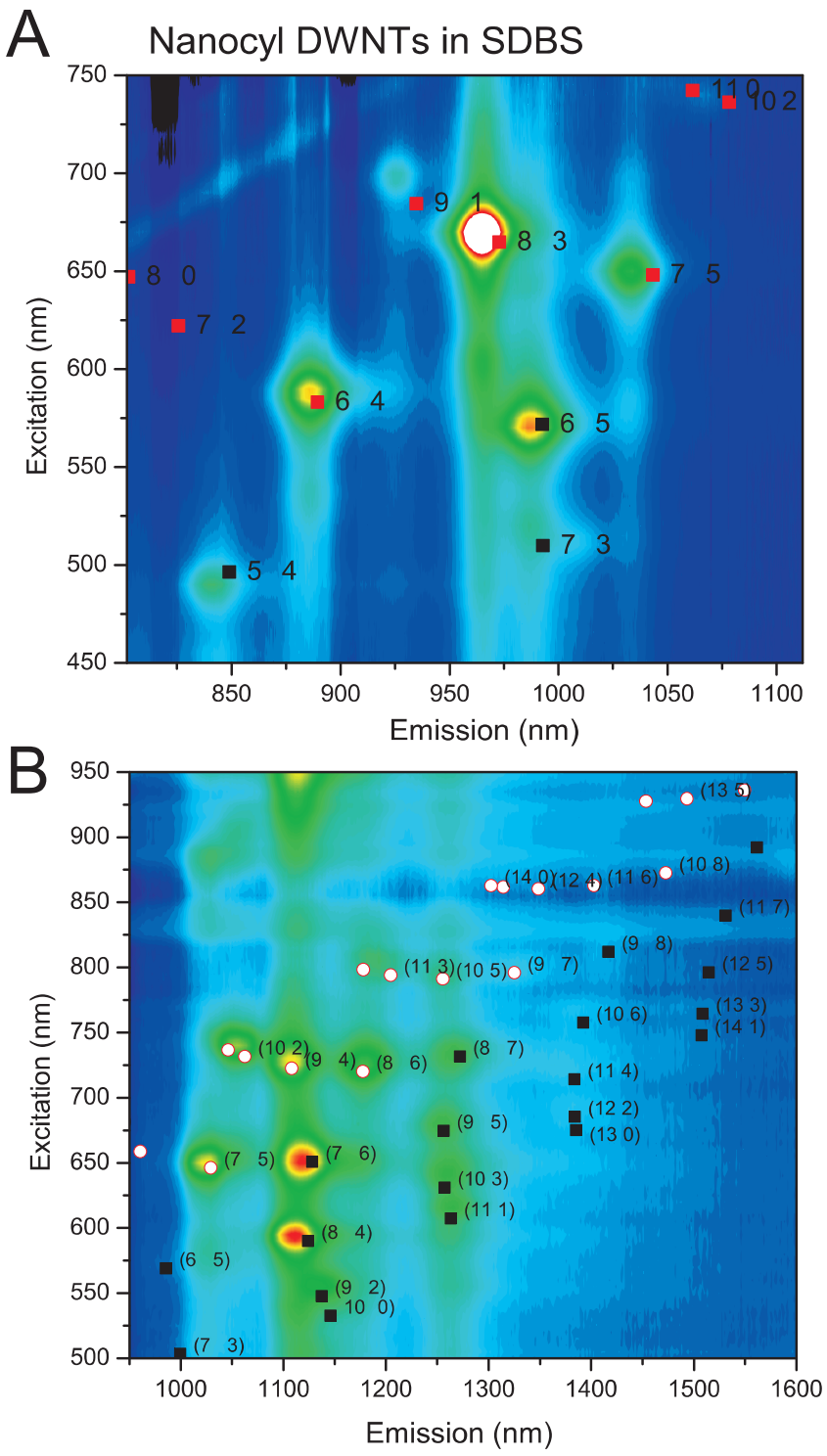


Figure 4.12: CCD and InGaAs PLE maps for Nanocyl DWNT material (plots A&B respectively). It is thought that these emitting species are actually SWNTs which are present as an impurity in the samples.

spacing of 0.33nm). The energy gap of this size of nanotube yields emission which is on the limit of the InGaAs detector and is thus impossible to observe with the current equipment.

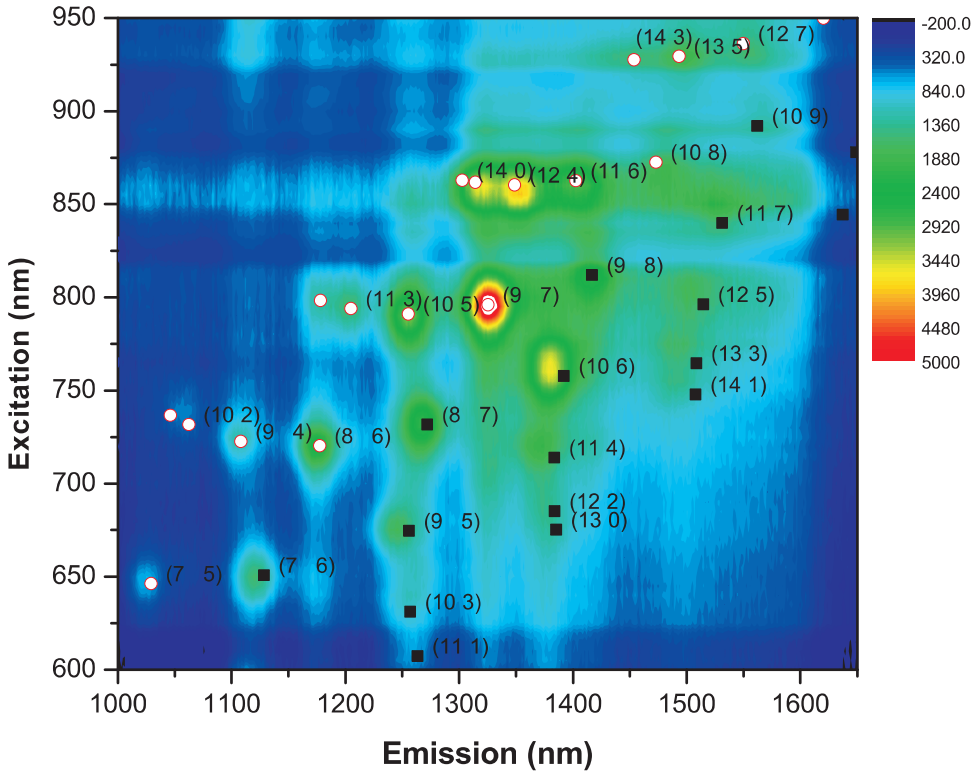


Figure 4.13: PLE maps for Nanocyl SWNTs

Figure 4.13 shows a PLE map of SWNTs grown by Nanocyl. This material is grown in a similar reaction chamber to the to the multi-walled nanotubes but with a different catalyst and reaction conditions. The process is still in the early stages of optimization in terms of product yield and so the samples give relatively low luminescence intensities. PLE mapping was again used here to give a 'fingerprint' of the production process and quantify the presence of the species in the samples. As can be seen from figure 4.13 nanotubes in the diameter range 0.83nm to 1.3nm are produced by this method. It is hoped that with more collaboration it might be possible to further optimize the production process and gain some degree of control over the range of SWNT diameters produced.

## 4.7 Simulated Spectra

A simple Matlab script was written to produce simulated PLE maps of SWNTs in an effort to better characterize samples in terms of their distribution of $(n, m)$ species. In particular it was interesting to test if a uniform Gaussian distribution of diameters could be applied to the simulations in order to replicate the observed PLE maps.

The first step in producing the script was to write a function which could simulate a single peak for typical SWNT luminescence. Although it is commonly accepted [18] that SWNT luminescence has a Voigt line-shape (a combination of Gaussian and Lorentzian features), for the purposes of this simulation a simple Gaussian line-shape was used. The line-width used had a constant FWHM of 20nm, which corresponds to around 20meV at 1100nm. The correct method in retrospect would have been to use a constant energy line-width, nonetheless the advantages of using a more complicated line-shape were judged to be negligible when viewing the final simulated maps. The next step involved setting the relative positions of peaks to match that of the experimentally observed spectra. This was done using semi-empirical data from the paper of Weisman et al. [15] (the same as was used for the 'theoretical positions' used to assign the species in figure 4.9 for example).

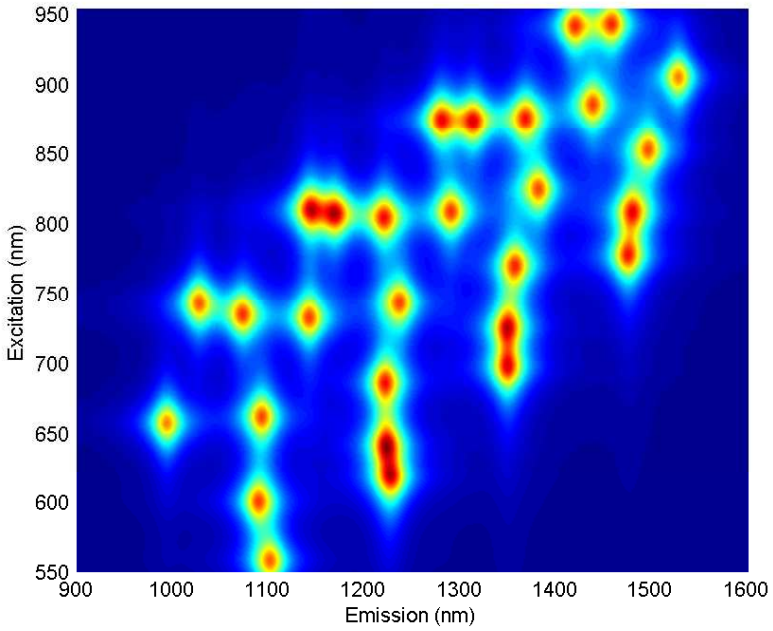


Figure 4.14: Simulated PLE Map with an un-weighted intensity distribution.

Figure 4.14 shows how the simulated PLE map looked at this stage. This is how a SWNT sample would appear if there was an even distribution of species with a constant PL efficiency. Of course in a real SWNT sample the growth process produces a non-uniform distribution of species. To a first approximation this distribution should be close to Gaussian and so applying this function to the diameters of species shown in figure 4.14 results in the pattern shown in figure 4.15.

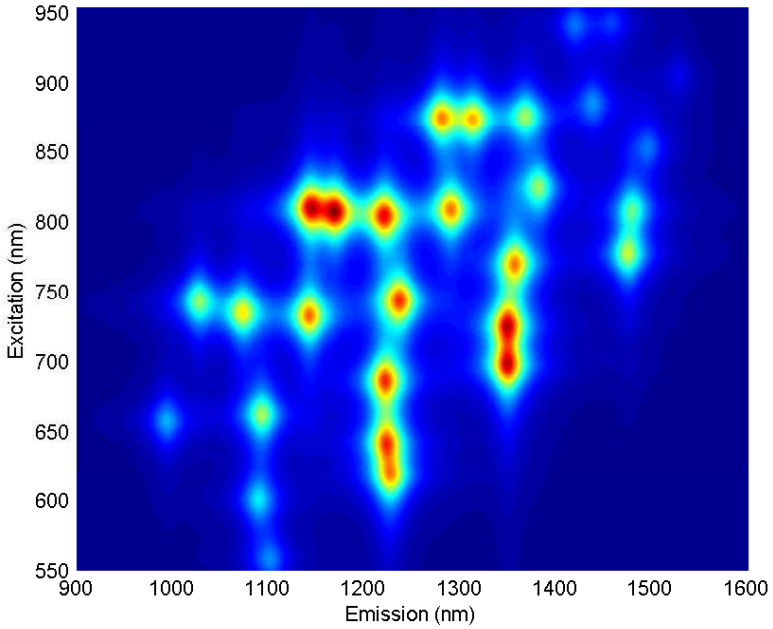


Figure 4.15: Simulated PLE map after weighting the intensities using a Gaussian diameter distribution

Although this map is clearly an improvement it still does not resemble the experimental data. This is because we have neglected the effect of weighting the intensities in terms of their chiral angle. A Gaussian function was again used here to apply a distribution with a weighting towards high chiral angle species.

Adjusting the parameters of the weighting functions, in particular the mean diameter and width of its distribution, allows us to simulate the maps of samples of nanotubes grown by different methods. Figure 4.16 shows a series of simulated maps for SWNTs produced by the CoMoCAT, HiPCO, Laser Vaporisation and Arc Discharge methods. As can clearly be seen in these maps the mean diameter of the species present is increasing from CoMoCAT to Arc. Plotting the Gaussian functions used in weighting the intensities gives us an idea of not only how the mean diameter varies in these different growth processes but also how the width of the distribution varies, the latter being a particular characteristic which could be of practical importance to many technological applications. Figure 4.17

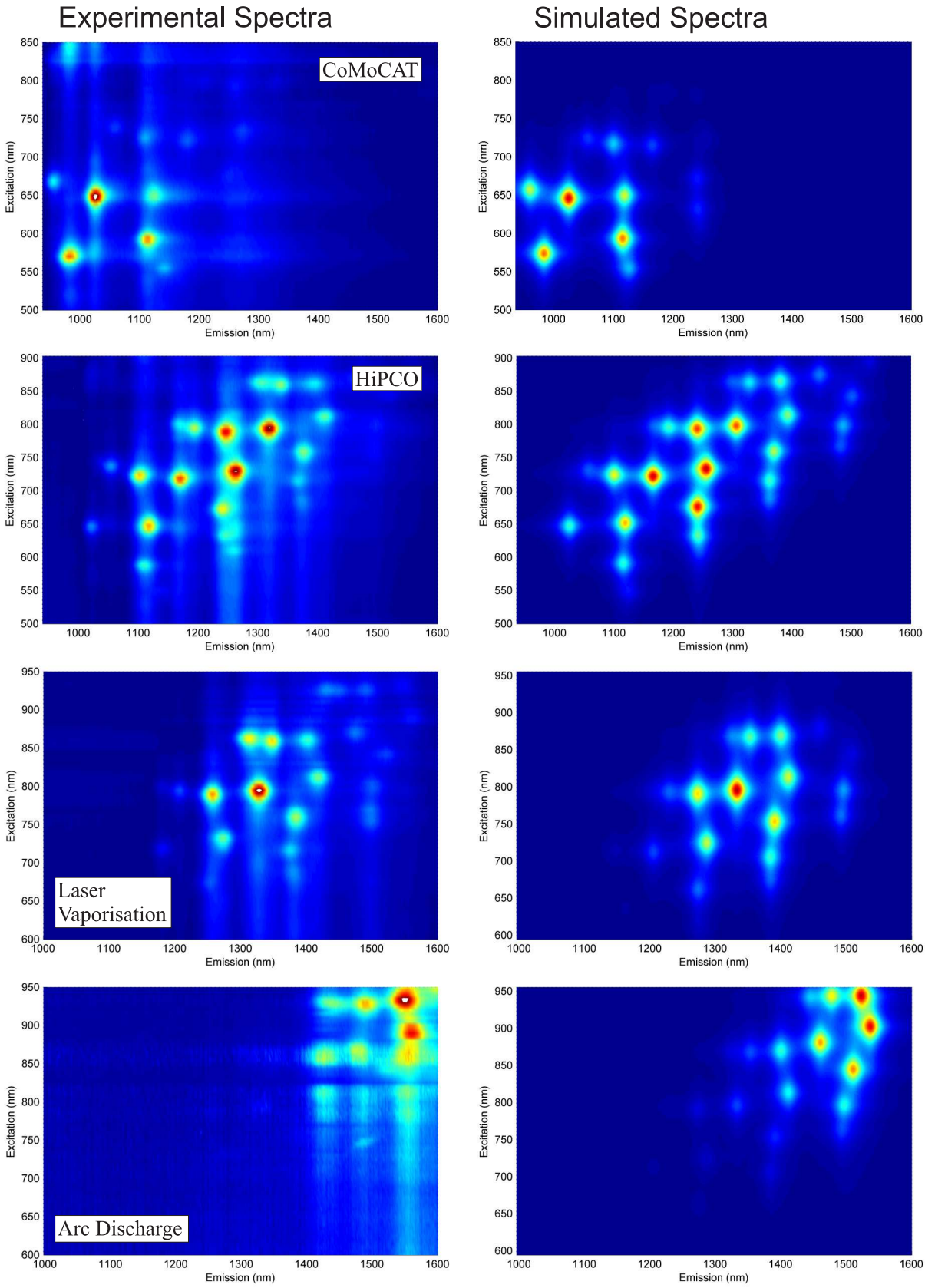


Figure 4.16: Comparison of experimental PLE maps with those generated by the simulation.

shows plots of these Gaussian functions. It has yet to be established whether the SWNT growth process has a symmetric distribution of diameters as is used here or if, as some research suggests [20], the distribution is actually log-normal with a tail extending to larger diameters. This would seem logical if one considers that there should be a strong energetic restriction on the minimum SWNT diameters attainable. It might be possible that the photoluminescence results yield a distribution which is symmetric due to the quantum yield decreasing with increasing diameter. Imaging methods such as TEM or AFM would be better at finding the true distribution of diameters.

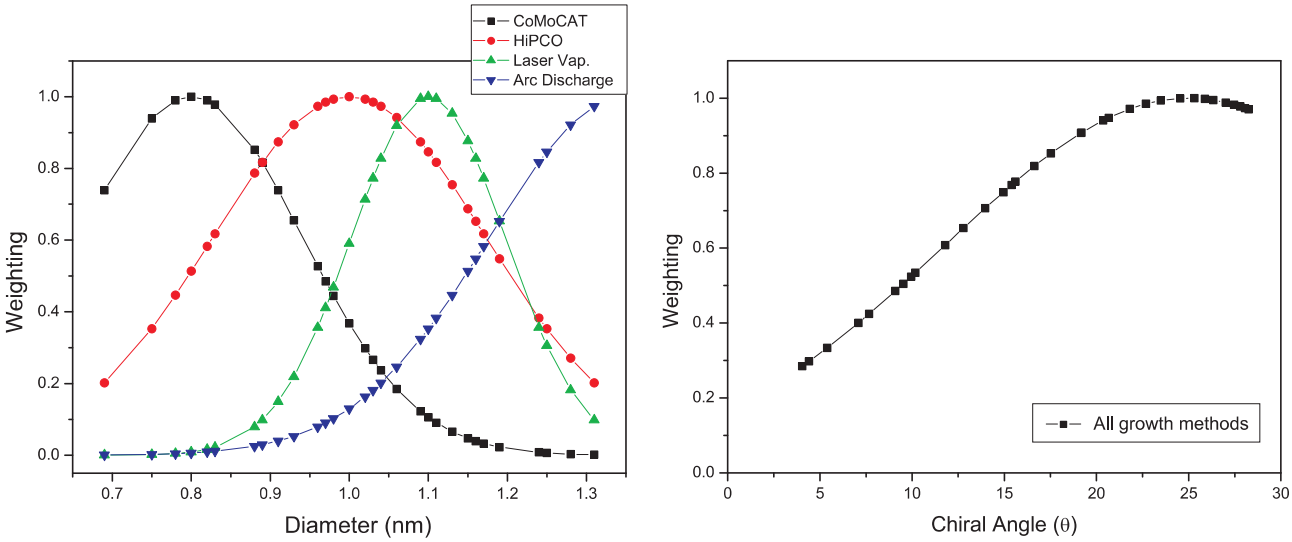


Figure 4.17: The diameter and chiral angle weightings used to generate the simulated spectra shown in figure 4.16. The same chiral angle weighting can be used to simulate nanotubes from each growth method.

The necessity to weight the intensities of the peaks according to chiral angle again raises more questions. It is likely that the growth process should show some preference for growing tubes of a particular chiral angle, such as a tendency towards Zig-zag or towards Armchair. However, it has also been predicted by theoretical studies that the photoluminescence efficiency depends strongly on the chiral angle with Zig-zag tubes having a lower efficiency than Armchair [19, 21]. Thus it could be plausible that the observed distribution in peak intensities comes merely from the variations in the PL quantum yield across the range of tube chiral angles. In a study of electron diffraction patterns from individual SWNTs (performed in a high-resolution TEM), Meyer et al. found the mean angle to be around 24 degrees [22] as opposed to the 15 degrees which would be predicted for a random distribution. This gives credence to the argument that the chiral angle weighting used here is reflective of the population of SWNTs. More work needs to be done on this to establish the reliability of photoluminescence measurements at deducing chiral populations.

Although at first glance the simulated spectra look fundamentally similar to the experimental PLE maps, there are in fact some interesting features in the real maps apart from the $E_{22}$-$E_{11}$ resonances. The most obvious and well studied of these are the phonon assisted transitions, the $E_{12}/E_{21}$ transitions and the Raman lines.

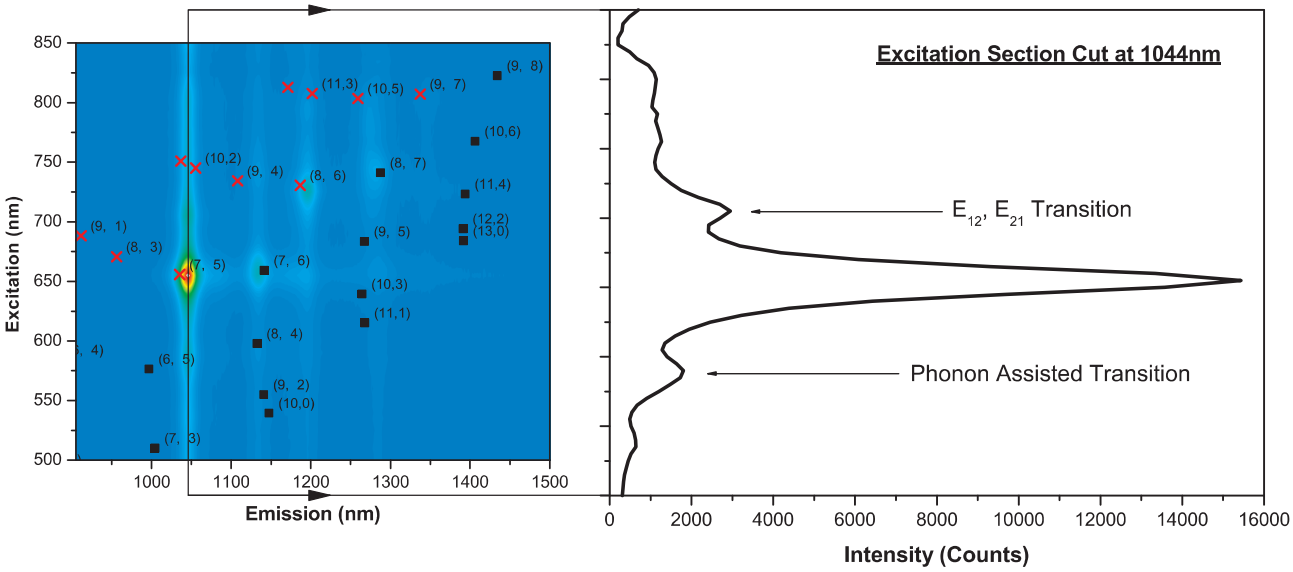


Figure 4.18: PLE map and Cross section

Figure 4.18 shows a good example of additional features on a PLE map of CoMoCAT material dispersed in an organic polymer (to be discussed in chapter 5). A cross section cut of the map along the PL peak at 1044nm shows the detail of the absorbance processes which produce the (7,5) SWNT emission. As well as the main $E_{22}$ peak at 655nm there is also a sideband ~200meV higher in energy. This absorbance occurs due to the coupling of the normal electronic transition and a vibrational mode (an LO phonon). They are called phonon assisted transitions and occur for all SWNT species at around the same energy separation from both the $E_{22}$ and $E_{11}$ states. Further explanation of the origin and behavior of these exciton-phonon virtual states are detailed in the literature [23, 24]. Also highlighted in figure 4.18 is an absorbance peak at lower energy than the main excitation. This feature has only recently been studied in depth and is thought to be due to absorbance through both the $E_{12}$ and $E_{21}$ pathways [25]. These transitions are forbidden for light polarized parallel to the SWNT axis but can occur weakly when the incident light is polarized perpendicular to the nanotube [26].

Visible in the top left hand corner of the CoMoCAT sample in figure 4.16 are other features which are not included in the simulated spectra. These are often seen in the maps as diagonal streaks - a good example can be seen in the top PLE map of figure 4.12. These lines occur due to inelastic Raman

scattering of photons by the carbon-carbon bond modes of the SWNT. Here, the incident photon loses an amount of energy exactly corresponding to the mode frequency, meaning the scattered light is at longer wavelengths. As the frequency of incident light is decreased the scattered frequency decreases linearly as the energy lost exciting a specific mode is constant. Again, detailed explanations of these features can be found in the literature [27].

## 4.8 Summary and Future Work

We have shown that optical spectroscopy and in particular photoluminescence-excitation mapping is a useful characterisation technique and yields novel effects in the physics of single-walled nanotubes. It's importance stems from the ability to quantitatively probe the relative populations of the distinct $(n, m)$ species in the samples and from the high throughput of material which is tested. The latter point has benefitted dramatically from the automation of the equipment for scanning the excitation source whilst acquiring the emission spectra. This has enabled not only the improvement of sample preparation but also the subsequent thorough investigation of SWNTs from different sources.

Simulation of the PLE maps has made it possible to test the theory that the diameter distribution is roughly Gaussian. An excellent agreement and verification of this can be seen when directly comparing the experimental data with that of the simulations. Interestingly the distribution of chiral angles is also found to closely follow a Gaussian distribution. Future work should hopefully elucidate the contribution which variations in the chiral angle dependent photoluminescence yield have on this.

The interest in SWNT properties and need for their characterisation is by no means limited to the 30 or so species which have been looked at in this chapter. Current restrictions are entirely due to equipment performance rather than availability of samples. As was discussed previously the InGaAs detector used for most of our PLE mapping work has a bandgap corresponding to a wavelength around 1.6$\mu$m. This places a restriction on the ability to detect SWNT emission as we extend into the infra-red, where larger diameters of nanotube species have bandgaps. Future work could focus on larger diameters of SWNTs. This would not only broaden the range of samples which could be tested, but also possibly provide new physical behaviors to study.

# Bibliography


[1] P. Atkins and J. de Paula. *Atkins' Physical Chemistry.* Oxford University Press, 7th edition, 2002.

[2] J. Hollas. *Modern Spectroscopy.* Wiley, 1987.

[3] J. Lefebvre, S. Maruyama and P. Finnie. Photoluminescence:Science and Applications. *Topics in Applied Physics: Carbon Nanotubes*, 111:287–319, 2008.

[4] J. A. Misewich, R. Martel, Ph. Avouris, J. C. Tsang, S. Heinze and J. Tersoff. Electrically Induced Optical Emission from a Carbon Nanotube FET. *Science* 300(5620):783–786, 2003.

[5] M. Freitag, V. Perebeinos, J. Chen, A. Stein, J. C. Tsang, J. A. Misewich, R. Martel and Ph. Avouris. Hot Carrier Electroluminescence from a Single Carbon Nanotubes. *Nano Lett.* 4(6):1063–1066, 2004.

[6] F. Wang, G. Dukovic, L. E. Brus and T. F. Heinz. Time-Resolved Fluorescence of Carbon Nanotubes and Its Implication for Radiative Lifetimes. *Phys. Rev. Lett.* 92:177401, 2004.

[7] J. M. Bonard, T. Stora, J. P. Salvetat, F. Maier, T. Stockli, C. Duschl, L. Forro, W. A. de Heer and A. Chatelain. Purification and size-selection of carbon nanotubes. *Adv. Mater.*, 9(10):827–831, 1997.

[8] M. J. O'Connell, S. M. Bachilo, C. B. Huffman, V. C. Moore, M. S. Strano, E. H. Haroz, K. L. Rialon, P. J. Boul, W. H. Noon, C. Kittrell, J. Ma, R. H. Hauge, R. B. Weisman and R. E. Smalley. Band gap fluorescence from individual single-walled carbon nanotubes. *Science*, 297:593–596, 2002.

[9] S. M. Bachilo et al. Structure-assigned optical spectra of single-walled carbon nanotubes. *Science* 298:2361–2366, 2002.

[10] R. B. Weisman, S. M. Bachilo and D. Tsyboulski. Fluorescence spectroscopy of single-walled carbon nanotubes in aqueous suspension. *Appl. Phys. A* 78:1111–1116, 2004.

[11] T. Ando. Excitons in Carbon Nanotubes. *J. Phys. Soc. Jpn.*, 66:1066, 1997.

[12] F. Wang, G. Dukovic, L. E. Brus and T. F. Heinz. The Optical Resonances in Carbon Nanotubes arise from excitons. *Science*, 308:838, 2005.

[13] J. Maultzsch, R. Pomraenke, S. Reich, E. Chang, D. Prezzi, A. Ruini, E. Molinari, M. S. Strano, C. Thomsen and C. Lienau. Exciton binging energies in carbon nanotubes from two-photon photoluminescence. *Phys. Rev. B*, 72:241402, 2005.

[14] J. Lefebvre, D. G. Austing, J. Bond and P. Finnie. Photoluminescence imaging of suspended single-walled carbon nanotubes. *Nano. Lett.* 6:1603–1608, 2006.

[15] R. B. Weisman and S. M. Bachilo. Dependence of optical transition energies on structure for single-walled carbon nanotubes in aqueous suspension: An empirical kataura plot. *Nano. Lett.*, 3:1235–1238, 2003.

[16] P. Nikolaev *et al.* Gas-phase catalytic growth of single-walled carbon nanotubes from carbon monoxide. *Chem. Phys. Lett.* 313:91–97, 1999.

[17] S. M. Bachilo *et al.* Narrow (n,m)-distribution of single-walled carbon nanotubes grown using a solid supported catalyst. *J. Am. Chem. Soc.* 125:11186–11187, 2003.

[18] M. Jones *et al.* Analysis of photoluminescence from solubilized single-walled carbon nanotubes. *Phys. Rev. B* 71:115426, 2005.

[19] S. M. Reich, C. Thomsen and J. Robertson. Exciton resonances quench the photoluminescence of Zig-zag carbon nanotubes. *Phys. Rev. Lett.* 95(7):077402, 2005.

[20] Z. Luo, L. D. Pfefferle, G. L. Haller and F. Papadimitrakopoulos. (n,m) Abundance Evaluation of Single-Walled Carbon Nanotubes by Fluorescence and Absorption Spectroscopy. *J. Am. Chem. Soc.* 128(48):15511–15516, 2006.

[21] Y. Oyama, R. Saito, K. Satoa, J. Jianga, G. Samsonidzee, A. Grneis, Y. Miyauchi, S. Maruyama, A. Jorio, G. Dresselhaus and M. S. Dresselhaus. Photoluminescence intensity of single-wall carbon nanotubes. *Carbon* 44(5):873–879, 2006.

[22] J. C. Meyer, M. Paillet, G. S. Duesberg and S. Roth. Electron diffraction analysis of individual single-walled carbon nanotubes. *Ultramicroscopy*, 106:176–190, 2006.

[23] S. G. Chou, F. Plentz, J. Jiang, R. Saito, D. Nezich, H. B. Ribeiro, A. Jorio, M. A. Pimenta, G. Samsonidze, A. P. Santos, M. Zheng, G. B. Onoa, E. D. Semke, G. Dresselhaus and M. S. Dresselhaus. Phonon-Assisted Excitonic Recombination Channels Observed in DNA-Wrapped Carbon Nanotubes Using Photoluminescence Spectroscopy. *Phys. Rev. Lett.*, 94:127402, 2005.

[24] F. Plentz, H. B. Ribeiro, A. Jorio, M. S. Strano and M. A. Pimenta. Direct experimental evidence of exciton-phonon bound states in carbon nanotubes. *Phys. Rev. Lett.*, 95:247401, 2005.

[25] S. Lebedkin, F. Hennrich, O. Kiowski and M. M. Kappes. Photophysics of carbon nanotubes in organic polymer-toluene dispersions: Emission and excitation satellites and relaxation pathways. *Phys. Rev. B.*, 77:165429, 2008.

[26] K.-C. Chuang, A. Nish, J.-Y. Hwang, G. Evans and R. J. Nicholas. An experimental study of coulomb corrections and single particle energies for single-walled carbon nanotubes using cross-polarized photoluminescence. *Phys. Rev. B.*, In Press, 2008.

[27] C. Thomsen and S. Reich. Raman scattering in carbon nanotubes. *Topics in Applied Physics: Light Scattering in Solids IX*, 108:115–235, 2007.

# Chapter 5

# Selective Dispersion of SWNTs

## 5.1 Background

Isolating SWNTs has proved to be one of the major difficulties in the investigation of some of the unique physical properties of these materials. Many studies have used surfactants, such as sodium dodecyl sulphate [1] or the superior sodium dodecylbenzene sulfonate (SDBS) [2], to disperse SWNTs. The carbon surface of the nanotube is highly hydrophobic and leads to an energetically favorable interaction with the aliphatic chain of the surfactant in aqueous dispersion. Thus the surfactant is thought to efficiently coat the nanotube surface providing both stearic repulsion and colloidal stability to the dispersion. Coupled with strong sonication and ultracentrifugation this method is highly effective at yielding dispersions with high proportions of isolated individual tubes [3]. Refinements of this technique, using multiple, density-gradient ultracentrifugation are able to introduce tube selectivity [4], although these methods do require significant experimental complexity.

Photoluminescence (PL) spectroscopy [5] can be used to assess the effectiveness of the dispersing agent at breaking up the aggregates of nanotubes known as bundles. The usefulness of this technique arises from the presence of metallic SWNTs, which account for a third of all nanotube species in any ensemble sample. The metallic tubes provide efficient non-radiative decay pathways for any photo-excited carriers in a nanotube bundle. Thus the PL efficiency of nanotube samples bears a direct relationship to the degree of de-bundling and the isolation of individual semiconducting species.

Another route which has been used to disperse SWNTs is by using DNA [6]. This differs from the surfactant in that DNA is a long helical molecule and is likely to enclose the nanotube by wrapping its helix around the cylindrical structure of the tube. Several authors have used this technique to purify SWNTs and showed it to be efficient at narrowing the diameter distribution [7]. In contrast to surfactants which are thought to coat all the material, including impurities, in a given raw nanotube sample, DNA seems to have a preferential interaction with certain tube species. It is thought that this effect might be further enhanced by using macromolecules such as conjugated polymers [8, 9] with structures which closely match the surface of the SWNT [10, 11]. This would result in selective solubilization of not only certain diameters of nanotubes but also certain species, where the polymer's backbone or side-chains favorably wrap around a particular SWNT structure [12, 13].

In this chapter it is demonstrated using PLE mapping and optical absorbance spectroscopy that aromatic organic polymers have the potential to selectively solubilize certain nanotube species. Relatively small changes in the polymer structure lead to selection on the basis of both chiral angle and nanotube diameter. The polymer poly(9,9-dioctylfluorenyl-2,7-diyl), here referred to as PFO, has shown particularly strong selectivity and leads to much improved optical spectra. Computer simulations of the interaction of PFO with SWNTs of various diameters give some insight into the mechanism which causes the selectivity but ultimately show the system to be more complex than can be currently modeled.

## 5.2 Methods

The polymers used in this study were purchased from American Dye Source Inc. They were poly[9,9-dioctylfluorenyl-2,7-diyl] (PFO), poly[9,9-dihexylfluorenyl-2,7-diyl] (PFH), poly[(9,9-dioctylfluorenyl-2,7-diyl)-co-(1,4-phenylene)] (PFO-P) and poly[(9,9-dioctylfluorenyl-2,7-diyl)-alt-co-(1,4-benzo-2,1',3-thiadiazole)] (PFO-BT). The molecular weights quoted by the supplier were $M_W$=7,500-30,000 for PFO-BT and $M_W$=40,000-150,000 for the other polymers. Samples of single-walled carbon nanotubes studied came from the HiPCO [14] and CoMoCAT [15] processes. The powders were used as purchased with quoted purities of >85% SWNTs (HiPCO) and >90% (CoMoCAT). Samples grown by laser vaporization were provided by Björn Hornbostel of the Max-Planck-Institut für Festkörperforschung, Stuttgart, Germany and were of undetermined purity. All other chemicals used were purchased from Sigma Aldrich. The nanotube powders were dispersed in solutions in the ratio 5mg SWNT: 6mg polymer: 10ml solvent. The dispersions were then homogenized in a sonic bath for 60 minutes followed by vigorous sonication using the ultrasonic probe apparatus for 15 mins. This was then promptly followed by centrifugation at 9000g for 3 minutes.

The preparation procedure for dispersions in sodium dodecylbenzene sulfonate (SDBS), used here for comparison with PFO, consisted of 5mg SWNT: 350mg surfactant: 35ml $D_2O$. These were then sonicated and centrifuged as described in chapter 3. It is worth noting that a much lower centrifugal force and time duration was found to be sufficient to remove the non-dispersed nanotubes in our polymer samples compared to the aqueous surfactants. Absorbance measurements were taken using

a Perkin-Elmer Lambda 9 Photospectrometer. Raman spectra were taken using a Krypton laser at 647nm with an incident power of <1mW. The light was collected from the sample in a back scattering geometry and recorded using a Jobin-Yvon triple grating spectrometer fitted with a liquid nitrogen cooled silicon CCD detector. Photoluminescence Excitation (PLE) mapping was done using the automated custom built system described in chapter 4.

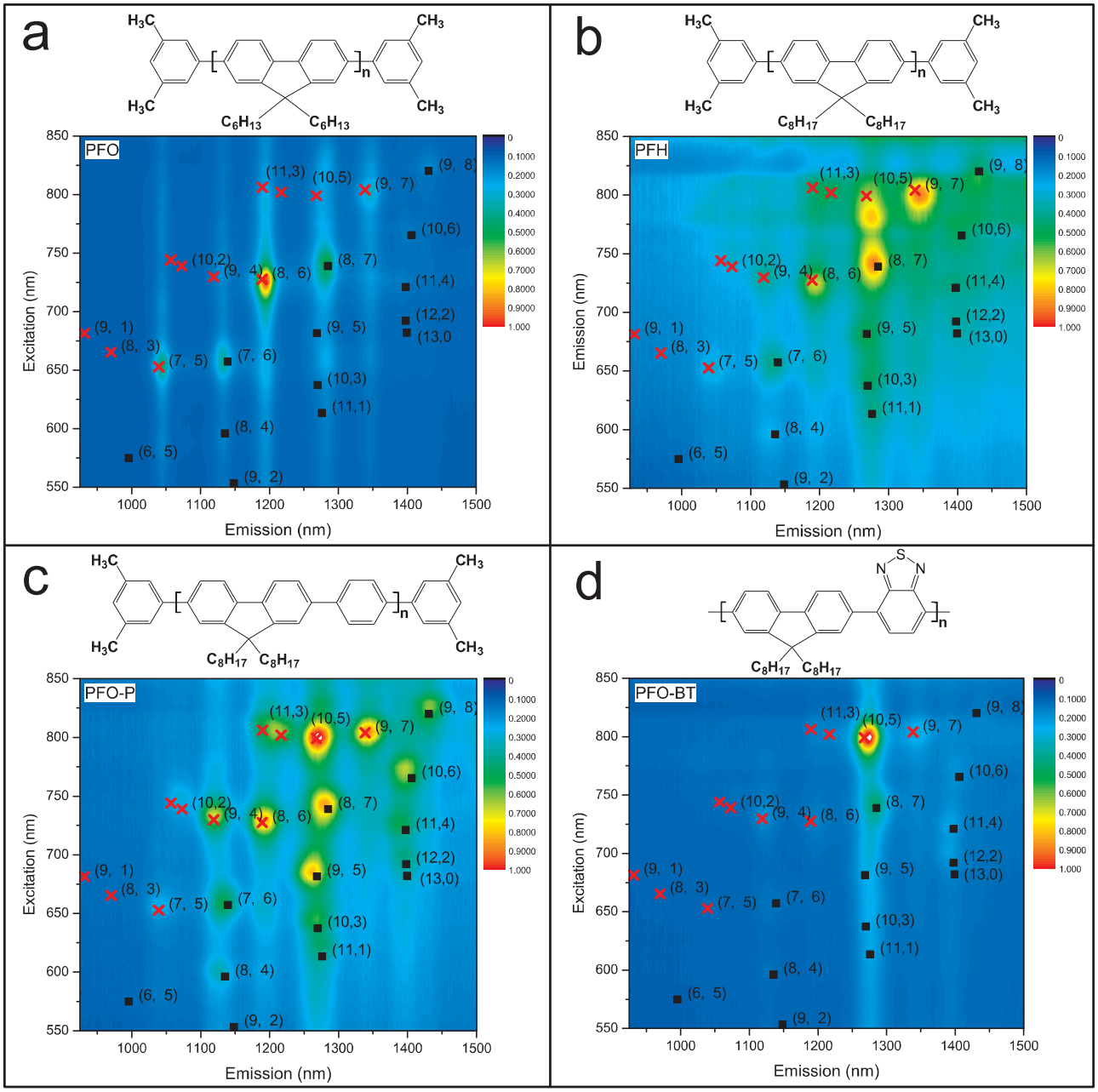


Figure 5.1: PLE maps of various polymer-SWNT samples in toluene dispersions prepared using nanotubes grown by the HiPCO process as starting material. The false colour indicates the strength of the emission and the positions of the peaks, unique for each nanotube species, have been indicated here by their $(n,m)$ indexed points that come from a semi-empirical model. The red crosses correspond to the family of tube species for which $q$=-1 and the black squares to the family where $q$=+1. Parts a to d describe the maps for the polymers PFO, PFH, PFO-P and PFO-BT, whose repeat structures are shown.

## 5.3 Results

The series of polymers listed in the methods section were found to produce excellent dispersions as judged by using optical spectroscopy. These polymers are all related by the fact that they contain the fluorene structure as part of their repeat unit, leading to the formation of a stiff backbone. Figure 5.1 shows photoluminescence-excitation (PLE) maps of SWNTs produced by the HiPCO process dispersed in the solvent toluene using the polymers whose structures are shown, chosen to show examples of representative data which have different degrees of selectivity. Photoluminescence spectroscopy has been used to verify the solubilization due to the sensitivity which it has to the degree of SWNT exfoliation. The peaks correspond to the resonantly enhanced emission from the SWNTs' primary $E_{11}$ electronic transitions when the excitation matches their secondary $E_{22}$ electronic levels [5]. The points indicate theoretical positions for the energy gaps of the corresponding ($n$,$m$) indexed tube species. For the polymer-SWNT maps these points have been redshifted by 1.3% from those given by Weisman et al. for the case of SWNTs dispersed using an aqueous surfactant [16]. This shift is attributed to a difference in the local dielectric environment where the increased dielectric screening causes a reduction of the electron-electron and excitonic Coulomb interactions which produce a net reduction in the energy gap [17]. Other resonant features which are visible at higher and lower energy excitation relative to $E_{22}$ also result in emission from the same $E_{11}$ energy gaps and can be attributed to previously established phonon [18] and weakly allowed absorption [19] effects.

The maps show that the distribution of SWNT species depends strongly on the structure of the polymer used. Whilst all the polymers induce some selectivity over the nanotubes which have been solubilized, PFO and PFO-BT have by far the most dramatic influence on the number of species dispersed. This selectivity is not only very sensitive to slight alterations in the polymer structure, as is shown here, but also to changes in the solvent used. Replacing toluene with other organic solvents such as THF and chloroform was found to reduce the selectivity and produces PLE maps with many more SWNT species present.

Figure 5.2 shows a direct comparison between the spectra obtained for SWNTs from the HiPCO and CoMoCAT processes when dispersed in the PFO/toluene solutions and in aqueous surfactants. It shows a clear reduction in the number of radiative species in the polymer-SWNT suspensions.

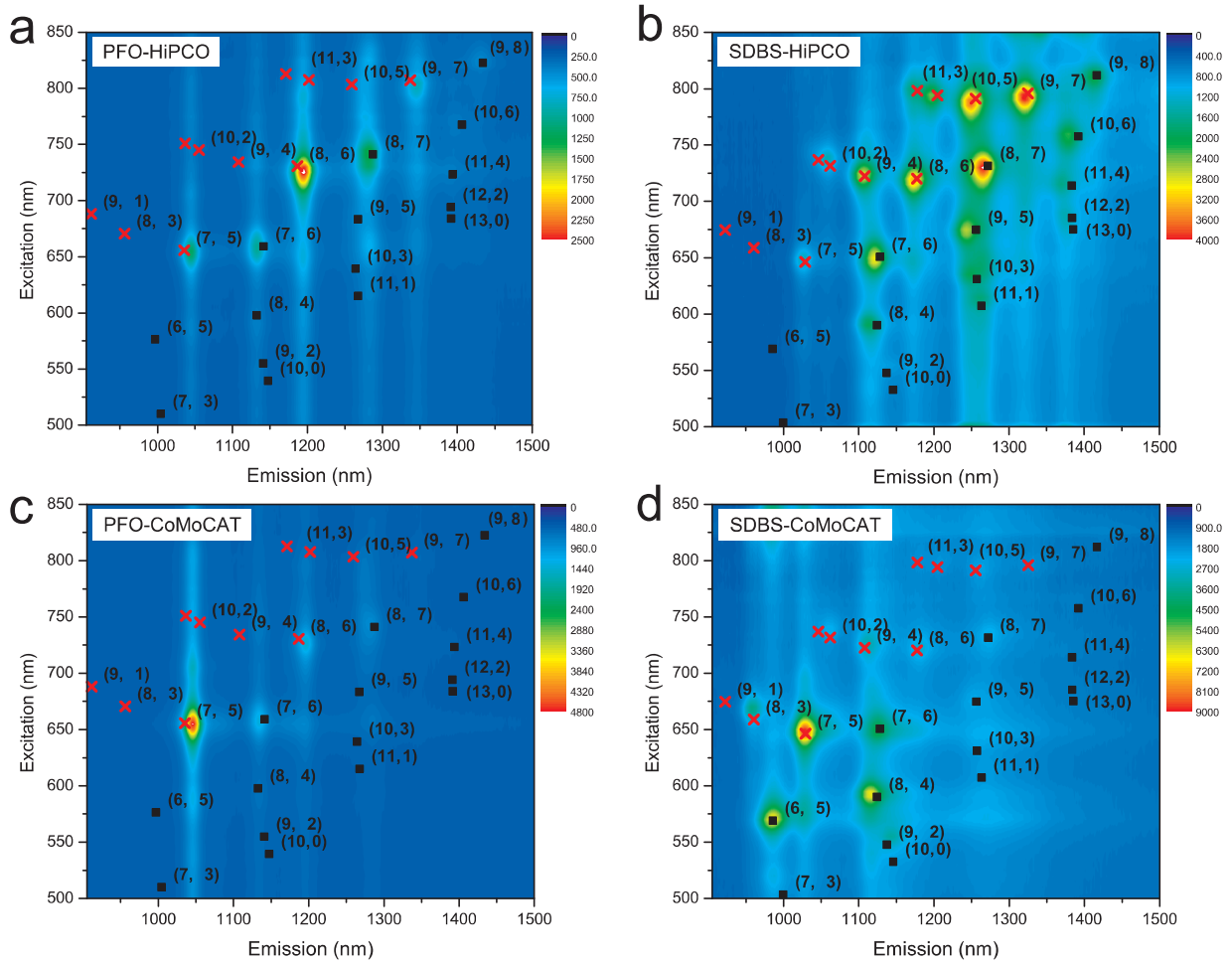


Figure 5.2: PLE maps of nanotubes produced by the HiPCO and CoMoCAT growth processes in PFO/toluene dispersions (a & c) and in aqueous surfactant (b & d).

To understand this selective solubilization process we[†] performed molecular mechanics simulations [20] using the MM3 force field [21] to model the interaction between PFO and SWNTs. The mechanism by which the these polymers encase the SWNTs studied is similar to that proposed by Chen et al. [11], who showed that rigid aromatic polymers could solubilize SWNTs by aligning their backbone along the nanotube surface in order to maximize the interaction between $\pi$-bonds. We found that the polymer can form a tight ordered structure around the SWNT with a fixed distance between the nanotube surface and the polymer shell approximately equal to twice the van der Waals radius of a carbon atom. Also, the structure has an n-fold symmetry where the number of polymer units wrapping the nanotubes is related to the tube diameter and the side chain length. A plot of the binding energy verses SWNT diameter can be seen in figure 5.3. The overall trend shows that the total binding energy increases with increasing nanotube diameter, however, there are two discontinuities where the favorable interaction swaps from two polymer chains surrounding the tube to three and then to four.

[†]Initial simulation work was performed by myself and then elaborated on by another DPhil student, James Doig.

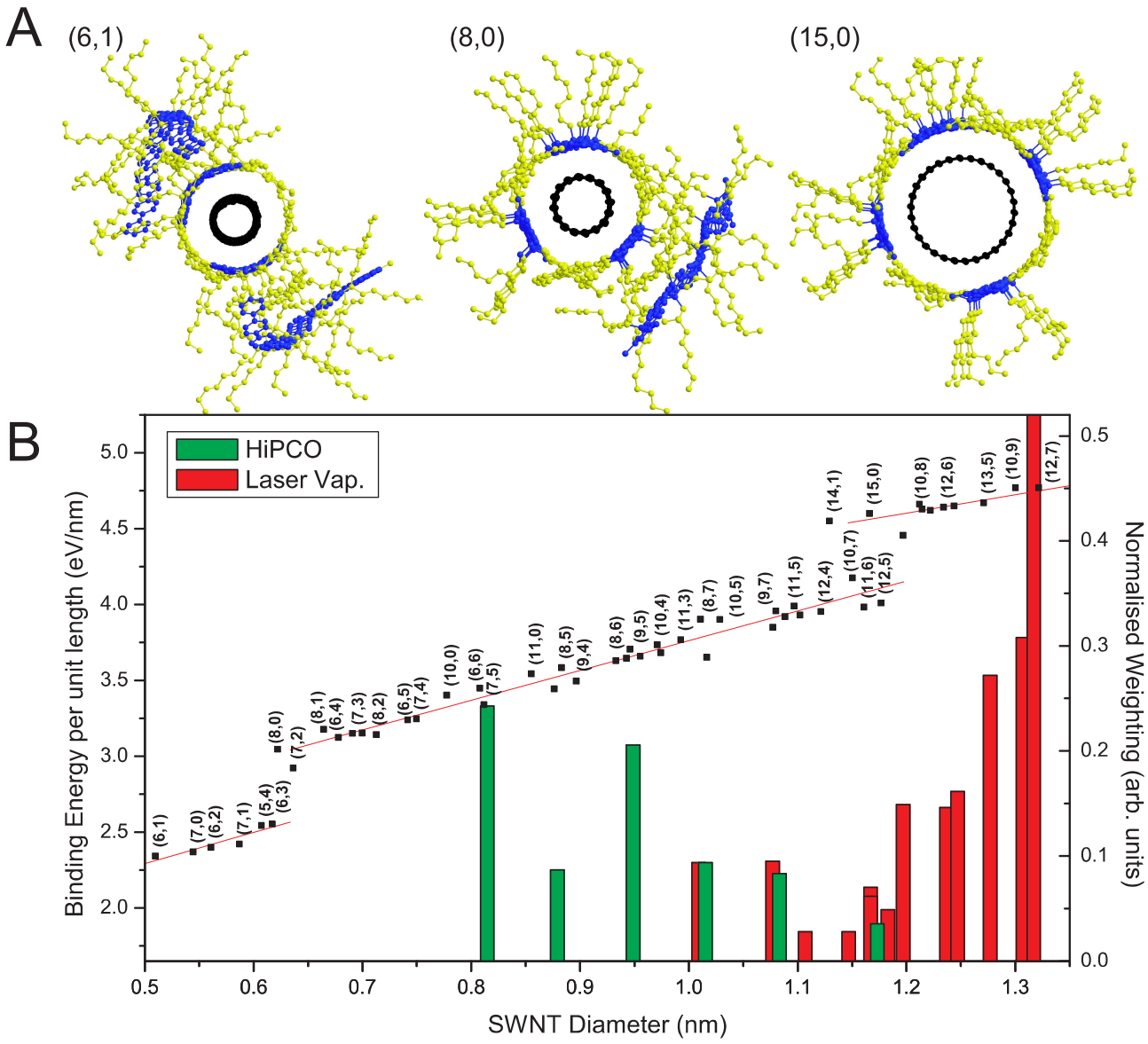


Figure 5.3: Molecular mechanics simulations of the polymer wrapping mechanism. Part A - The model structures show radial views of three nanotube species encased with PFO chains of six repeat units in length with the polymer backbone coloured in blue and the side chains in yellow. Part B - Calculated SWNT-polymer interaction energies for these simulations show a discontinuous dependence of the binding energy on nanotube diameter due to the favorable wrapping mechanism changing from two polymer chains to three and then to four. The histogram gives the experimentally determined weighting which the polymer imposes across the range of nanotube diameters that were accessible by PLE mapping, using nanotubes grown by the HiPCO and laser vaporization growth processes.

Model structures shown in figure 5.3 highlight this, where we have a (6,1) nanotube encased in two polymer molecules, an (8,0) nanotube encased in three polymers and a (15,0) encased in four. With the first two examples it is possible to see the extraneous polymer strands adjacent. The modeling suggests therefore that the nanotube solubilization might be strongly diameter dependent. This can be seen experimentally in the histogram which is given in figure 5.3. This has been produced from the experimental data by normalizing the SWNT-PFO PL intensities using the intensities from maps of nanotubes dispersed in aqueous surfactant. Since the aqueous surfactant is assumed to be non-selective, normalizing in this manner will give an accurate representation of the preference which the PFO polymer has for solubilizing particular diameters of nanotube. Starting materials produced by both the HiPCO and laser vaporization [22] growth processes have been used here to give a wide range of diameters. The minimum weighting in the histogram correlates strongly with the instability in the wrapping process where the polymer is jumping between different n-fold wrapping scenarios, thus providing a potential mechanism for the diameter selectivity. In addition to the diameter dependence, however, there is also a strong selection of high chiral angle tubes at small diameters, suggesting that more than one mechanism is responsible for the full behavior seen. Simulations of the interactions of the other polymers such as PFH show the formation of similar ordered structures at slightly different diameters but do not give any obvious explanation for the differences in selective solubility shown in figure 5.1.

One significant consequence of the selectivity of the polymers is that the remaining SWNT optical resonances become much better resolved. This is shown in the absorbance spectra of figure 5.4 for SWNTs produced by the HiPCO and CoMoCAT processes dispersed in aqueous SDBS and in PFO/toluene solutions. Three important differences are observed between the two dispersions for both SWNT materials. Firstly the total absorbance is substantially smaller in the case of the PFO/toluene dispersions. Secondly the absorption features are significantly narrowed and much more clearly resolved than in the case of the aqueous dispersion, and thirdly the underlying background is very significantly reduced. We attribute the difference to a very substantial reduction in the number of different nanotube species present in the PFO/toluene dispersions, combined with enhanced purification. As a result the peaks observed in absorbance can easily be resolved and assigned to those seen in the PLE maps, in contrast to the absorbance spectra from the aqueous dispersions where the presence of multiple species causes convolution of the absorption peaks making detailed analysis very difficult.

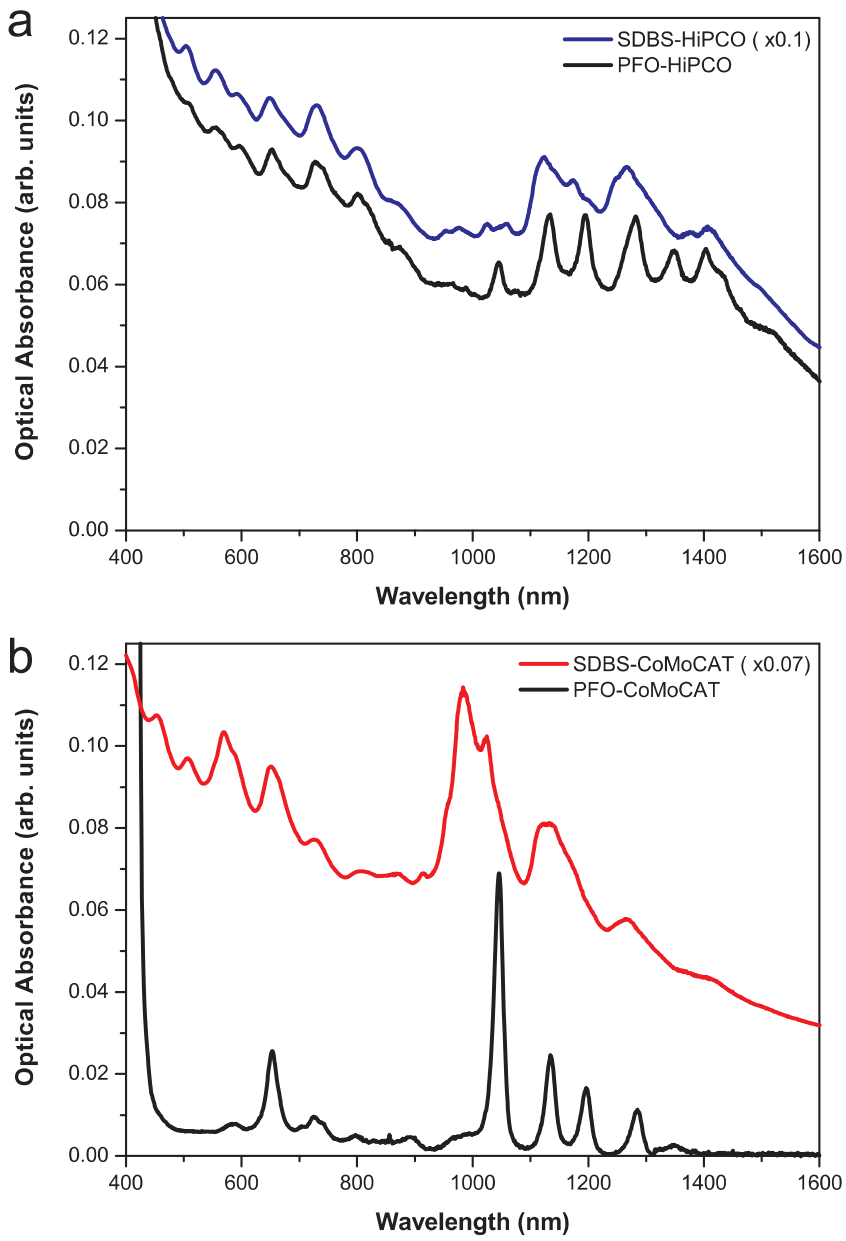


Figure 5.4: Absorbance spectra comparing SWNTs from separate growth methods dispersed in aqueous SDBS surfactant solution (red and blue lines) and in toluene dispersions of the polymer PFO (black lines). a, Samples prepared using material grown by the HiPCO process as the starting material. b, Samples prepared using material from the CoMoCAT growth process. The absorption edge at 450nm is due to the polymer. No background subtraction has been made for any of these spectra.

| $n$ | $m$ | q | Diameter (nm) | HiPCO Absorb. | PL | CoMoCAT Absorb. | PL |
|---|---|---|---|---|---|---|---|
| 7 | 5 | -1 | 0.83 | 0.08 | 0.16 | 0.58 | 0.65 |
| 7 | 6 | +1 | 0.90 | 0.21 | 0.13 | 0.19 | 0.13 |
| 8 | 6 | -1 | 0.97 | 0.21 | 0.39 | 0.13 | 0.15 |
| 8 | 7 | +1 | 1.03 | 0.24 | 0.18 | 0.08 | 0.06 |
| 9 | 7 | -1 | 1.10 | 0.15 | 0.10 | 0.02 | 0.01 |
| 9 | 8 | +1 | 1.17 | 0.11 | 0.04 | - | - |

Table 5.1: Relative molecular fractions of selected ($n$,$m$) semiconducting nanotube species as deduced from relative absorbance & compared to their relative PL emission intensities. The values for the HiPCO sample have been deduced after subtraction of a monotonic background.

The increased resolution now makes it possible to deduce the relative molecular fractions of the different tubes directly from both optical absorbance and peak intensity in the PLE maps as shown in Table 5.1. In practice, the relative values deduced by the two methods may differ if the individual ($n$,$m$) species have different PL efficiencies [23, 24]. In particular, it has been suggested that the $q$=+1 nanotubes have a significantly lower PL yield than the $q$=-1 tube types. Further chiral angle and diameter dependencies are also thought to exist. Limited evidence for this may be seen by comparing the relative molecular fractions deduced for the (7,6), (8,7) and (9,8) tubes from absorbance and PL. The apparent proportion of these tubes is significantly smaller when deduced from the PL intensities for either the HiPCO or CoMoCAT samples, consistent with these tubes having a much lower quantum efficiency than the other species present. A further notable observation from the absorbance and PLE maps is that the (6,5) SWNT species which is particularly prominent for the CoMoCAT sample has been almost totally removed. This can been seen from the absence of its $E_{11}$ absorption at around 1000nm and its $E_{22}$ at just below 600nm. The significance of this will be discussed later.

The almost total removal of the background is particularly striking for the CoMoCAT in PFO sample though some background is still present in the HiPCO sample. As discussed in chapter 4, the origin of this background is not certain. Although it is known to come from the graphitic $\pi$-plasmon [25], the relative contributions from carbonaceous impurities and metallic SWNTs have not been established. Nonetheless its removal could signal the absence of metallic species in the sample. Further evidence of this can be seen in the absorbance data of figure 5.4, which show clear peaks at 505 and 455 nm (corresponding to the metallic branches beginning with the (7,7) and (6,6) tubes) for the aqueous CoMoCAT dispersion, but no detectable trace of these peaks remains for the polymer/toluene sample. Removal of the metallic SWNTs from the CoMoCAT material is also evident in resonant Raman spectra at 647nm, shown in figure 5.5, which give no detectable signal from the metallic species.

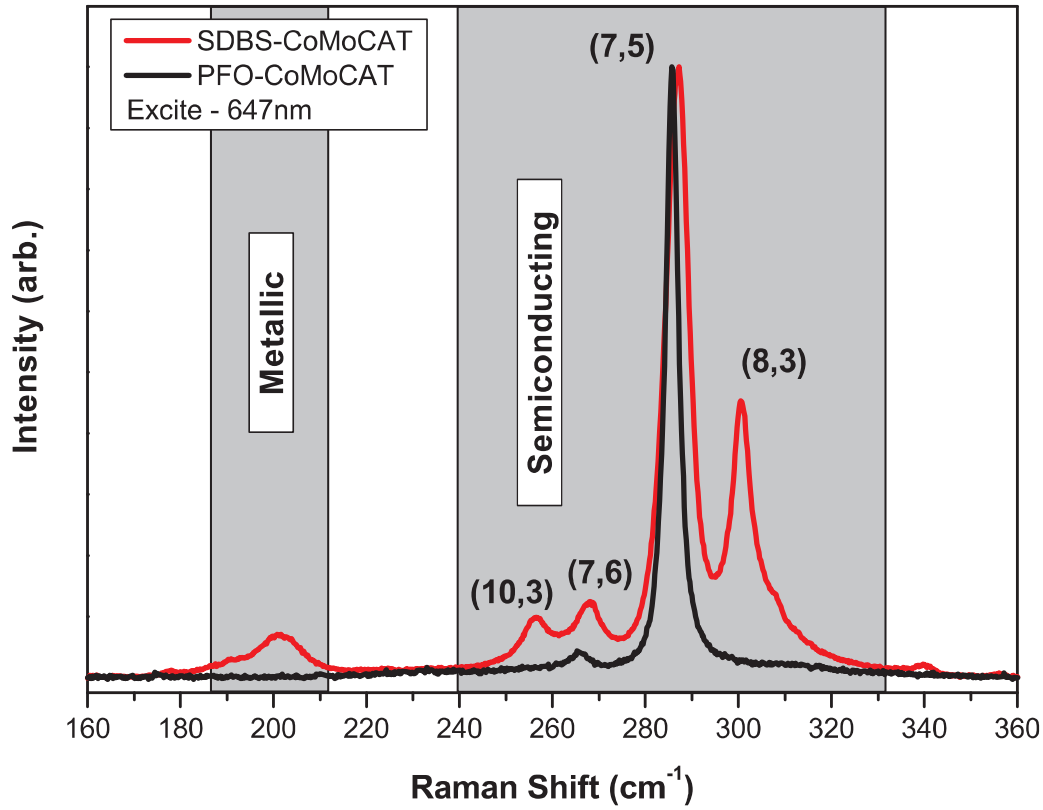


Figure 5.5: Highly resolved Raman spectra may also be obtained from PFO to solubilized SWNTs. The plot shows a comparison between the Raman spectra, taken using a 647nm light source, of surfactant wrapped CoMoCAT SWNTs (red line) and PFO wrapped SWNTs (black line), normalized with respect to the semiconducting (7,5) nanotube. This figure also emphasizes the removal of both the metallic and other semiconducting species by the PFO/toluene dispersion. The (7,5) tube peak is particularly strong here due to its $E_(22)$ resonance with the excitation wavelength.

In addition to the improvements in resolution and purity the PFO/toluene dispersions also show a significant increase in quantum efficiency. The luminescence quantum yield has been found by comparing the measured luminescence intensity and absorbance with that of a dispersion of known quantum yield. Rhodamine 6G, with a quantum efficiency of 95%, was used as our standard solution. For the SDBS suspended CoMoCAT nanotubes we find a quantum efficiency of 0.1%, consistent with previous reports [3]. However the quantum efficiency for the same CoMoCAT nanotubes suspended in PFO was found to increase to ∼1.5%. The main cause of this difference is thought to be the absence of the large non-resonant background which absorbs a significant fraction of the excitation light but does not contribute to the photoluminescence. This suggests that the previous reports of low quantum yield in nanotubes are in fact primarily a result of the parasitic absorption and not an intrinsic property of isolated nanotubes. This view is supported by measurements on isolated single nanotubes [26] where quantum efficiencies of 7% have been reported recently.

## 5.4 Discussion

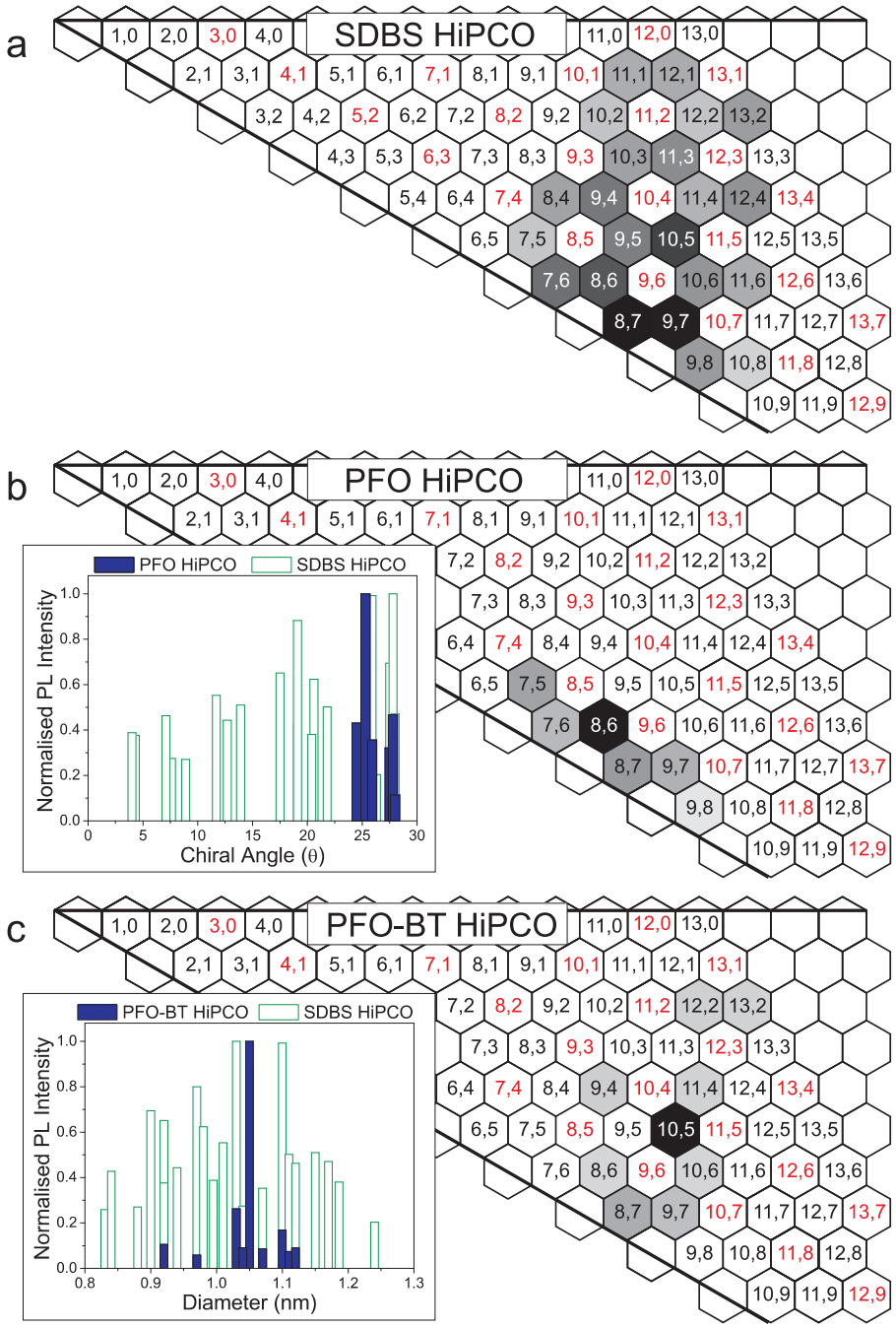


Figure 5.6: Graphene sheet maps showing normalized PL intensities for different dispersions. The hexagons correspond to the relevant $(n,m)$ metallic (red indices) and semiconducting (black indices) tube species with the darker fill shading representing higher PL intensity. a, Aqueous SDBS solubilized HiPCO. b, HiPCO solubilized using PFO in toluene. The inset histogram here shows a comparison of the PL intensities for the aqueous and polymer based suspensions as a function of chiral angle showing the strong selectivity which this polymer has for nanotubes of high chiral angle. c, HiPCO solubilized using PFO-BT in toluene. The inset histogram of the PL intensities here illustrates the strong selectivity which this polymer has for certain diameters of SWNT with respect to surfactant suspensions.

The ability of fluorene based aromatic polymers to efficiently solubilize individual SWNTs is evident from the optical spectra given here. From the PLE maps shown it is apparent that the distribution of nanotube species which are solubilized has a strong dependence on the polymer structure. For example, in going from PFO (figure 5.1A) to PFH (figure 5.1B) the polymer side-chain has been shortened and in going from PFO (figure 5.1A) to PFO-P (figure 5.1C) the backbone has been altered. Both of these small changes have a radical effect on the number of species which are solubilized and demonstrate the sensitivity of the selection process to the polymer structure.

The most remarkable selectivity is seen using the polymers PFO and PFO-BT. This is best illustrated with schematic representations called graphene sheet maps [27]. These show hexagons corresponding to the carbon nanotube species that give measurable PL shaded in a greyscale from white to black, proportional to their relative intensity. PL is used as the measure of relative species abundance as although absorbance spectra are not affected by quantum efficiencies, deconvolution of the different species is much more difficult than that from PL maps. Examples are shown in figure 5.6 for the HiPCO starting material, which has a wide initial spread (at least 22 observed) of tube species. As mentioned previously, the aqueous ionic surfactant, SDBS is thought to induce the least amount of selectivity of any dispersing agent and is therefore used in this instance as a comparison which most closely matches the distribution of species in the starting material. The dramatic selectivity of the polymer suspensions is clearly demonstrated in these maps. Only 6 species can be detected for the PFO dispersion, with a very strong chiral angle bias since all of the observed SWNTs are close to the armchair configuration. For the PFO-BT dispersion 9 species are detected with a strong selectivity for nanotubes with diameters around 1.05nm, as can be seen from the inset histogram of PL intensity. Both these selective solubilization phenomena are unprecedented to the authors' knowledge and may represent a breakthrough in the purification of SWNTs.

Using CoMoCAT SWNTs we found the same selection processes also applied. This was most relevant for the PFO/toluene suspensions due to the particular distribution of species in the starting material. Here it was found that the strong selectivity resulted in around 60% of all the suspended tubes being the (7,5) species with no trace of the formerly prominent (6,5) remaining (see figure 5.7). From the results it is clear that, in this diameter range, PFO has a very strong preference for SWNTs which have a large chiral angle. However, the total removal of the (6,5) species in the CoMoCAT sample also shows that there is not only a chiral angle selective process but also a very specific diameter

selection. This is predicted by the simulations shown in figure 5.3 when the wrapping of an additional polymer chain becomes favourable at a diameter of 0.63nm. The experimental results suggest that this onset is at 0.81nm, however the simulations do not include the presence of a solvent which is likely to alter the molecular separations and change the onset position. For larger diameter tubes it is found that an increase in selectivity occurs for diameters around 1.3nm as shown in the histogram in figure 5.3. For these larger diameters the sensitivity of the PFO to the SWNT's chiral angle is diminished. Clearly the conditions which allow the chiral angle selectivity of PFO only apply to smaller diameter nanotubes, again emphasizing the sensitivity of the wrapping process to changes in the system.

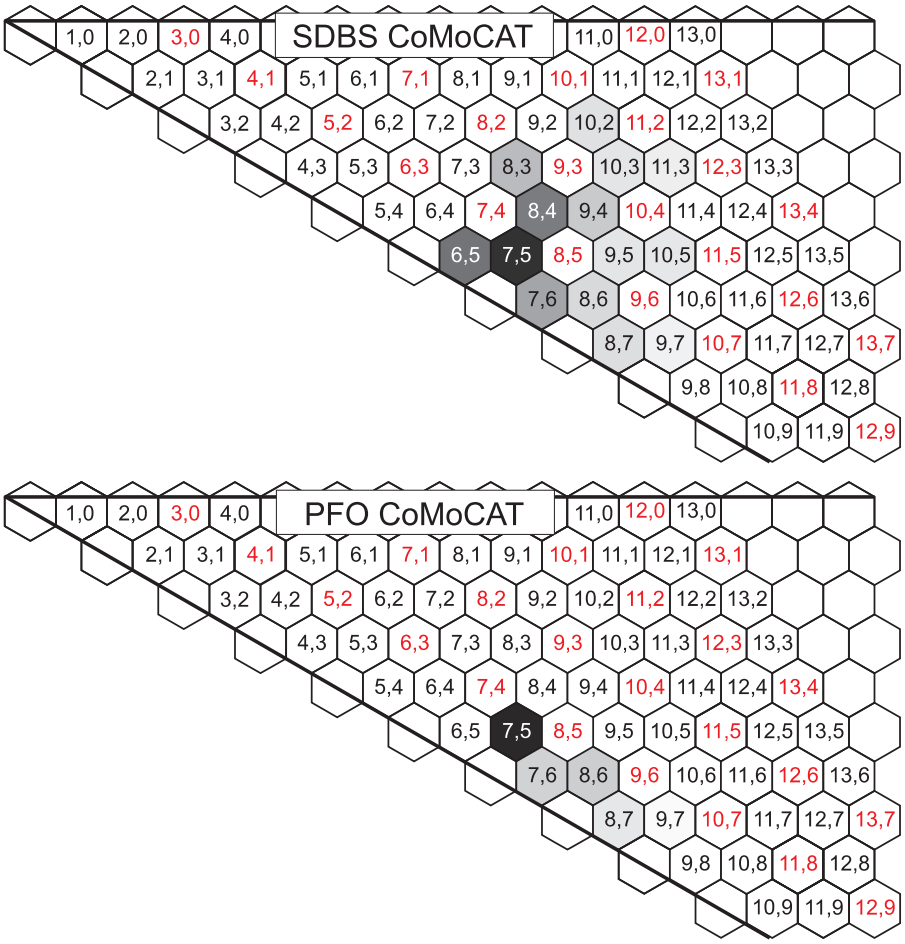


Figure 5.7: Graphene sheet maps showing normalized PL intensities for dispersions of SWNTs from the CoMoCAT processes dispersed in aqueous SDBS surfactant and PFO/toluene. The hexagons correspond to the relevant $(n,m)$ metallic (red indices) and semiconducting (black indices) tube species with the darker fill shading representing higher PL intensity.

We may conclude therefore that PFO and PFO-BT demonstrate strong diameter selectivity which we can attribute to the formation of self-assembled intermolecular structures with an n-fold symmetry. In addition to this however there is evidence of an electronic interaction between the polymers and the nanotubes, which is provided by the strong selectivity shown by some SWNT-polymer mixtures

in favour of large chiral angle tubes and the inhibition of metallic species. This suggests that the SWNT-polymer bonding is strongly influenced by both the relative orientation of the polymer chain to the nanotube structure as well as possible charge transfer which could occur from metallic tubes and lead to changes in the conformation of the polymer.

The dramatic dependence of the solubilization of the nanotubes on the details of the polymer backbone and side-chains suggest that a better understanding of the SWNT-polymer interaction could lead to custom designed polymers able to purify SWNTs down to single species with any desired chiral indices. In addition, the disappearance metallic nanotubes also suggests that polymer wrapping could be a potential route to the bulk separation of metallic from semiconducting nanotube species. The high selectivity and exceptional optical properties of these dispersions must also be appreciated in the light of the simplicity of sample preparation, a good indication of the potential which conjugated polymers have as SWNT separation agents.

# Bibliography


[1] A. Nish and R. J. Nicholas. Temperature induced restoration of fluorescence from oxidised single-walled carbon nanotubes in aqueous sodium dodecylsulfate solution. *Phys. Chem. Chem. Phys.* 8:3547–3551, 2006.

[2] O. Matarredona *et al.* Dispersion of single-walled carbon nanotubes in aqueous solutions of the anionic surfactant NaDDBS. *J. Phys. Chem. B* 107:13357–13367, 2003.

[3] M. J. O'Connell *et al.* Band gap fluorescence from individual single-walled carbon nanotubes. *Science* 297:593–596, 2002.

[4] M. S. Arnold, A. A. Green, J. F. Hulvat, S. I. Strupp and M. C. Hersam. Sorting carbon nanotubes by electronic structure using density differentiation. *Nature Nanotech* 1:60–65, 2006.

[5] S. M. Bachilo *et al.* Structure-assigned optical spectra of single-walled carbon nanotubes. *Science* 298:2361–2366, 2002.

[6] M. Zheng *et al.* DNA-assisted dispersion and separation of carbon nanotubes. *Nature Mat.* 2:338-342, 2003.

[7] M. Zheng and B. A. Diner. Solution redox chemistry of carbon nanotubes. *J. Am. Chem. Soc.* 126:15490–15494, 2004.

[8] M. J. O'Connell *et al.* Reversible water-solubilization of single-walled carbon nanotubes by polymer wrapping. *Chem. Phys. Lett.* 342:265–271, 2001.

[9] N. A. Rice, K. Soper, N. Zhou, E. Merschrod and Y. Zhao. Dispersing as-prepared single-walled carbon nanotube powders with linear conjugated polymers. *Chem. Commun.* 47:4937–4939, 2006.

[10] C. Wei. Radius and chirality dependent conformation of polymer molecule at nanotube interface. *Nano. Lett.* 6:1627–1631, 2006.

[11] J. Chen *et al.* Noncovalent engineering of carbon nanotube surfaces by rigid, functional conjugated polymers. *J. Am. Chem. Soc.* 124:9034–9035, 2002.

[12] M. Yang, V. Koutsos and M. Zaiser. Interactions between polymers and carbon nanotubes: A molecular dynamics study. *J. Phys. Chem. B* 109:10009–10014, 2005.

[13] B. McCarthy *et al.* A microscopic and spectroscopic study of interactions between carbon nanotubes and a conjugated polymer. *J. Phys. Chem. B* 106:2210–2216, 2002.

[14] P. Nikolaev *et al.* Gas-phase catalytic growth of single-walled carbon nanotubes from carbon monoxide. *Chem. Phys. Lett.* 313:91–97, 1999.

[15] S. M. Bachilo *et al.* Narrow (n,m)-distribution of single-walled carbon nanotubes grown using a solid supported catalyst. *J. Am. Chem. Soc.* 125:11186–11187, 2003.

[16] W. B. Weisman and S. M. Bachilo. Dependence of optical transition energies on structure for single-walled carbon nanotubes in aqueous suspension: An empirical Kataura plot. *Nano. Lett.* 3:1235–1238, 2003.

[17] T. Ando. Excitons in carbon nanotubes revisited: Dependence on diameter, AharonovBohm flux, and strain. *J. Phys. Soc. Jpn.* 73:3351–3363, 2004.

[18] M. Jones *et al.* Analysis of photoluminescence from solubilized single-walled carbon nanotubes. *Phys. Rev. B* 71:115426, 2005.

[19] Y. Miyauchi, M. Oba and S. Maruyama. Cross-polarized optical absorption of single-walled nanotubes by polarized photoluminescence excitation spectroscopy. *Phys. Rev. B* 74:205440, 2006.

[20] J. W. Ponder, and F. M. Richards. An efficient Newton-like method for molecular mechanics energy minimization of large molecules. *J. Comput. Chem.* 8:1016–1024, 1987.

[21] N. L. Allinger, Y. H. Yuh and J. H. Li. Molecular mechanics. The MM3 force field for hydrocarbons. 1. *J. Am. Chem. Soc.* 111:8551–8566, 1989.

[22] B. Hornbostal, M. Haluska, J. Cech, U. Dettlaff and S. Roth. Arc discharge and laser ablation synthesis of single-walled carbon nanotubes. *NATO Science Series, II. Mathematics, Physics and Chemestry* 222:1–18, 2005.

[23] S. Reich, C. Thomson, and J. Robertson. Exciton resonances quench the photoluminescence of zigzag carbon nanotubes. *Phys. Rev. Lett.* 95:077402, 2005.

[24] Y. Oyama, R. Saito, K. Satoa, J. Jianga, G. Samsonidzee, A. Grneis, Y. Miyauchi, S. Maruyama, A. Jorio, G. Dresselhaus and M. S. Dresselhaus. Photoluminescence intensity of single-wall carbon nanotubes. *Carbon* 44(5):873–879, 2006.

[25] X. Y. Huang, R. S. McLean and M. Zheng. High-resolution length sorting and purification of DNA-wrapped carbon nanotubes by size-exclusion chromatography. *Anal. Chem.* 77:6225–6228, 2005.

[26] J. Lefebvre, D. G. Austing, J. Bond and P. Finnie. Photoluminescence imaging of suspended single-walled carbon nanotubes. *Nano. Lett.* 6:1603–1608, 2006.

[27] R. B. Weisman, S. M. Bachilo and D. Tsyboulski. Fluorescence spectroscopy of single-walled carbon nanotubes in aqueous suspension. *Appl. Phys. A* 78:1111–1116, 2004.

# Chapter 6

# Charge Transfer

## 6.1 Transfer from SWNTs

Photoluminescence (PL) from freely suspended SWNTs has been observed [1], however the majority of PL studies are made with the nanotubes in dispersion suspensions. Until recently, ionic surfactants or DNA were the primary agents used to stabilize SWNTs in aqueous solvent [2, 3, 4]. It was found that as well as being sensitive to differences in suspension agents [5], the photoluminescence from SWNTs could also be reversibly quenched by increasing the acidity of an aqueous dispersion [6]. This process is thought to strip electrons from the nanotubes resulting in the tube being oxidized and causing a decrease in optical absorbance [7] and a loss of PL [8]. Initial reports showed that different nanotube species within the same sample reacted at different pH values with larger diameter tubes being the most sensitive. This oxidation process is dependent on the dispersing agent used to suspend the SWNTs. The original surfactant used by O'Connell et al. [9] was sodium dodecylsulfate (SDS), a common anionic surfactant used in many shampoos and detergents. Dispersions prepared with this surfactant were found to be extremely sensitive to oxidation and it was necessary to either de-gas the dispersions by nitrogen purging or increase their pH by adding sodium hydroxide in order to get the strongest photoluminescence signal. Therefore other surfactants began to be used [10] which make the SWNT more immune to attack from oxygen and water. Nonetheless, the aqueous SDS dispersions prove an interesting way to study the electron transfer behavior in SWNTs.

In this first section of chapter 6 it is shown that the natural oxidation of SDS coated SWNTs in water can be reversed by heating and that PL peaks corresponding to certain species are quenched upon cooling below room temperature. The results have been understood in the light of previous reports on solution redox chemistry of SWNTs [11] and are important to the development of a better understanding of the oxidation and reduction of SWNTs in aqueous solutions. They could also lead to a better understanding of the role of surfactants in SWNT suspensions, as well as giving important information about the nanotubes themselves such as whether or not the Fermi level depends on nanotube species [12]. The results illustrate that the photoluminescence is very sensitive to electron transfer, which may be crucial to the use of nanotubes as liquid-phase sensors [13].

### 6.1.1 Methods

All SWNT samples used were from the HiPCO growth process. Typically, a 0.05M aqueous sodium dodecylsulfate solution (SDS, Merck) was used to disperse the nanotube powder. Following the process pioneered by O'Connell et al. [9], the nanotube aggregates were broken up using ultrasonic agitation and purified using ultracentrifugation. The top 50% of the resulting solution was then decanted and used for further investigations. The photoluminescence studies were performed using a simple set-up consisting of optical fibres, a 30mW 633nm HeNe laser and silicon CCD detector. For longer wavelength excitation and emission a tuneable Ti:Sapphire laser and a germanium detector were used. The optical fibres were made into a bundle of six collecting fibres surrounding a central excite fibre. This was then immersed in the sample solution to give the highest signal. Control of the sample temperature was achieved by surrounding a quartz cuvette with thermoelectric coolers. Controlling the bias and voltage allowed the sample to be cooled to below 5°C or heated to above 60°C, as measured by a thermocouple attached to the fibre bundle. The photoluminescence intensity was monitored after each temperature change to ensure that the solution was at equilibrium before a final recording was made. A control experiment was done to confirm the role of dissolved gases in the observed phenomenon. This involved purging the solution with nitrogen gas at room temperature and noting its effect on the overall PL emission intensity.

### 6.1.2 Results and Analysis

The photoluminescence intensity as a function of temperature for the tube species seen in the range of the CCD detector is shown in figure 6.1. The sample was initially cooled then measurements taken as the temperature was raised slowly. It is interesting to note the dramatic changes in intensity which occur very close to room temperature. This could be of considerable significance to experiments using sodium dodecylsulfate as a dispersing agent where variations in sample temperature as small as $\pm 1$°C may give large changes not only in overall intensity but also relative peak intensity.

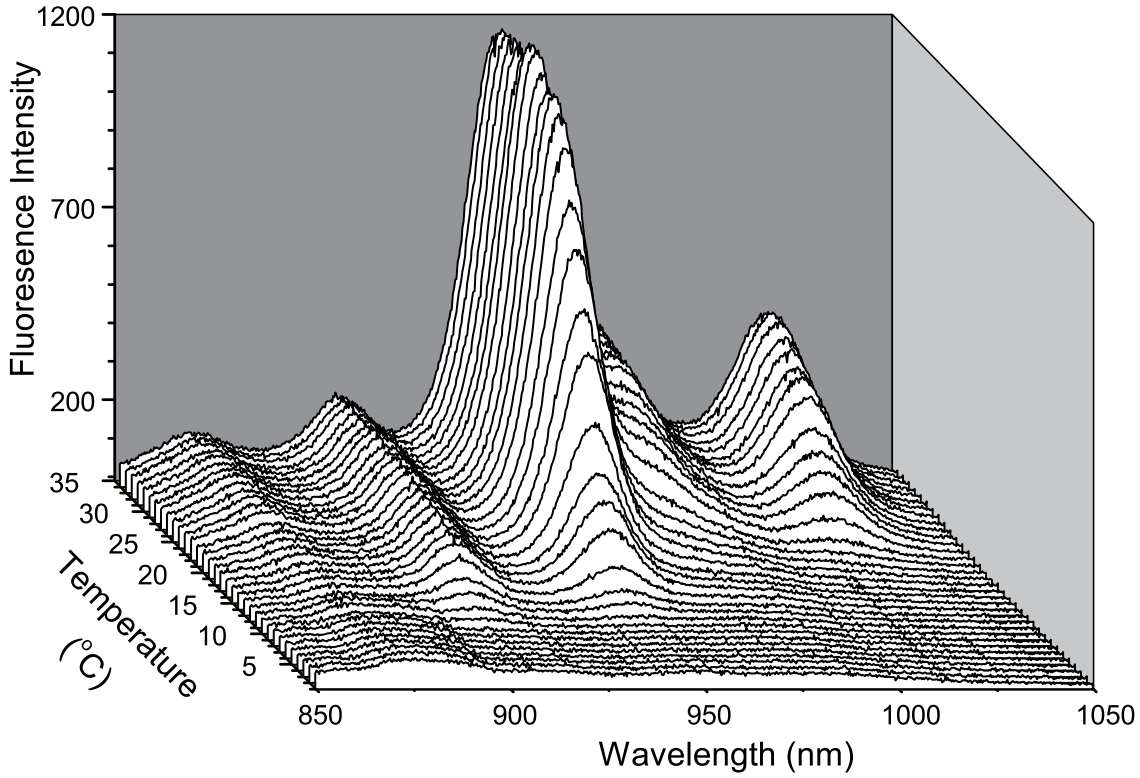


Figure 6.1: Intensity of SWNT-SDS photoluminescence in the temperature range $1 - 35°C$.

The peak emission intensity of the SWNTs as a function of temperature for the small diameter semiconducting tubes present in HiPCO material is shown in figure 6.2. Sigmoidal curve fitting to the data yields a common trend underlying the increase in PL intensity as the sample is heated. The shape of the curve is similar in every case though its position is dependent on the tube species. The temperature at midpoint of the curve, the photoluminescence restoration midpoint, is taken as the characteristic parameter in studying the overall dependency.

The oxidation of materials by water and oxygen is a well understood phenomenon in electrochemistry due to its importance in prevention of corrosion. The reduction half reaction which drives general water oxidation processes is

$$O_2 + 4H^+ + 4e^- \Longleftrightarrow 2H_2O. \tag{6.1}$$

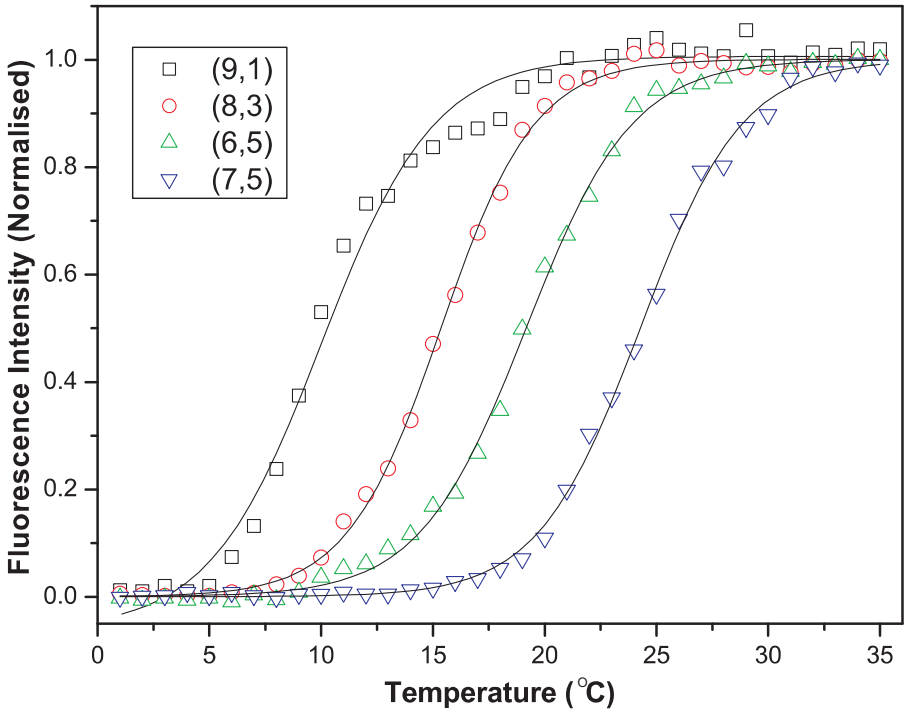


Figure 6.2: Normalised photoluminescence intensity vs temperature for peaks seen in figure 6.1. The points show experimental data and the lines indicate sigmoidal curve fits from which the point of inflection has been taken as the PL restoration midpoint. The (n,m) indices in the box refer to different chiral species of SWNT with distinct diameters and bandgaps.

It can be seen from equation 6.1 that the combination of dissolved oxygen and protons has the ability to remove 4 electrons per $O_2$ molecule. Whether or not an electron will be removed from a particular material depends on its potential energy relative to that of the $O_2$, $H^+/H_2O$ redox couple. Electrochemists have established values for standard redox potentials of various systems and quote these by referencing to a 'normal hydrogen electrode'. It is then possible to use the Nernst equation to estimate the reduction potential for the reaction in equation 6.1 for the concentrations and temperatures of the experiment

$$E_{water} = E_0 - \frac{RT}{nF} lnQ. \tag{6.2}$$

Here $E_0$ is the standard reduction potential for the reaction in equation 6.1, $R$ is the gas constant, $T$ is absolute temperature, $n$ is number of electrons transferred, $F$ is the Faraday constant and $Q$ is the reaction quotient.

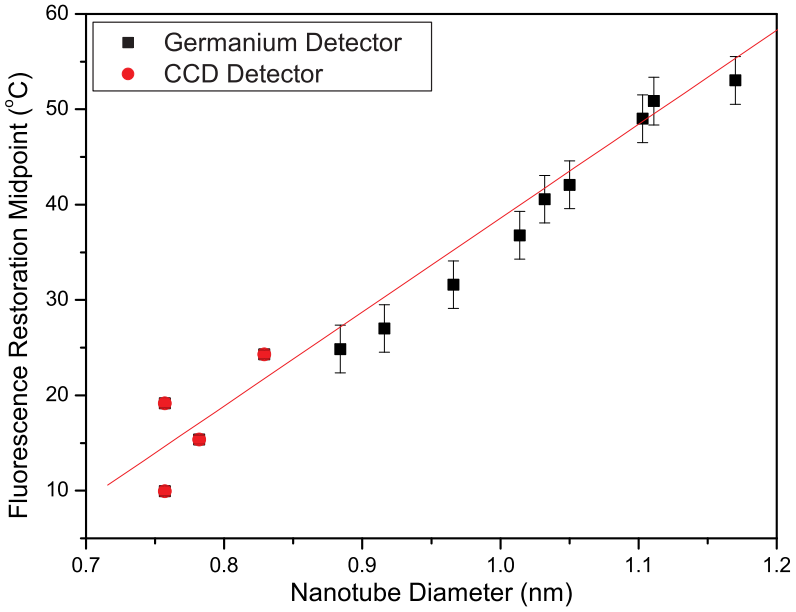


Figure 6.3: The midpoint of the photoluminescence restoration is strongly dependent on nanotube species with PL being restored in larger diameter SWNTs at higher temperatures than for small diameter tubes.

The reaction quotient may be expressed in terms of the molar concentrations as shown below

$$Q = \left( \frac{[H_2O]^2}{[H^+]^4[O_2]} \right). \tag{6.3}$$

The next question is what is the potential energy of the electrons in the SWNTs? Although the bandgap of different SWNT species is easily found from PL data, the absolute positions of the valence or conduction band edges are unknown. They are vitally important in the context of electron transfer between any semiconductor and aqueous redox species since these are the energy levels involved in transfer. In physics the Fermi level is used as the reference point for defining the band edges and this may in turn be referenced to the vacuum level, giving the work function for a material. However, as just stated, in electrochemical literature it is common to use standard redox potentials as a measure of electron affinity (analogous to conduction band edge) or ionisation potential (analogous to valence band edge). A conversion between the two conventions is possible using

$$E_{(NHE)} = E_{(WF)} - 4.52eV \tag{6.4}$$

where $E_{(NHE)}$ is the standard redox potential and $E_{(WF)}$ is the potential on the work function scale.

The value 4.52eV is the binding energy of a hydrogen molecule. The work function for SWNTs can be approximated as being that of graphene, taken to be 4.66eV [15]. Using equation 6.4 this makes it possible to approximate the reduction potential (valence band edge) of the SWNTs from

$$E_{(SWNT)} = \left(4.66 + 0.5E_g\right) - 4.52 \tag{6.5}$$

where $E_g$ is the bandgap of a particular SWNT. Unlike in previous experimental work [16] the Fermi level is assumed to be constant for all nanotubes. Using equation 6.5 the reduction potential for the range of SWNTs investigated here is predicted to vary between $+0.82V$ for a small diameter (9,1) tube to $+0.58V$ for a larger diameter (9,8) tube. This simplified approach gives a reduction potential for SWNTs which is remarkably close to the standard potential for the reduction half reaction of $H^+$ (in the presence of dissolved $O_2$ at 25°C) of $+0.71V$. More interestingly, if equation 6.5 is used to calculate the standard potential for the (6,5) SWNT a value of $0.78V$ is found. This corresponds very well with the value of $0.80V$ found experimentally by Zheng and Diner [11] using DNA wrapped SWNTs and redox titration. From figure 6.4 (part a) it can be seen how the distinct chemical nature of the different nanotube species in the sample comes into play and helps to explain the roughly linear relationship (part b) between the photoluminescence restoration temperature and SWNT bandgap. As the temperature is increased there is a reversal of the reaction (equation 6.1) at the point where the $O_2$, $H^+/H_2O$ reduction potential moves above the valence band edge for a particular SWNT. This causes a refilling of the valence band with the resultant restoration of PL as is observed. The broadening of the transition and the sigmoidal shape of the curve show a behavior consistent with the chemical potential controlling a Fermi distribution function.

To explain the source of the decrease in $O_2$, $H^+/H_2O$ reduction potential it is necessary to consider the Nernst equation. This shows not only that an increase in temperature will directly decrease the reduction potential but also that it will be sensitive to any change in the concentration of $H^+$ and $O_2$. The solubility of dissolved gases in aqueous solution is known to be strongly temperature dependent and has been well studied due to its importance in many systems including aquaculture and corrosion [17]. Typically in pure water or saline solution the oxygen concentration will decrease by a factor of three upon heating from 5°C to 60°C. Dissolved carbon dioxide is also important since it affects the pH. Thus a sodium dodecylsulfate solution at equilibrium with air was found to have a pH of 6.0 at room temperature and pH of 7.0 after heating. Using literature values [17] for the concentration

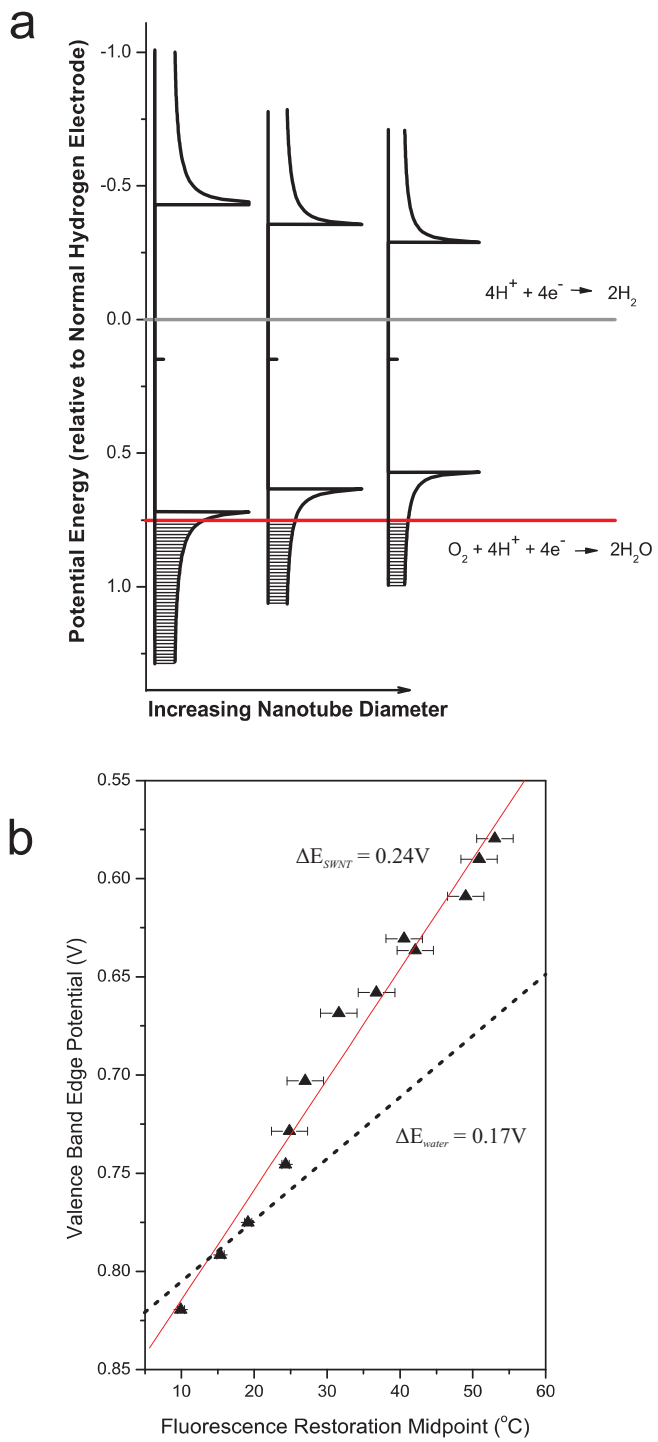


Figure 6.4: (a) Schematic diagram of semiconducting SWNT energy states close to the band-gap. The reduction potential (valence band edge) for SWNTs is expected to decrease relative to the NHE for increasing nanotube diameter. The position of the $O_2$, $H^+/H_2O$ reduction potential will also decrease with increasing temperature thus restoring PL to different SWNT species as the solution is heated. (b) The photoluminescence restoration midpoint is shown to vary linearly with the calculated valence band edge, $E_{SWNT}$. This may be compared with the variation in the reduction potential for water ($\Delta E_{water}$) over the same temperature range.

of oxygen[†] and pH values for the $H^+$ concentration yields a value for $E_{water}$ of $+0.82V$ at 5°C and $+0.65V$ at 60°C ($\Delta E_{water} = 0.17V$). Equation 6.5 allows us to calculate the valence band edges for the SWNT species studied. These are plotted in figure 6.4b against the PL restoration midpoint. The results show the spread in values for the valence band edge ($\Delta E_{SWNT} = 0.24V$) to be significantly greater than the predicted temperature induced change in the reduction potential for water.

However it is possible that the SWNTs possess a large amount of physisorbed $O_2$ even in solution. This would result in a higher local concentration of oxygen than has just been assumed. Upon increasing the temperature the oxygen would desorb and be removed from the solution with the effect of restoring PL. Thus a high concentration of physisorbed oxygen would play an important role, as its removal would augment the natural temperature dependent change in reduction potential. Indeed a hysteresis has been observed in the temperature dependence of the PL intensity suggesting that the re-quenching is kinetically limited by the adsorbance of oxygen.

The effect of temperature on the $H^+$ concentration is hard to quantify. Apart from being strongly influenced by the amount of dissolved $CO_2$, the effective $H^+$ concentration is also thought to be affected by the charged surfactant layer. This is something which will be sensitive to temperature through the degree of ionic dissociation though it is not yet known how this may effect redox reactions for SWNTs in aqueous surfactants. Tests done with other surfactant solutions [18] did not yield any similar temperature dependence. This is thought to be due to the fact that other surfactants have higher natural pH values than the SDS solutions and thus oxidation of the SWNTs does not occur.

The results of the control experiment where the SDS-SWNT solutions were purged with $N_2$ at room temperature showed a similar increase in emission intensity. This gives further credibility to the theory outlined here and emphasizes the effect which the dissolved gases have on SWNT photoluminescence in this system.

[†]12 mg/L at 5°C and 4.55 mg/L at 60°C.

### 6.1.3 Discussion

Photoluminescence intensity from SWNTs dispersed in aqueous sodium dodecylsulfate has been shown to be temperature dependent. This has been interpreted as being a reversible redox reaction where the decrease in dissolved $O_2$ and $CO_2$ and increase in temperature diminish the oxidising strength of the $O_2$, $H^+/H_2O$ couple. Although it is certain that this process is highly complex due to the convolution of several influential factors, it has been found that by invoking the Nernst equation and some simple assumptions we can explain the observed behavior. At low temperatures the oxygen combines with $H^+$ in the water to remove an electron from the valence band of the SWNT causing the loss of photoluminescence. By increasing the temperature dissolved gases are removed with the result that the redox reaction is reversed causing reduction of the SWNT and restoration of photoluminescence. The temperature at which the photoluminescence is restored was different for individual SWNT species whereby photoluminescence returned to smaller diameter nanotubes first with larger diameter tubes being restored at higher temperatures. This trend was approximately linear with the SWNT bandgap and consistent with previous reports of bandgap selective redox reactions with carbon nanotubes [19]. The origin of this linear behavior has been discussed and is thought to be due to the different tube species having distinct reduction potentials owing to the relative positions of their valence band edges.

The results shown here emphasise that SDS is a poor choice of surfactant for solution phase characterisation of SWNTs using photoluminescence spectroscopy. Its use could lead to misleading results due to the fact that larger diameter nanotubes may be in an oxidised non-fluorescing state whilst smaller diameter tubes show strong emission. The control of dissolved $O_2$ concentration may lead to an accurate determination of reduction potentials for individual SWNT species since the point of reversal of the redox reaction seen in this study is well defined. Ultimately this would require a more accurate knowledge of the reduction potential of the $O_2$, $H^+/H_2O$ redox couple than could be established here. Using dissolved oxygen as the variable oxidising agent would be preferable to addition of standard chemical oxidising reagents since these could be expected to react with the surfactant making accurate calculations difficult. The solution redox chemistry of SWNTs promises to be an area of much future interest due to possible applications in catalysis and sensors.

## 6.2 Transfer to SWNTs

Whilst aqueous-surfactant solutions are shown to remove electrons from SWNTs, their organic solvent-polymer equivalents (which were described in the previous chapter) are found to donate charge carriers when photo-excited. This work is of major importance to research into using SWNTs and organic polymers in photovoltaic applications.

Organic conjugated polymers have been proposed as promising alternatives to existing solar cell technology due to their low cost and versatility. Photo-voltaics based on conjugated polymers are flexible, robust and lightweight and may potentially be embedded into other materials such as fabrics or applied to surfaces as coatings. The current drawback with organic photovoltaic cells is their low efficiency at converting light into electricity. Whilst commercial silicon solar cells can achieve between 13-16% energy conversion [20], organic PV cells are frequently quoted as having efficiencies an order of magnitude lower [21]. Nonetheless the possibility of manufacturing cheap, large area cells and their potential versatility make organic PVs an attractive material for future energy needs. One major challenge in improving organic PVs arises from the excitonic nature of the photo-excited carriers in these materials. Whilst excitons in inorganic semiconductors typically have binding energies of ∼4-15meV [22], allowing thermal dissociation at room temperature, organic polymers such as PPV and its derivatives may have binding energies of over 400meV [23]. Thus it is necessary to choose electrode materials with work functions that are sufficiently offset from the polymer's HOMO and LUMO levels to make it energetically favorable for the electron-hole pair to dissociate. A further issue with polymer photovoltaics is the low carrier mobilities. To reduce the possibility of the electrons and holes recombining before reaching their electrodes, thin films of polymer can be used. However, since the diffusion length of excitons in conjugated polymers is in the range 5-15nm [24], alternative approaches to overcome both these problems have been sought.

Blending additives into the conjugated polymers has been found to be a successful way of improving device efficiency. This approach often relies on adding a material such as another polymer [25] or inorganic nanoparticles [26] which have a higher electron affinity than the bulk conjugated polymer itself. In the presence of the potential junction between the phases, the exciton is split by electron transfer to the acceptor material. The electron may then be transported via a percolation network or

otherwise to its electrode whilst the hole may be transported through the donor polymer phase. To date the most efficient organic photovoltaic devices, with efficiencies of up to 5%, have been produced by blending a functionalized form of $C_{60}$ (PCBM) with polymer [27]. Single walled carbon nanotubes (SWNTs) have also been blended with conjugated polymers with the aim of providing heterojunctions for the excitons to dissociate at [28]. An advantage of SWNTs is that their defect free molecular wire type structure should provide excellent channels for the electrons to be transported efficiently through the material [29]. Previous researchers have used SWNTs as electron acceptors in polymeric photo-voltaics and shown promising results [30]. Despite the predicted advantages of using SWNTs as an electron acceptor and transport phase, it has so far not been possible to produce a photovoltaic cell with efficiencies approaching that of other composites, such as those using PCBMs for example.

In this second section of chapter 6 we give direct evidence using photoluminescence excitation mapping that energy is transferred from the semiconducting aromatic polymers, poly[2-methoxy-5-(2'-ethyl-hexyloxy)-1,4-phenylene vinylene] (MEHPPV) and poly(9,9-dioctylfluorenyl-2,7-diyl) (PFO), to SWNTs when the polymers are excited across their minimum energy gaps. The energy transfer is seen to occur both in solution and in drop cast films. This work could lead to a better understanding of the energy transfer process in polymer-nanotube composites and to a realization of the full potential of these materials in photovoltaic devices.

### 6.2.1 Methods

Samples were prepared in a similar manner to those which were described in chapter 5 and as given by Kazaoui et al. [31]. All SWNTs were from the HiPCO process [14]. MEHPPV (Sigma Aldrich) and PFO (American Dye Source) were dissolved in toluene with SWNTs in the ratio 5mg SWNT: 6mg polymer: 10ml solvent then sonicated and centrifuged as before. Film samples were prepared by drop casting the solution onto Spectrosil substrates.

Photoluminescence-Excitation (PLE) mapping was done as in chapter 5 with a home built automated excitation system and liquid nitrogen cooled InGaAs photodiode array. For measurement of the luminescence from the polymer this detector was substituted for a thermoelectrically cooled silicon CCD system. Optical absorbance studies were performed using the Perkin-Elmer photospectrometer.

### 6.2.2 Results and Analysis

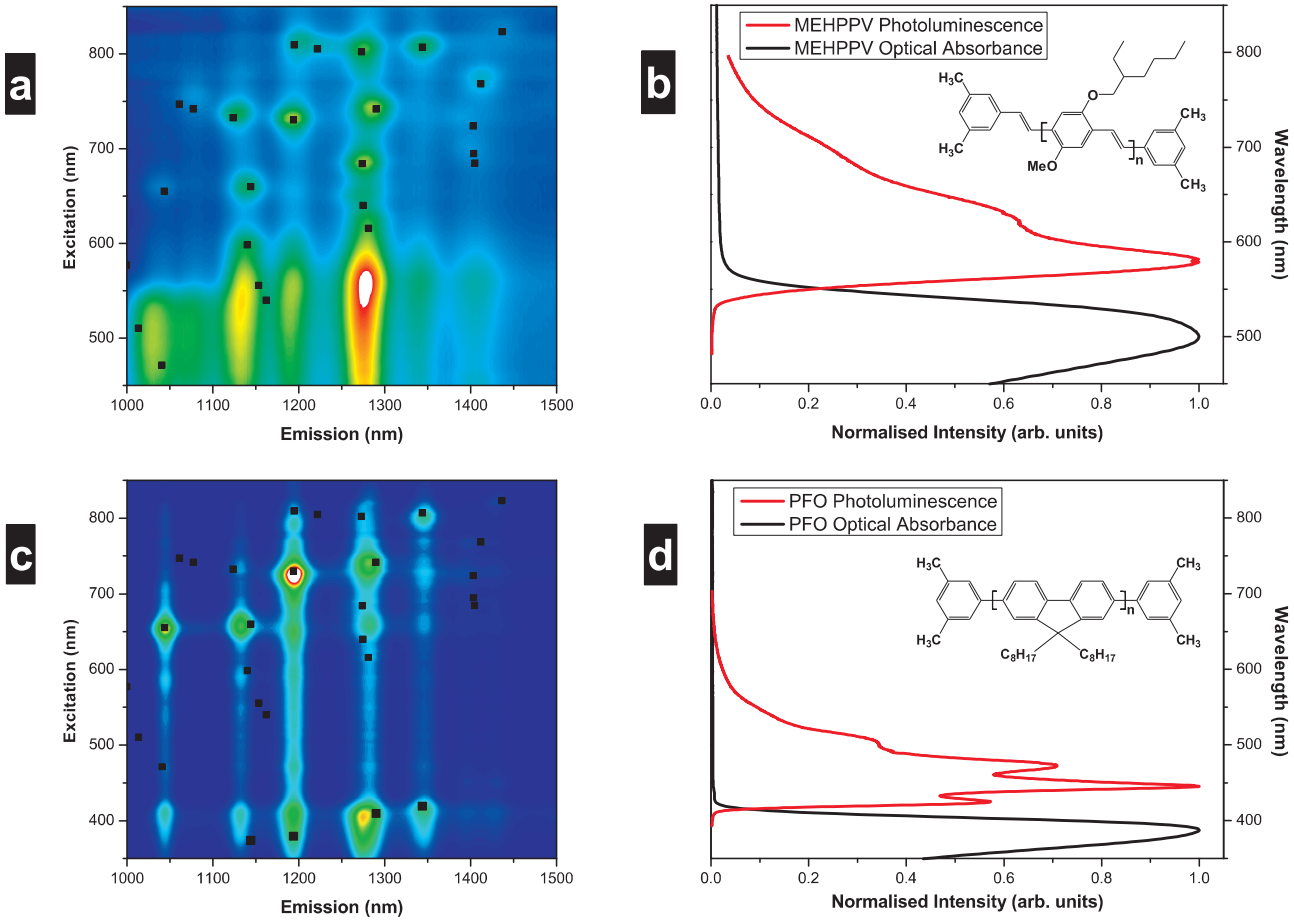


Figure 6.5: The colour-plots show photoluminescence intensity from SWNTs (HiPCO) in solutions of MEHPPV (a) and PFO (c) as a function of emission and excitation wavelengths. The black squares indicate the expected peak positions for all possible nanotube structures in this spectral range. The solutions used in (a) and (c) were prepared using 40min and 15min sonication time respectively. The adjacent graphs show the optical absorbance and emission from the bare MEHPPV and PFO polymers in toluene.

The capacity of semiconducting polymers to transfer energy to SWNTs is likely to be linked to their ability to solubilize the nanotubes. We have studied a variety of organic polymers in organic solvents and have found a very strong dependence of the solubility of the SWNTs on the polymer structure. The degree of solubilization was studied by observing the intensity of the SWNT features in both optical absorbance and photoluminescence spectra. Two of the more common semiconducting polymers, MEHPPV and PFO, were found to work remarkably well at dispersing SWNTs using toluene as solvent. Notable differences were, however, found in the fractional concentrations of the nanotubes species which were solubilized by different polymers, allowing this process to be used to produce highly selected solutions of nanotubes [32]. This shows that the solubilization process is very sensitive not only to the polymer structure but also to the structure of the individual SWNTs themselves.

In order to investigate the energy and/or charge transfer from polymer to nanotubes we have studied photoluminescence-excitation (PLE) maps of their solution dispersions and dried films. Examples of these spectra are shown in figures 6.5a and 6.5c for SWNTs produced by the HiPCO process dispersed in toluene solutions of MEHPPV and PFO. The emission spectra are normalized to constant excitation photon flux. The upper sections of the plots show the features present in a standard PLE map of SWNTs [33], allowing the contributions of individual nanotube species to be identified. These peaks correspond to the resonantly enhanced emission from the SWNTs' primary $E_{11}$ electronic transitions when the excitation matches their secondary $E_{22}$ electronic levels. The PFO solution shows emission from a much smaller number of nanotube species due to the selective solubilization referred to above. A small shift ($\sim$1.3% redshift) is seen when compared to previous luminescence data taken using samples prepared with aqueous surfactants [34]. This shift is similar for all nanotube species and does not have any chiral angle dependence. We therefore attribute this to a change in the local dielectric environment where the increased dielectric screening causes a reduction of the electron-electron and excitonic Coulomb interactions which produce a net reduction in the energy gap [35].

The lower section of the PLE maps show luminescence from the same SWNTs but in this case with excitation at shorter wavelengths. In the case of the MEHPPV-SWNT solution (figure 6.5a) it can be seen that emission occurs from all of the nanotube species present when excitation wavelengths in the regime 450-550nm are used. This spectral range does not correspond to any electronic transitions in the nanotubes. The position and excitation profile of the emission does, however, closely match the optical absorbance of the polymer as shown in figure 6.5b. This is clear evidence that the photoexcited MEHPPV polymer is transferring energy to the SWNT, resulting in the creation of an electron-hole pair which then recombines at the nanotube's bandgap. For the case of PFO, the PFO-SWNT PLE map (figure 6.5c) again shows the same broad excitation profile for all nanotubes present for wavelengths shorter than 420nm, corresponding to the much shorter wavelength of the polymer absorption (figure 6.5d). In this case the polymer absorbance lies close, as shown, to the $3^{rd}$ order nanotube energy levels, however, since the excitation profile is also independent of nanotube diameter, it seems likely that the energy transfer is also taking place from this polymer to the nanotubes and not via direct excitation. Comparison of the nanotube emission intensities when pumped via the polymer against the emission when pumped directly into the nanotubes, suggests that absorption into the polymer can have up to twice the collection efficiency of direct absorption.

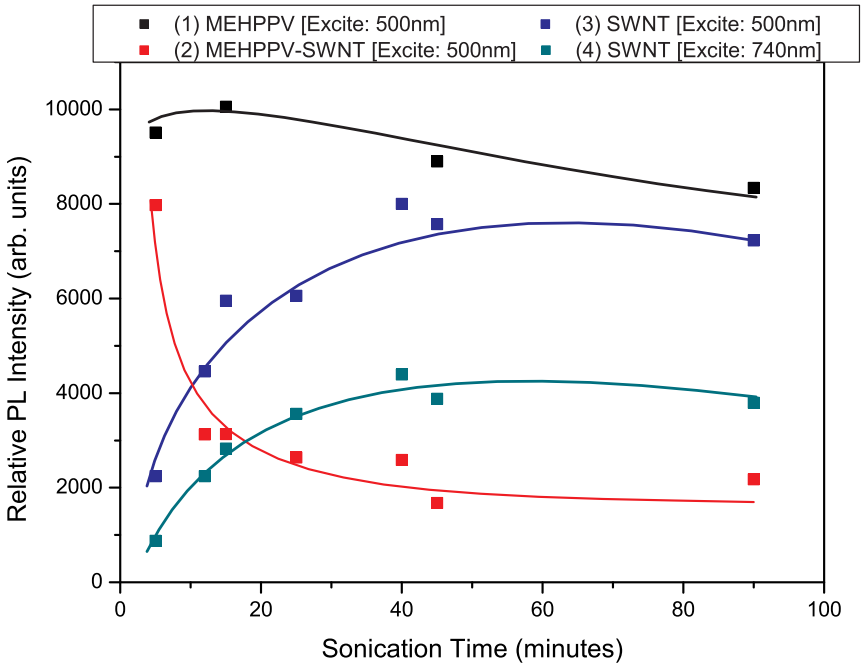


Figure 6.6: The dependence of the PL emission intensity from solutions of MEHPPV and MEHPPV-SWNT as a function of sonication time used for preparation of the solutions. (1) Polymer PL measured at 1000nm from pure MEHPPV solutions excited using 500nm light. (2) Polymer PL measured at 1000nm for MEHPPV-SWNT solutions excited using 500nm light. (3) SWNT PL measured at 1280nm for MEHPPV-SWNT solutions excited through the polymer using 500nm light. (4) SWNT PL measured at 1280nm for MEHPPV-SWNT solutions excited directly into the nanotubes using 740nm light.

We investigate the charge transport processes taking place in the composite by studying the relative emission intensities as a function of the sonication time used in the sample processing. The sonication has two effects: Firstly, it acts to debundle the nanotubes, causing an increase in the solubilisation of isolated polymer wrapped tubes and a resultant increase in the nanotube PL. Secondly, it is thought that the sonication will also shorten both the polymer and nanotubes to some extent. Figure 6.6 shows how the PL emission varies for both a polymer solution alone (MEHPPV) and the nanotube/MEHPPV composite as a function of sonication time. The PL intensity from the polymer is measured in its emission tail at 1000nm when excited at a wavelength of 500nm (the peak of the polymer absorption). PL intensity from the strongest nanotube emission at 1280nm is measured for both excitation via the polymer absorption at 500nm and by direct absorption at 740nm. Emission from the polymer solution is only weakly dependent on sonication, with a small initial increase probably caused by an increase in polymer solubility, followed by a small ($\sim 15\%$) decrease caused by cutting of the polymer. In a separate study we have shown that both the intensity and the spectra of the visible polymer

emission are independent of sonication time. By contrast, the polymer emission in the composite shows a very rapid and dramatic (over 4-fold) decrease in intensity as the sonication time increases, falling to a minimum once the nanotubes are fully dispersed. The nanotube emission increases very significantly for both direct excitation and excitation via the polymer. The intensity of both processes increases by a similar amount, with an approximately four-fold increase matching the fall seen in the polymer emission. The increase in the direct excitation peak tells us that the change is due to the increase in the density of isolated single wall tubes, while the clear inverse correlation of the changes in the polymer and nanotube emissions when excitation is into the polymer provides direct evidence for the high probability (of order 75%) of charge/energy transfer from the polymer to the nanotubes. The increase in the transfer rate is attributed to the increase in the density and homogeneity of the distribution of the isolated nanotubes.

We have also prepared drop cast films of both solutions and tested them using PLE mapping. As shown in figure 6.7 these solid state samples show a similar energy transfer effect to that found for the solutions although the SWNT emission intensity was significantly less both when the nanotubes were excited directly across their secondary energy gap, $E_{22}$, as well as when excited via the polymer. The position of the peak PL is slightly shifted to around 580nm. This is thought to be partly due to over-absorption in the polymer layer and partly to the intrinsic shift in the polymer absorption maximum in the dried state [36]. The enhanced relative emission from the polymer, compared to the nanotubes in the long wavelength region is due to the enhanced emission from the polymer tail which is observed in the solid state. We can nevertheless conclude that the same mechanism of energy transfer from polymer to nanotube, which is seen to take place in the solutions, must also occur in the solid films.

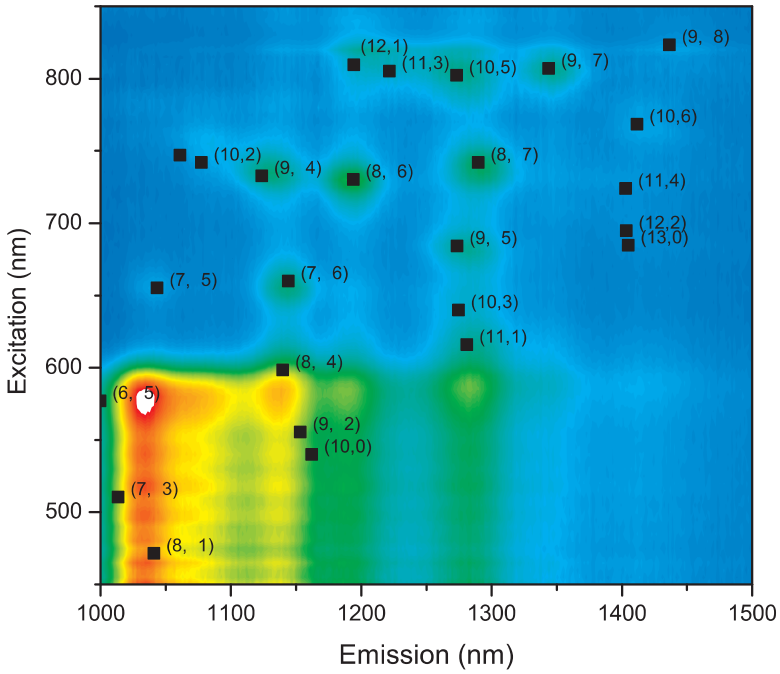


Figure 6.7: A false colour-plot of photoluminescence intensity from a drop cast film of SWNTs made from a solution of MEHPPV in toluene. The black squares indicate the theoretical peak positions for all possible nanotube structures in this spectral range. The numbers in brackets correspond to the (n, m) index of each distinct nanotube structure.

The PLE maps, shown in figure 6.5, give strong evidence for the photo-induced transfer of energy from organic polymers to SWNTs in these samples. Similar results have been shown by Yanagi et al. [37] for the case of carbon nanotubes filled with an organic dye. This dye was found to be selectively encapsulated inside SWNTs with a minimum diameter threshold of around 1.3nm. PLE mapping was also used to show that emission from the nanotubes occurred when the dye was resonantly excited. Since the organic dye used in their work is similar in nature to the organic polymer which we have used here, it is quite probable that the mechanism of energy transfer in both systems will be the same.

Figure 6.8 shows an energy level scheme for the polymer-nanotube composites. The ionisation energies (HOMO) and electron affinities (LUMO) for MEHPPV [38] and PFO [39] have been taken from values found in the literature and their separation corresponds to the energy of the lowest optically active singlet exciton. The SWNT levels are based on a workfunction of -4.66eV [15] and empirically determined energy gaps. It has been suggested by some workers that the workfunction value is diameter dependent but this is not certain [16, 40, 12, 41] and so for the purposes of this schematic it has been assumed to be constant for all tubes. The position of the chemical potential has been omitted as it is also an uncertainty in this system.

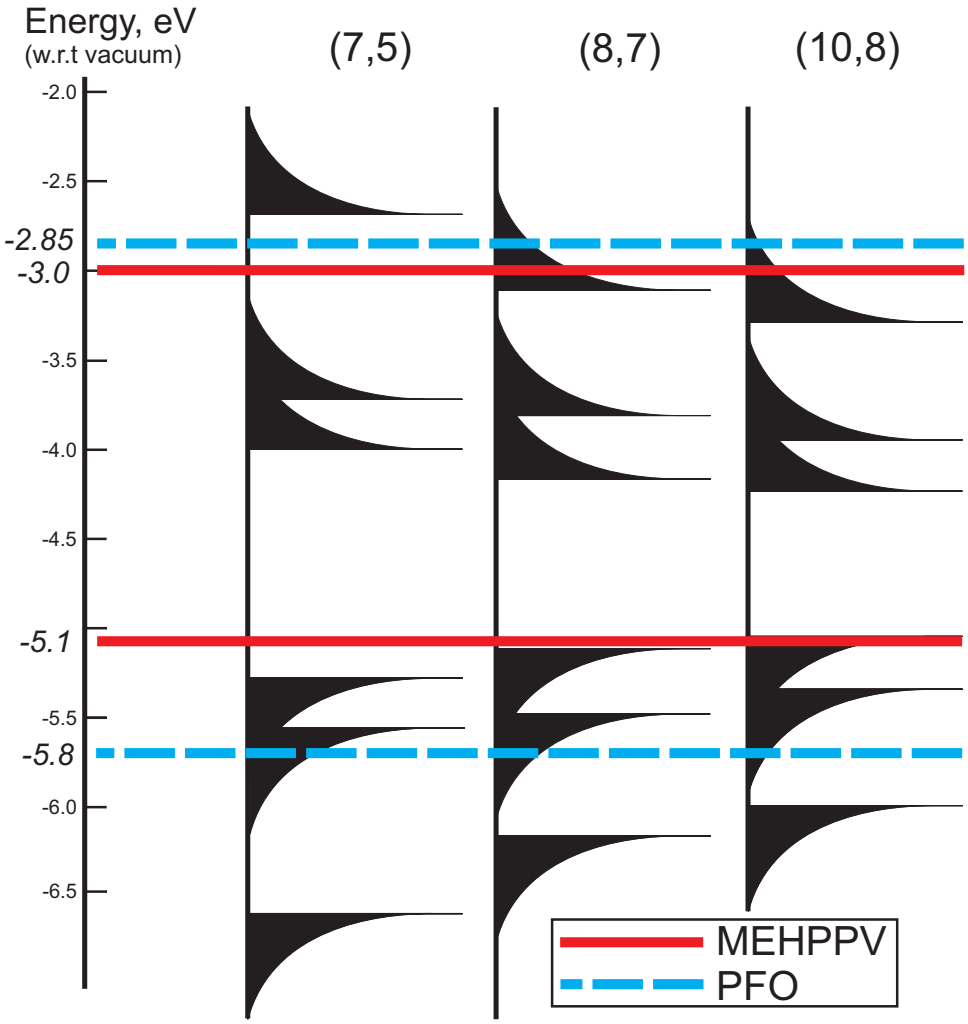


Figure 6.8: Illustrative density of states scheme for three nanotube species: (7,5), (8,7) & (10,8). The coloured lines indicate the possible overlap between the polymers' (MEHPPV and PFO) HOMO and LUMO levels with the nanotubes' $1^{st}$, $2^{nd}$ and $3^{rd}$ order energy levels, where the scale is given with respect to the vacuum level.

Several possible mechanisms exist for the energy transfer from polymer to SWNT. It has been proposed that the addition of nanotubes to polymer semiconductors might allow them to act as electron acceptors [28, 31], facilitating charge separation and electron transport. Our observation of high levels of photoluminescence from the SWNTs casts some doubt on this hypothesis, since we must assume that significant densities of both electrons and holes are present in the tube for recombination to occur. Another possible process would be Förster resonance energy transfer (FRET) [42]. This is a mechanism of energy transfer which happens between molecules that have a spectral overlap of emission and absorption and which is strongly enhanced by the spatial proximity of the two components due to the interaction between the transition dipole moments of the donor and acceptor molecules. It has recently been suggested [43] that such a process could be responsible for the energy transfer in polymer/PCBM photovoltaic cells. The data in figure 6.5 shows that this is rather unlikely in the present case, since the overlap between polymer emission and the absorption in the nanotube $E_{22}$ levels is strongly wavelength dependent for both polymers. In particular, the PFO has almost no emission below 600nm, thus precluding the possibility of any Förster transfer. The most probable explanation is that direct exciton transfer is taking place, as figure 6.8 shows that there is a large energy difference in the electron energy levels and almost no barrier to hole transfer. Since the exciton binding energy in polymers is of the order of 0.4eV [23], it is unlikely that the electrons and holes can be separated easily and thus direct exciton transport will take place into the nanotubes. This is contrary to the current proposed role of SWNTs in organic photo-voltaics where the holes remain in the polymer phase, although it should be remembered that the additional electric fields present in such devices will contribute significantly to electron-hole separation.

An alternative possibility is that recombination may be the result of electron separation combined with a strong p-type doping of the SWNTs. In this case, however, it has been shown that there is usually a strong dependence of the PL intensity on tube species [44], since the different SWNT species will be differently doped by a chemical potential fixed in the p-type polymers [38]. A further complication is that electron transfer would lead to the build up of space charge, leading to hole transport into the nanotubes and making the comparison of different measurement situations more difficult. The exciton transport picture is also supported by the quenching of the polymer PL by the nanotubes, since if this occurred due to electron transfer alone it would again lead to species specific enhancement of the nanotube PL. Recent data from MEHPPV light emitting diodes, where the addition of SWNTs produces a significant decrease in the light output [45] is also suggestive of exciton transport.

### 6.2.3 Summary

It has been demonstrated that energy transfer occurs between semiconducting organic polymers and single-walled carbon nanotubes when the polymer is photo-excited. This has been shown by recording the near-IR luminescence intensity from the nanotubes as a function of excitation wavelength. Well defined emission peaks in this region are unambiguously correlated to known SWNT species by way of comparison with previous semi-empirical theory work. The luminescence from SWNTs when excited across the polymer's optical absorbing peak is a significant observation. It verifies that energy is transferred from the polymer to the nanotube in these composites but does not necessarily concur with previous reports that the nanotubes simply act as electron acceptors. The results raise interesting questions about the potential benefits of using SWNTs to split excitons in the polymer photovoltaic devices.

# Bibliography


[1] J. Lefebvre, J. M. Fraser, P. Finnie and Y. Homma. Photoluminescence from an individual single-walled carbon nanotube. *Phys. Rev. B*, 69:075403, 2004.

[2] V. C. Moore, M. S. Strano, E. J. Haroz, R. H. Hauge and R. E. Smalley. Individually suspended single-walled carbon nanotubes in various surfactants. *Nano Lett.*, 3:1379–1382, 2003.

[3] Y. Tan and D. E. Resasco. Dispersion of single-walled carbon nanotubes of narrow diameter distribution. *J. Phys. Chem. B*, 109:14454–14460, 2005.

[4] M. Zheng, A. Jagota, E. D. Semke, B. A. Diner, R. S. McLean, S. R. Lustig, R. E. Richardson and N. G. Tassi. DNA-assisted dispersion and separation of carbon nanotubes. *Nat. Mater.*, 2:338–342, 2003.

[5] T. Hertal, A. Hagen, V. Talalaev, K. Arnold, F. Hennrich, M. Kappes, S. Rosenthal, J. McBride, H. Ulbricht and E. Flahaut. Spectroscopy of single- and double-wall carbon nanotubes in different environments . *Nano Lett.*, 5:511–514, 2005.

[6] M. S. Strano, C. B. Huffman, V. C. Moore, M. J. O'Connell, E. H. Haroz, J. Hubbard, M. Miller, K. Rialon, C. Kittrell, S. Ramesh, R. H. Hauge and R. E. Smalley. Reversible, band-gap-selective protonation of single-walled carbon nanotubes in solution. *J. Phys. Chem. B*, 107(29):6979–6985, 2003.

[7] W. Zhao, C. Song and P. E. Pehrsson. Water-soluble and optically pH-sensitive single-walled carbon nanotubes from surface modification. *J. Am. Chem. Soc.*, 124:12418–12419, 2002.

[8] G. Dukovic, B. E. White, Z. Zhou, F. Wang, S. Jockusch, M. L. Steigerwald, T. F. Heinz, R. A. Friesner, N. J. Turro and L. E. Brus. Reversible surface oxidation and efficient luminescence

quenching in semiconductor single-wall carbon nanotubes. *J. Am. Chem. Soc.*, 126:15269–15276, 2004.

[9] M. J. O'Connell, S. M. Bachilo, C. B. Huffman, V. C. Moore, M. S. Strano, E. H. Haroz, K. L. Rialon, P. J. Boul, W. H. Noon, C. Kittrell, J. Ma, R. H. Hauge, R. B. Weisman and R. E. Smalley. Band gap fluorescence from individual single-walled carbon nanotubes. *Science*, 297:593–596, 2002.

[10] O. Matarredona, H. Rhoads, Z. Li, J. H. Harwell, L. Balzano and D. E. Resasco. Dispersion of single-walled carbon nanotubes in aqueous solutions of the anionic surfactant NaDDBS. *J. Phys. Chem. B*, 107(48):13357–13367, 2003.

[11] M. Zheng and B. A. Diner. Solution Redox Chemistry of Carbon Nanotubes. *J. Am. Chem. Soc.*, 126:15490–15494, 2004.

[12] K. Okazaki, Y. Nakato and K. Murakoshi. Absolute potential of the Fermi level of isolated single-walled carbon nanotubes. *Phys. Rev. B*, 68:035434, 2003.

[13] P. W. Barone, S. Baik, D. A. Heller and M. S. Strano. Absolute potential of the Fermi level of isolated single-walled carbon nanotubes. *Nat. Mater.*, 4:86-92, 2005.

[14] P. Nikolaev, M. J. Bronikowski, R. K. Bradley, F. Rohmund, D. T. Colbert, K. A. Smith and R. E. Smalley. Gas-phase catalytic growth of single-walled carbon nanotubes from carbon monoxide. *Chem. Phys. Lett.*, 313:91–97, 1999.

[15] B. Shan and K. Cho. First principles study of work functions of single wall carbon nanotubes. *Phys. Rev. Lett.*, 94:236602, 2005.

[16] M. J. O'Connell, E. E. Eibergen and S. K. Doorn. Chiral selectivity in the charge-transfer bleaching of single-walled carbon-nanotube spectra. *Nat. Mat.*, 4:412–418, 2005.

[17] M. L. Hitchman. *Measurement of Dissolved Oxygen.* Wiley, New York, 1978.

[18] Sodium decylsulfate (Acros), Sodium dodecylbenzene-sulfonate (Sigma), Sodium n-lauroylsarcosinate (Fluka) and Cetyltrimethyl-Ammonium Bromide (Fluka).

[19] L. J. Li, and R. J. Nicholas. Bandgap-selective chemical doping of semiconducting single-walled carbon nanotubes. *Nanotech.*, 15:1844–1847, 2004.

[20] T. Markvart and L. Castaer. *Practical Handbook of Photovoltaics: Fundamentals and Applications.* Elsevier, Oxford, 2003.

[21] S. S. Sun and N. S. Sariciftci. *Organic photovoltaics : mechanism, materials, and devices.* Taylor & Francis, London, 2005.

[22] C. Kittel. *Introduction to solid state physics.* Wiley, New York, 7 edition, 2005.

[23] M. Pope and C. E. Swenberg. *Electronic processes in organic crystals and polymers.* Oxford University Press, Oxford, 2 edition, 1999.

[24] N. C. Greenham, X. G. Peng and A. P. Alivisatos. Charge separation and transport in conjugated-polymer/semiconductor-nanocrystal composites studied by photoluminescence quenching and photoconductivity. *Phys. Rev. B*, 54:17628–17637, 1996.

[25] J. J. M. Halls, C. A. Walsh, N. C. Greenham, E. A. Marseglia, R. H. Friend, S. C. Moratti and A. B. Holmes. Efficient photodiodes from interpenetrating polymer networks. *Nature*, 396:498–500, 1995.

[26] W. U. Huynh, J. J. Dittmer and A. P. Alivisatos. Hybrid nanorod-polymer solar cells. *Science*, 295:2425–2427, 2002.

[27] G. Yu, J. Gao, J. C. Hummelen, F. Wudl and A. J. Heeger. Polymer photovoltaic cells: Enhanced efficiencies via a network of internal donor-acceptor heterojunctions. *Science*, 270:1789–1791, 1995.

[28] E. Kymakis and G. A. J. Amaratunga. Single-wall carbon nanotube/conjugated polymer photovoltaic devices. *Appl. Phys. Lett.*, 80:112–114, 2001.

[29] K. W. Lee, S. P. Lee, H. Choi, K. H. Mo, J. W. Jang, H. Kweon and C. E. Lee. Enhanced electroluminescence in polymer-nanotube composites. *Appl. Phys. Lett.*, 91:023110, 2007.

[30] B. J. Landi, R. P. Raffaelle, S. L. Castro and S. G. Bailey. Single-wall carbon nanotube-polymer solar cells. *Prog. Photovolt: Res. Appl.*, 13:165–172, 2005.

[31] S. Kazaoui, N. Minami, B. Nalini, Y. Kim and K. Hara. Near-infrared photoconductive and photovoltaic devices using single-wall carbon nanotubes in conductive polymer films. *J. Appl. Phys.*, 98:084314, 2005.

[32] A. Nish, J.-Y. Hwang, J. Doig and R. J. Nicholas. Highly selective dispersion of single-walled carbon nanotubes using aromatic polymers. *Nature Nanotech.*, 2:640-646, 2007.

[33] S. M. Bachilo, M. S. Strano, C. Kittrell, R. H. Hauge, R. E. Smalley and R. B. Weisman. Structure-assigned optical spectra of single-walled carbon nanotubes. *Science*, 298:2361–2366, 2002.

[34] R. B. Weisman and S. M. Bachilo. Dependence of optical transition energies on structure for single-walled carbon nanotubes in aqueous suspension: An empirical kataura plot. *Nano. Lett.*, 3:1235–1238, 2003.

[35] T. Ando. Excitons in carbon nanotubes revisited: Dependence on diameter, aharonovbohm flux, and strain. *J. Phys. Soc. Jpn.*, 73:3351–3363, 2004.

[36] O. Mirzov and I. G. Scheblykin. Photoluminescence spectra of a conjugated polymer: from films and solutions to single molecules. *Phys. Chem. Chem. Phys.*, 8:5569–5576, 2006.

[37] K. Yanagi, K. Iakoubovskii, H. Matsui, H. Matsuzaki, H. Okamoto, Y. Miyata, Y. Maniwa, S. Kazaoui, N. Minami and H. Kataura. Photosensitive function of encapsulated dye in carbon nanotubes. *J. Am. Chem. Soc.*, 129:4992–4997, 2007.

[38] J. Yang, I. Shalish and Y. Shapira. Photoinduced charge carriers at surfaces and interfaces of poly [2-methoxy-5-(2-ethyl-hexyloxy)-1,4-phenylene vinylene] with Au and GaAs. *Phys. Rev. B*, 64:035325, 2001.

[39] S. Janietz, D. D. C. Bradley, M. Grell, C. Giebeler, M. Inbasekaran and E. P. Woo. Electrochemical determination of the ionisation potential and electron affinity of poly(9,9-dioctylfluorene). *Appl. Phys. Lett.*, 73:2453–2455, 1998.

[40] C. W. Chen and M. H. Lee. Dependence of workfunction on the geometries of single-walled carbon nanotubes. *Nanotech.*, 15:480–484, 2004.

[41] J. Zhao, J. Han and J. P. Lu. Work functions of pristine and alkali-metal intercalated carbon nanotubes and bundles. *Phys. Rev. B*, 65:193401, 2002.

[42] K. E. Sapsford, L. Berti and I. L. Medintz. Materials for fluorescence resonance energy transfer analysis: Beyond traditional donor-acceptor combinations. *Angewandte Chemie- International Edition*, 45:4562–4588, 2006.

[43] Y. X. Liu, M. A. Summers, S. R. Scully and M. D. McGehee. Resonance energy transfer from organic chromophores to fullerene molecules. *J. Appl. Phys.*, 99:093521, 2006.

[44] Y. Oyama, Y. Saito, K. Sato, J. Jiang, G. G. Samsonidze, A. Gruneis, Y. Miyauchi, S. Maruyama, A. Jorio, G. Dresselhaus and M. S. Dresselhaus. Photoluminescence intensity of single-wall carbon nanotubes. *Carbon*, 44:873–879, 2006.

[45] Y. G. Ha, E. A. You, B. J. Kim and J. H. Choi. Fabrication and characterization of OLEDs using MEH-PPV and SWCNT nanocomposites. *Synth. Met.*, 153:205–208, 2005.

# Chapter 7

# Magneto-Photoluminescence Studies

## 7.1 Background

The presence of magnetic flux threading a single walled nanotube parallel to its axis causes a significant perturbation of the electronic band structure and exciton states. This phenomenon arises from a manifestation of the Aharanov-Bohm effect. It's appearance in SWNTs was first reported by Zaric et al. in 2004 [1], who performed magneto-optical studies on solutions of nanotubes at room temperature. The effects and behavior have since been detailed in numerous studies [2, 3, 4].

The observed change in optical transition energies in either magneto absorbance or magneto photoluminescence experiments arises from the addition of a phase shift to the electronic wavefunction which determines the allowed wavevectors of the nanotube. This can be visualized as a rotation of these wavevectors with respect to the underlying graphene energy surface. Such rotation causes a lifting of the degenerate energy levels which determine the nanotube's optical energy transitions. In absorbance this results in a splitting of the peak but in photoluminescence only a red-shift is seen, since the carriers will preferably emit from the lowest energy state. The application of a magnetic field shifts in the band gap by an amount

$$\frac{\Delta_{AB}}{E_g} = \pm\frac{3\pi d^2 B}{4\phi_0} \tag{7.1}$$

for a SWNT of bandgap $E_g$ and diameter $d$ lying parallel to an applied magnetic field $B$, where $\phi_0$ ($= h/e$) is the flux quantum [5, 6, 7]. The splitting is labeled as Ajiki-Ando (AA) splitting [5].

Further interesting behavior in the photoluminescence was noticed when a magnetic field was applied to SWNTs at low temperatures [3]. Here, applying a magnetic field was found to have the effect of increasing the SWNT emission; whilst at room temperature the magnetic field has little or no effect on the PL intensity. This arises from an interplay of the lowest lying excitonic levels that can best be observed as T$\rightarrow$0 and is explained as follows: As they are cooled the nanotubes' luminescence efficiency decreases. This was explained by Perebeinos [8] and others as the relaxation of carriers into a 'Dark' exciton state lying below the main emissive 'Bright' state. At higher temperatures than absolute zero thermal energy populates the upper emissive level. However, this is suppressed as the SWNTs are cooled, resulting in a decrease in the luminescence efficiency below $\sim$20 - 100K (depending on the tube type). Applying a magnetic field parallel to the nanotube axis causes a reversal of this

behavior and the luminescence intensity is found to increase once again. The AB phase lifts the degeneracy of the K and K′ states, which control the symmetry of the excitons. For sufficiently large AB flux [9] - the bonding and antibonding states are decoupled resulting in two Bright exciton peaks, corresponding to the KK and K′K′ excitons, split by $\delta E_g$. This mechanism has been shown to be the origin of magnetic brightening observed in nanotubes at low temperatures [2, 3, 10, 4], although the range of energy values deduced for the splitting of the Bright and Dark singlet states is quite large and showed a strong dependence on the chiral vector indices $(n, m)$ and nanotube diameter $(d)$.

Previous work done in the group (for which I was a contributing author, [11]) had reveled the importance of having samples which could withstand being frozen to 2K and allow alignment of the SWNTs in order to enhance this magnetic brightening effect. The dispersion of nanotubes in polymer solutions, which has been described in the previous chapters, solves both of these problems. Firstly the solutions can be dried to form films of polymer in which the nanotubes are embedded. These films have excellent luminescence efficiency, are stable down to 2K and, unlike frozen aqueous surfactant solutions, can be cooled and warmed many times without degradation. Secondly, polymer films can be stretched. The stretching has been shown to increase the alignment of nanotubes along the stretch vector [12], increasing their optical resonances when polarised light is used as well as their magneto-optical response.

Thus a magneto-photoluminescence study has been performed using the samples of SWNT prepared in MEHPPV films. It is demonstrated that where the Dark and Bright exciton states are close together in energy, magnetic brightening effects are limited and a not before seen high field effect is found in which the luminescence efficiency falls with increasing magnetic field. The intensity dependence is again attributed to the magnetic field induced mixing of the wavefunctions of the exciton states. Evidence of the strain playing a role in determining the splitting between exciton levels is shown by comparing samples prepared by different methods. Functional fitting of the data allows the estimation of the exciton splitting as well as the diameter dependence of the Aharanov-Bohm phase-induced energy shifts. The results are remarkably self consistent and similar to those found by previous studies although the origin of the high field suppression of PL is yet to be explained.

## 7.2 The Experiment

In order to provide a wide range of diameters for our study, SWNTs produced by the HiPCO (Carbon Nanotech.) growth technique were used in conjunction with the non-selective wrapping polymer, MEHPPV (American Dye Source). The preparation method for SWNTs with organic polymers has been described previously [13, 14, 15]. For this set of experiments the optimal solvent for the solution dispersions was found to be o-xylene (Sigma-Aldrich). The samples were then prepared in two different ways from the same starting solution. In the first method the MEHPPV-HiPCO was dried by repeatedly dropping a small volume of the solution onto a thin glass substrate. This produced a thick deposit which contained the nanotubes randomly orientated in the amorphous polymer matrix. In the second case a second polymer (polystyrene) was added to the initial solution and the composite dried in a similar manner as before. It was then possible to align the nanotubes along a particular direction by removing the deposit from the substrate and stretching it along one direction [16]. These films were thicker and more robust and could be stretched by up to a factor of 5 at $\sim$370°K. The increased alignment of the SWNTs in the polymer matrix was verified using polarized PL spectroscopy.

Photoluminescence-excitation maps were taken for each of the samples at 2K showing the distinctive peaks corresponding to nanotube $E_{11}$-$E_{22}$ resonances. Excitation was made in the range 710-850nm using a tunable Ti:sapphire laser and in the range 610-660nm using a tunable dye laser. Typical estimated output powers illuminating the sample were in the region of 1mW. Collection was made through an optical fibre bundle with a liquid nitrogen cooled InGaAs array detector and 0.3m spectrometer. A schematic of the sample mount is shown in figure 7.1. Measurements of the field dependence were made in the Voigt geometry using polarizers mounted adjacent to the samples both parallel and perpendicular to the field for light propagating perpendicular to the field direction. Both exciting and emitted radiation are polarized giving an added selectivity to the orientation of the SWNTs which are probed. Optical absorption and emission in carbon nanotubes is strongly dependent upon the polarization of the incident light, with preferential absorption observed at the primary band gaps for light polarized parallel to the tube axis [17, 18]. Continuous fields of up to 32T were provided by a 24MW resistive-coil magnet at the Grenoble High Magnetic Field Lab. A variable temperature insert inside the magnet bore allowed control of the temperature from 2K to 280K.

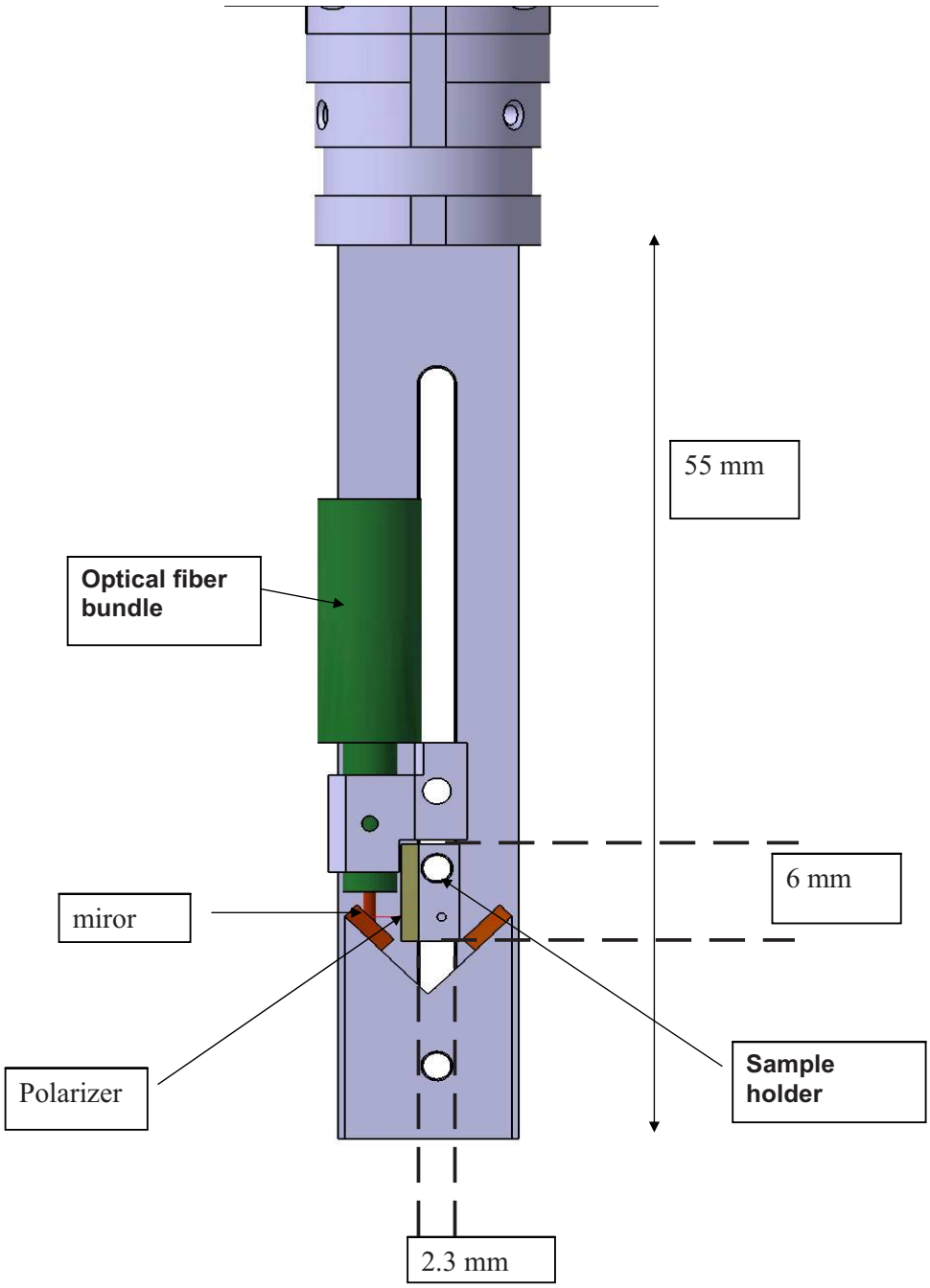


Figure 7.1: The insert used to measure photoluminescence from the SWNT films inside the bore of the 32T magnet at the Grenoble High Magnetic Field Laboratory.

## 7.3 Results

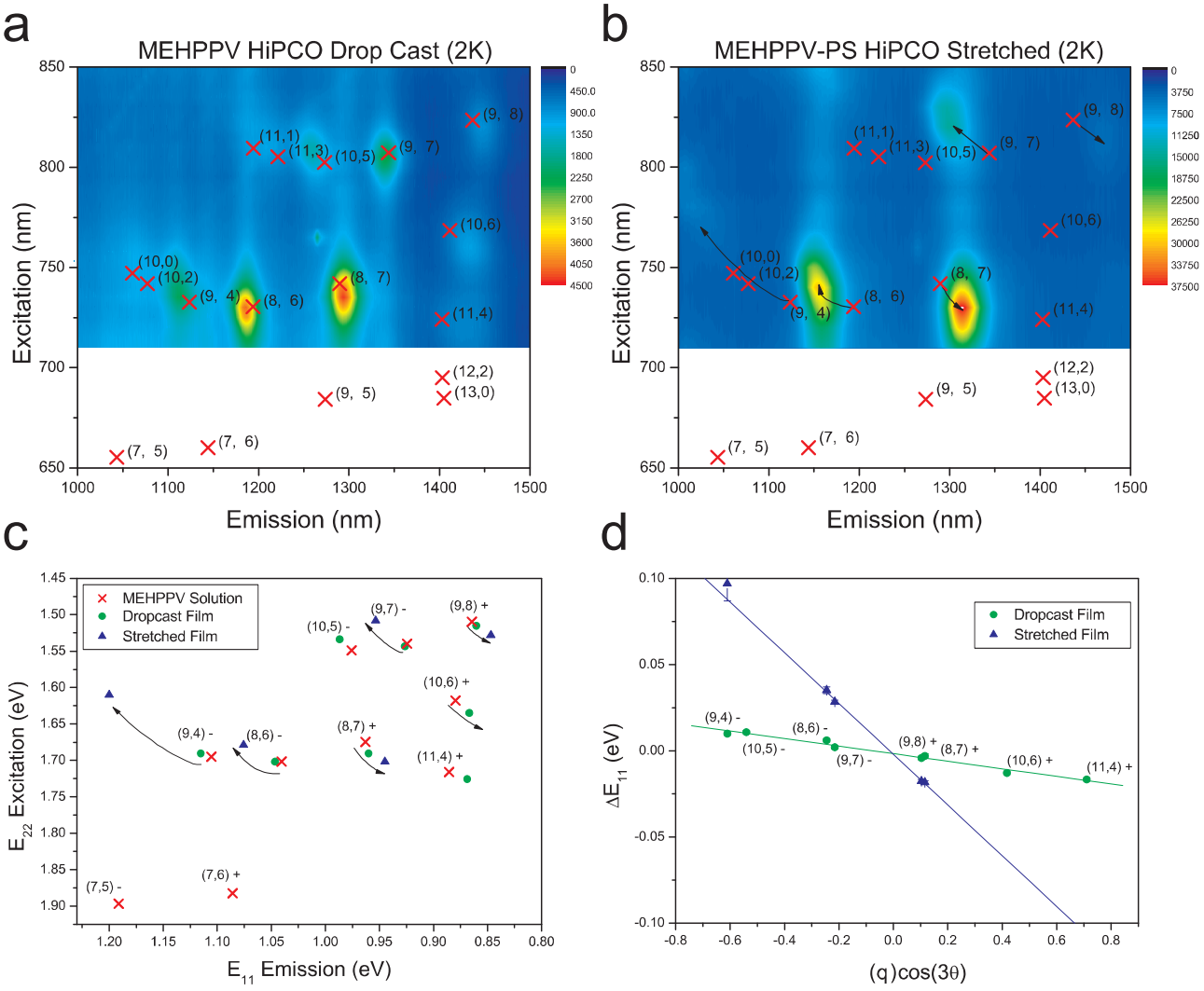


Figure 7.2: Parts **a** & **b** show PLE maps from Ti:sapphire excited tube species for both film samples at 2°K. The red crosses represent the positions of the $(n, m)$ indexed SWNT peaks in MEHPPV-solvent solution. Arrows indicate the shifts in the transitions due to strain. These shifts are shown on an energy scale in part **c**. Part **d** shows the dependence of the $E_{11}$ transition on the nanotube chiral angle $\theta$.

Photoluminescence-excitation maps are show in figure 7.2, as measured for the two different preparations of polymer wrapped nanotubes at 2K in the region 710 - 850nm; which covers the majority of the nanotubes species present. The smaller diameter $(7, 5)$ & $(7, 6)$ species were probed using resonant excitation at around 660nm from the dye-laser. Shifts are observed in the positions of the transitions which are consistent with the family behavior that arises from the presence of a large uniaxial strain component [19]. This is most evident in the stretched polystyrene-MEHPPV/CNT film.

The shifts may be analysed using the expression for the strain induced band gap shift $\Delta E_g^s$ following the theory of Yang and Han [20] and as shown by Li et al. [21] and Leeuw et al. [22]

$$\Delta E_g^s = 3q\gamma_0[(1+\nu)\sigma cos(3\theta)] \tag{7.2}$$

where $q$=±1 (from $n$-$m$=3$p$+$q$), $\gamma_0$ is the carbon-carbon transfer integral, $\nu$ is Poisson's ratio, $\sigma$ is the strain along the nanotube axis and $\theta$ is the chiral angle. Using this expression the shifts shown in figure 7.2 allow us to deduce relative levels of strain of 0.16% and 0.02% for the stretched polystyrene-MEHPPV film and drop cast MEHPPV film samples respectively at 2K. This should be compared with values of order 0.25% as found in the quench frozen samples [21, 23] used for our previous magneto-PL studies [4].

Figure 7.3 shows a set of magneto-PL spectra for the $(8,7)$ species for the drop cast film where the polarized light selects tubes closest to parallel with the magnetic field. This shows a characteristic behavior in which there is a rapid initial magnetic brightening, followed by a significant fall in intensity at high fields. The emission peak position shows an almost linear decrease in energy at high field with field coefficient $\alpha = \frac{dE_g}{dB}$ meV/T. The experiments were repeated for light polarized perpendicular to the magnetic field direction. For this case a similar magnetic brightening and shift of the emission energies was observed but with a considerably reduced field coefficient and a brightening which occurred at much larger magnetic fields as illustrated in figure 7.4. This behavior is consistent with a much smaller AB flux threading the nanotubes which have been selected by this polarization, due to their dominant orientation perpendicular to the magnetic field. When the experiments were performed with the polystyrene strained films similar field coefficients were observed, but the magnetic brightening effects were much larger and higher fields were required to observe the high field fall in intensity, consistent with our previous measurements on strained aqueous solutions [4] where only saturation was observed in larger diameter tubes studied up to 19.5T.

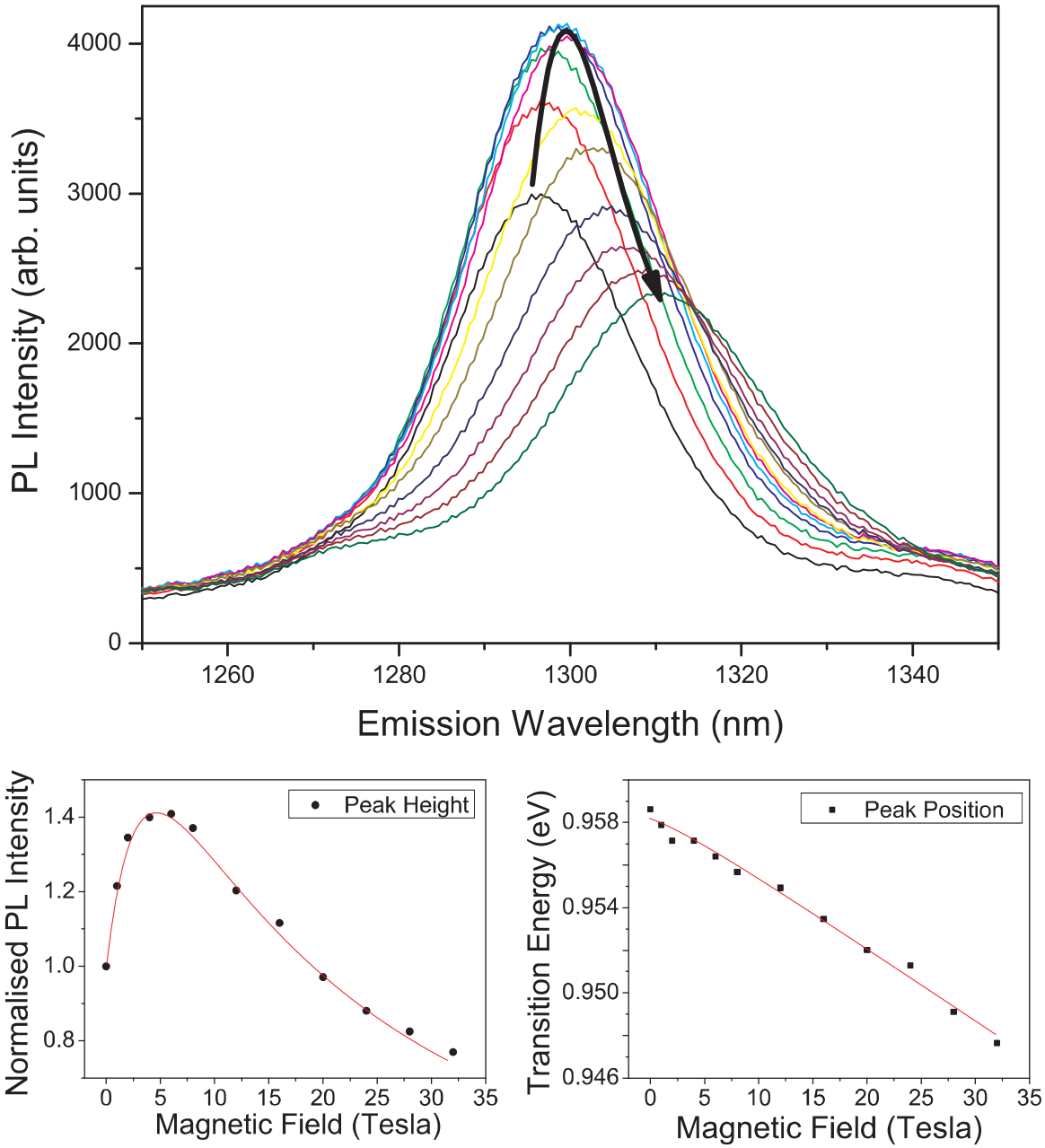


Figure 7.3: The PL peak of the (8,7) species as measured between 0 and 32T. The lower figures show the separate behaviors of the amplitude and emission energy.

We fit the magnetic brightening behavior using a conventional two level Hamiltonian analysis [10]

$$\hat{H} = \frac{\Delta_x}{2}\hat{\sigma_z} + \Delta_{AB}\hat{\sigma_x} \tag{7.3}$$

where $\Delta_x$ is the Dark-Bright exciton splitting, $\Delta_{AB}$ is the Aharanov-Bohm shift and $\hat{\sigma_x}$ and $\hat{\sigma_z}$ are the Pauli spin matrices. In order to fit the observed behavior, however, it is necessary to introduce two additional factors. Firstly, there is a finite intensity as T $\rightarrow$ 0, which we model by assuming that there is a finite AB shift at $B = 0$ of $\Delta_0$. This has been included in previous studies [3, 10, 4] where it has been attributed to disorder effects.

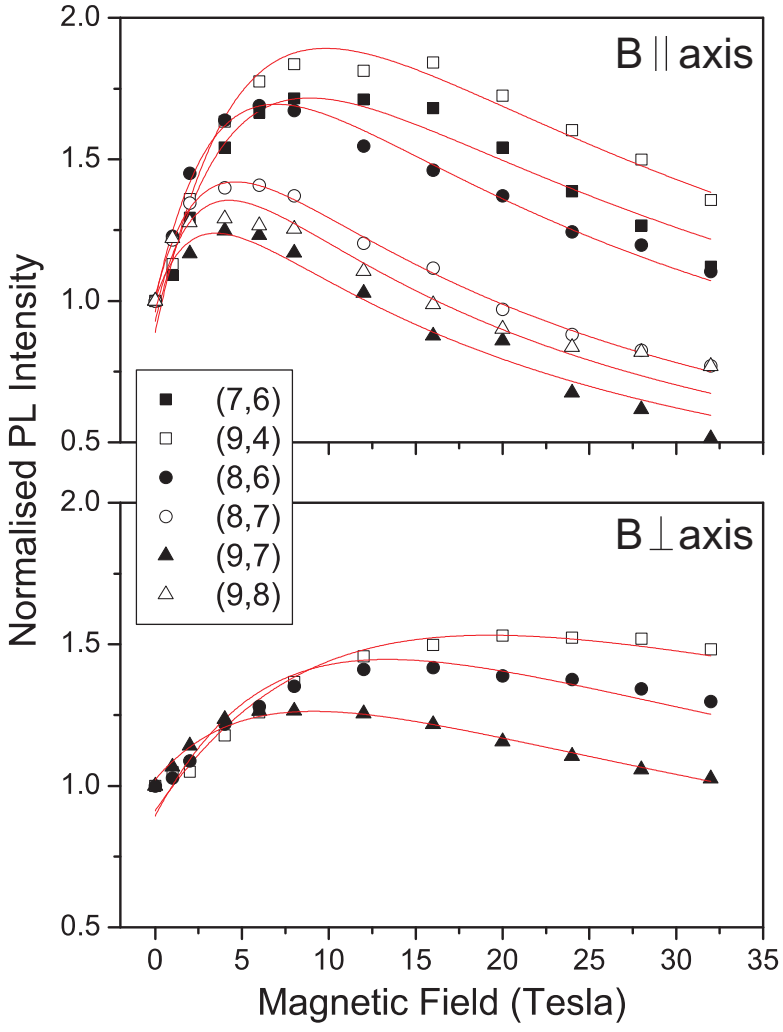


Figure 7.4: PL intensity for a range of nanotube species as a function of field. The use of polarised light allows the study of SWNTs oriented either parallel or perpendicular to the magnetic field.

The total AB splitting is therefore given by

$$\Delta_{AB} = \alpha B + \Delta_0. \tag{7.4}$$

Secondly there is clearly a systematic decrease in intensity with magnetic field. We model this by introducing an additional factor in the intensity $\sim 1/\Delta_{AB}$ whose origin is yet to be explained. This gives a total intensity dependence on magnetic field of

$$I = \frac{\Delta_{AB}^2}{\Delta_{AB}^2 + [\frac{\Delta_x}{2} + \sqrt{\frac{\Delta_x^2}{4} + \Delta_{AB}^2}]^2} \times \frac{A}{\Delta_{AB}} \tag{7.5}$$

where the amplitude $A$ is a fitting constant. The emission energy dependence is given by

$$E = E_0 - \frac{\Delta_x + \sqrt{\Delta_x^2 + 4\Delta_{AB}^2}}{2} \tag{7.6}$$

where $E_0$ is the unperturbed transition energy. The measured magnetic field dependent intensities have been fitted to equation 7.5, which is found to give a good description of the observed data, and the energy dependence is fitted to equation 7.6. The values of $\alpha$ are mainly determined by the high field dependence of $E$, while the values for $\Delta_x$ come mainly from the intensity dependence.

The values deduced for the Dark-Bright exciton splitting are shown in figure 7.5 and display two clear trends. Firstly the values deduced for the dropcast film, which has much less strain, are significantly lower (by a factor of ∼0.7) than those deduced for the stretched polystyrene film. Secondly there is a clear diameter dependence in which the splitting increases rapidly as the diameter decreases. The values for the strained films are comparable to those reported recently by Shaver et al [10] as deduced also from magnetic brightening for a few species in stretch aligned films. The values for the unstrained films are however much more similar to the values deduced from the temperature dependence of the emission from frozen solutions [3], and to values deduced from measurements on individual nanotubes which have been recently reported [24]. The strain will influence the exciton binding energies through changes in the role of trigonal warping in the band structure which is known to influence the excitons [25]. The individual nanotube measurements show a very wide spread of values [24] even for the same species of tube, but tend towards a large diameter tube result of ∼2.5meV as observed here. This suggests that although environmental factors such as local dielectric constant or strain play a significant

role in determining the exciton splitting as would be expected for Coulomb effects [26, 27, 8, 9, 28], the large diameter limit may correspond to essentially degenerate Bright and Dark excitons.

It is now clear that the observed high field behavior of magnetic suppression of PL intensity is only observable in the very high field limit $\Delta_{AB} \gg \Delta_x$, which is accessed in the present study due to the small values of $\Delta_x$ that occur for unstrained samples. The origin of this behavior is yet to be determined.

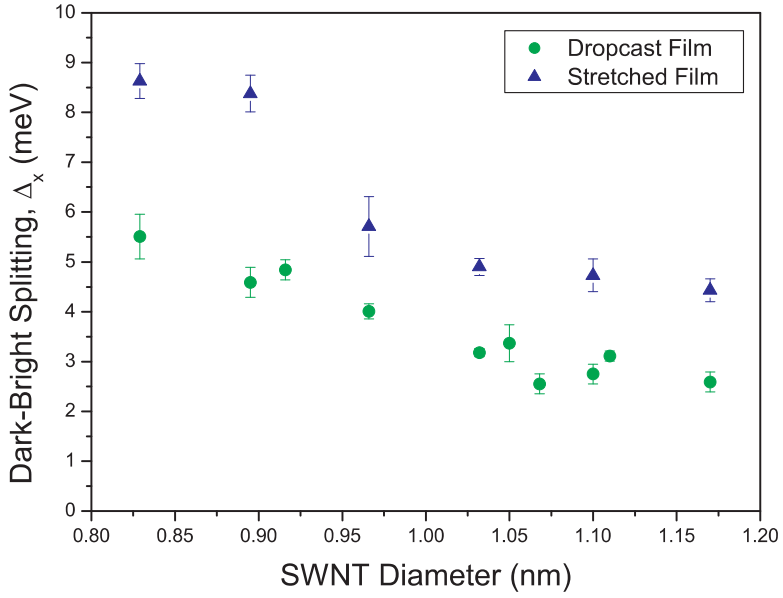


Figure 7.5: Dark-Bright exciton splittings as deduced for light polarized parallel to the SWNT axis from fitting to equation 7.5.

The values for $\alpha$ are shown in figure 7.6 as a function of $d$, compared with the values expected theoretically. The largest AB flux shift is measured when the tubes are aligned using the stretching and polarization parallel to the magnetic field. The values have been obtained by independent fitting of both the energy shift and the intensity dependence.

One further parameter which emerges from the analysis is the zero field AB splitting $\Delta_0$. This has been set to an arbitrary value of 1meV in the fitting for both the strained and unstrained films. Previous interpretations that the phenomenon is due to disorder may be incorrect. Instead we suggest that it is more likely that it is due to the presence of a small spin-orbit splitting in the nanotubes, as suggested by Ando [29]. Further study of this parameter is required to determine its value, tube dependence and field behavior.

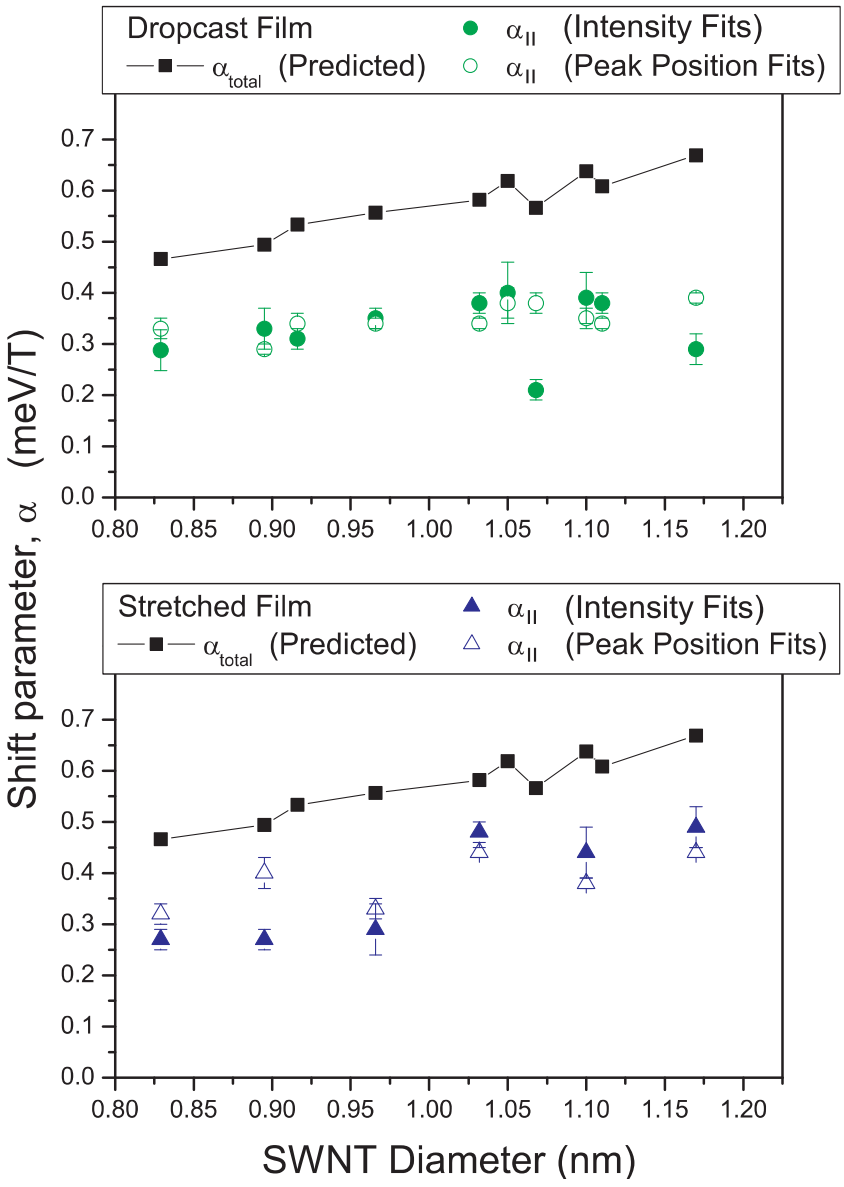


Figure 7.6: The values determined for the AB shift parameter, $\alpha$, show an excellent agreement when deduced independently from the intensity dependence and peak position data.

## 7.4 Discussion

The use of SWNTs prepared in MEHPPV is far superior to the surfactant solutions which had previously been used due to their strong photoluminescence and absence of strain. We have shown that the Dark-Bright exciton splittings in single walled carbon nanotubes are strongly dependent on the strain state and local environment of the nanotubes. Large diameter, unstrained nanotubes have very small splittings, of order 2.5meV, which allow us to access a previously unknown high field limit in which the PL intensity is found to be suppressed by high magnetic fields. This behavior has not been previously expected. The experiments done here have opened up new questions about the photo-physics of the nanotubes and revealed features which could be researched in future.

# Bibliography


[1] S. Zaric, G. N. Ostojic, J. Kono, J. Shaver, V. C. Moore, M. S. Strano, R. H. Hauge, R. E. Smalley and X. Wei. Optical signatures of the aharanov-bohm phase in single-walled carbon nanotubes. *Science*, 304:1129, 2004.

[2] S. Zaric, G. N. Ostojic, J. Shaver, J. Kono, O. Portugall, P. H. Frings, G. L. J. A. Rikken, M. Furis, A. Crooker, X. Wei, V. C. Moore, R. H. Hauge and R. E. Smalley. Excitons in carbon nanotubes with broken time-reversal symmetry. *Phys. Rev. Lett.*, 96:016406, 2006.

[3] I. B. Mortimer and R. J. Nicholas. The role of bright and dark excitons in the temperature dependent photoluminescence of carbon nanotubes. *Phys. Rev. Lett.*, 98:027404, 2007.

[4] I. B. Mortimer, L.-J. Li, R. A. Taylor, G. L. J. A. Rikken, O. Portugall and R. J. Nicholas. Magneto-optical studies of single walled carbon nanotubes. *Phys. Rev. B*, 76:085404, 2007.

[5] H. Ajiki and T. Ando. Electronic states of carbon nanotubes. *J. Phys. Soc. Japan*, 62:1255, 1993.

[6] S. Roche, G. Dresselhaus, M. S. Dresselhaus and R. Saito. Aharonov-bohm spectral features and coherence length in carbon nanotubes. *Phys. Rev. B*, 62:16092, 2000.

[7] F. L. Shyu, C. P. Chang, R. B. Chen, C. W. Chiu and M. F. Lin. Magnetoelectronic and optical properties of carbon nanotubes. *Phys. Rev. B*, 67:045405, 2003.

[8] V. Perebeinos, J. Tersoff and P. Avouris. Radiative lifetime of excitons in carbon nanotubes. *Nano. Lett.*, 5:2495, 2005.

[9] T. Ando. Effects of valley mixing and exchange on excitons in carbon nanotubes with aharanov-bohm flux. *J. Phys. Soc. Japan*, 75:024707, 2006.

[10] J. Shaver, J. Kono, O. Portugall, V. Krystic, G. L. J. A. Rikken, Y. Miyauchi, S. Maruyama and V. Perebeinos. Optical signatures of the aharanov-bohm phase in single-walled carbon nanotubes. *Nano Letters*, 7:1851, 2007.

[11] R. J. Nicholas, I. B. Mortimer, L.-J. Li, A. Nish, O. Portugall and G. L. J. A. Rikken. Temperature and magnetic field dependent photoluminescence from carbon nanotubes. *Intl. J. Modern Phys.*, 21:1180-1188, 2007.

[12] Y. Kim, N. Minami and S. Kazaoui. Highly polarized absorption and photoluminescence of stretch-aligned single-wall carbon nanotubes dispersed in gelatin films. *Appl. Phys. Lett.*, 86:073103, 2005.

[13] A. Nish, J. Y. Hwang, J. Doig and R. J. Nicholas. Highly selective dispersion of single-walled carbon nanotubes using aromatic polymers. *Nature Nanotechnology*, 2:640, 2007.

[14] A. Nish, J. Y. Hwang, J. Doig and R. J. Nicholas. Direct spectroscopic evidence of energy transfer from photo-excited semiconducting polymers to single-walled carbon nanotubes. *Nanotechnology*, 19:095603, 2008.

[15] J. Y. Hwang, A. Nish, J. Doig, S. Douven, C. W. Chen, L. C. Chen and R. J. Nicholas. Polymer structure and solvent effect on the selective dispersion of single-wall carbon nanotube. *J. Am. Chem. Soc.*, 130:3543, 2008.

[16] J. Shaver, S. A. Crooker, J. A. Fagan, E. K. Hobbie, N. Ubrig, O. Portugall, V Perebeinos, Ph Avouris and J Kono. Magneto-spectroscopy of highly-aligned carbon nanotubes: Identifying the role of threading magnetic flux. *arXiv*, page 0802.3203v1, 2008.

[17] H. Ajiki. Magnetic-field effects on the optical spectra of a carbon nanotube. *Phys. Rev. B*, 65:233409, 2002.

[18] J. Lefebvre, J. M. Fraser, P. Finnie and Y. Homma. Photoluminescence from an individual single-walled carbon nanotube. *Phys. Rev. B*, 69:075403, 2004.

[19] R. S. Deacon, K. C. Chuang, J. Doig, I. B. Mortimer and R. J. Nicholas. Photoluminescence study of aqueous-surfactant-wrapped single-walled carbon nanotubes under hydrostatic pressure. *Phys. Rev. B*, 74:201402, 2006.

[20] L. Yang and J. Han. Strain effects on nanotubes. *Phys. Rev. Lett.*, 85:154, 2000.

[21] L.-J. Li, R. J. Nicholas, R. S. Deacon and P. A. Shields. Chirality assignment of single-walled carbon nanotubes with strain. *Phys. Rev. Lett.*, 93:156104, 2004.

[22] P. N. Nikolaev S. M. Bachilo S. Arepalli T. Leeuw, D. A. Tsyboulski and R. B. Weisman. *Nano. Lett.*, 8:826–831, 2008.

[23] K. Arnold, S. Lebedkin, O. Kiowski, F. Hennrich and M. M. Kappes. Matrix-imposed stress-induced shifts in the photoluminescence of single-walled carbon nanotubes at low temperatures. *Nano Letters*, 4:2349, 2004.

[24] A. Srivastava, H. Htoon, V.I. Klimov and J. Kono. Direct observation of dark excitons in individual carbon nanotubes. *arXiv*, page 0804.0875, 2008.

[25] J. Jiang, R. Saito, G. G. Samsonidze, A. Jorio, S. G. Chou, G. Dresselhaus and M. S. Dresselhaus. Chirality dependence of exciton effects in single-wall carbon nanotubes: Tight-binding model. *Phys. Rev. B*, 75:035407, 2007.

[26] H. Zhao, S. Mazumdar, C.-X. Sheng, M. Tong and Z. V. Vardeny. Photophysics of excitons in quasi-one-dimensional organic semiconductors: Single-walled carbon nanotubes and $\pi$-conjugated polymers. *Phys. Rev. B*, 73:075403, 2006.

[27] C. D. Spataru, S. Ismail-Beigi, R. B. Capaz and S. G. Louie. Theory and ab initio calculation of radiative lifetime of excitons in semiconducting carbon nanotubes. *Phys. Rev. Lett.*, 95:247402, 2005.

[28] K.-C. Chuang, A. Nish, J.-Y. Hwang, G. Evans and R. J. Nicholas. An experimental study of coulomb corrections and single particle energies for single-walled carbon nanotubes using cross-polarized photoluminescence. *Phys. Rev. B*, 80:in press, 2008.

[29] T. Ando. Spin-orbit in carbon nanotubes. *J. Phys. Soc. Jpn.*, 69:1757, 2000.

# Chapter 8

# Conclusions

A number of significant contributions to the field of carbon nanotube research have been made during the course of work for this thesis through the use of optical spectroscopy and advanced sample preparation. The main achievements have been:

1. An explanation of temperature mediated redox reactions on SWNTs which occur in aqueous surfactant solutions.
2. The advancement of sample characterisation through the development of an automated PLE mapping system & the subsequent demonstration of its utility for bulk characterisation of batches of SWNT material.
3. Investigation of polymer-organic solvent combinations as dispersing agents.
4. Discovery of the ability of some polyfluorenes to selectively wrap and suspend small diameter, high chiral angle nanotubes.
5. A study of energy transfer from photoexcited conjugated polymers to SWNTs using PLE mapping.
6. The use of polymer wrapped SWNTs to produce samples with low strain for magneto-PL studies.
7. Analysis of a novel high field suppression of SWNT PL and estimation of Dark-Bright exciton splittings across a range of tube diameters.

In the pursuit of each of these achievements new questions have emerged about the nature of SWNTs, the mechanisms with which they interact with their surroundings and the possibility of using them for useful applications. Four major remain issues stand out: Firstly, the photoluminescence yield in carbon nanotubes is still an open question. Does the chiral angle and diameter influence the PL yield? Or impurities and adsorbed molecules. What is the origin of the $\pi$-plasmon and how much do the metallic species contribute to it? Secondly, what are the redox potentials of SWNTs in aqueous solution and do the nanotubes' Fermi level vary with nanotube diameter? This has implications for the polymer-SWNT system as well, where a better understanding of the mechanism of photo-sensitized energy transfer is necessary. Also, what implications does the observation of emission from SWNTs have for using nanotubes as active materials in polymer solar cells. Thirdly, how do polyfluorene molecules selectively wrap the SWNTs? Is the chiral angle selectivity tunable by altering the sidechains or

sample preparation parameters? Finally, what is the origin of the high magnetic field suppression of the PL from the SWNTs which is seen at low temperatures in samples with little or no strain.

The future of carbon nanotube research is as promising as it was at the start of this project four years ago. Fundamental features have been studied thoroughly and revealed more and more detail to be explained and probed. The alluring prospect of high-tech applications is likely to drive forward investment in this area for years to come, with focus on sample preparation, efficient characterisation and quality control being of prime importance. It is hoped that aspects of the work done here will make some contribution to the advancement of technology which has yet to be realised.

*A N, 3rd July 2008*